3-D modelling of spatiotemporal variability of ice cover, water exchange and phytoplankton distribution in Lower Lake Constance

Dissertation submitted for the degree of

Doctor of Natural Sciences (Dr. rer. nat)

Presented by Irene

Caramatti

at the

Universität Konstanz

Faculty of Sciences

Department of Biology

Konstanz, 2021

Date of the oral examination: 21 December, 2021

Reviewer 1: Dr. Hilmar Hofmann

Reviewer 2: Prof. Dr. Frank Peeters

Reviewer 3: Prof. Dr. David Schleheck

Table of contents

Summary

Lake ecology is the result of complex interactions between lake hydrodynamic, lake hydrology, stream intrusion, nutrient loads, meteorology, sediment processes and lake morphology. The substantial heterogeneity of these factors within individual lakes favors the establishment of spatial gradient also within the phytoplankton community. Ability to describe the spatiotemporal hydrodynamic and water quality variability and identifying its drivers can benefit the understanding of lake ecosystems and their response to environmental stressors.

In this thesis, the three-dimensional hydrodynamic and ecological model AEM3D (3D-Aquatic Ecosystem Model) was setup to provide more insights into the spatial and temporal variability of hydrodynamic and ecological conditions in the morphologically complex lake Lower Lake Constance (LLC). The results of multi-annual continuous simulations of ice cover formation, inter-basin exchange and phytoplankton community were compared between years and between lake sub-basins. The research was conducted in a series of three separated studies.

First, the model AEM3D coupled with an ice model was calibrated and validated to simulate multi-annual hydrodynamic conditions and ice cover formation in LLC. The model results demonstrated that AEM3D is sensitive to the annual variability of the climate in reproducing the inter-annual variability of ice cover and suitable for simulating thin ice (<10 cm) and differentiating in ice cover formation between adjacent basins in a lake with complex morphometry. This study was a unique example in the field of 3D ice modelling of use of multi-sources data to validate an ice modelling study as alternative approach to a remote sensing one.

The model was then employed to investigate the inter-annual and seasonal pattern of inter-basin exchange to identify when the sub-basins are more disconnected and thus laterally more homogenous conditions are favored. The study focused on the water exchange between the sub-basins Zeller See and Gnadensee, separated by a shallow sill, and between this latter and the river Seerhein. Additionally, we assessed to which extent climate warming and associated water level changes affect inter-basin exchange and the spread of the river Seerhein into Gnadensee at seasonal time scales.

Results demonstrated the existence of a seasonal pattern of lateral exchange of water, and thus of dissolved substances and organisms, between the basin of Gnadensee and Zeller See, that

may lead to more homogenous nutrient conditions in summer than in winter. The seasonal course of water exchange is predominantly determined by the seasonal change in the current speed across the sill, but also by changes in the area of the cross-section above the sill resulting from water level changes, by the seasonal change in stratification and by ice cover formation. In summer, Gnadensee is also more under the influence of the water from the river Seerhein and hence the conditions of the upstream Upper Lake Constance.

The impact of climate warming and hydrological change on water exchange varies seasonally. Climate warming results in reduced ice cover and an earlier onset and longer duration of stratification, leading to enhanced inter-basin exchange especially during winter and spring, but not in summer. That, together with the changing in light availability resulting from shorter ice cover duration or absence of ice cover, could have a strong impact on the phytoplankton bloom that usually occurs early in the year. Additionally, the future reduced inter-seasonal pattern of water level in LLC may implying larger horizontal differences of dissolved substances and organisms between its sub-basin during summer months. Finally, the fraction of water from Upper Lake Constance reaching the rather secluded basin Gnadensee increases with climate warming, implying a larger influence of the upstream conditions on Gnadensee.

Lastly, the model was coupled with the biological module of AEM3D to simulate the spatial and temporal variability of the phytoplankton community and nutrient dynamics between the lake sub-basins over 2 years with very different ice cover formation and water level dynamics.

Results indicated that the model was able to capture the main spatial and temporal biogeochemistry variations, among which the progressive summer oxygen depletion at lake's bottom, as well as the typical seasonal algae dominant succession in LLC, even when including time periods with ice cover. Lastly, the model succeeded in simulating the presence of a deep chlorophyll maximum (DCM) caused by Cyanobacteria in Gnadensee. In agreement with data, the simulated DCM occurred only in Gnadensee but not in the other basins of LLC.

In conclusion, this study is the first investigation that provides a characterization of the spatiotemporal variability of hydrodynamic and ecology in Lower Lake Constance, advancing the understanding of the interaction of hydrodynamic and ecological processes in a morphologically complex lake, also under consideration of a changing climate.

Zusammenfassung

Die Seenökologie ist das Ergebnis komplexer Wechselwirkungen zwischen Seehydrodynamik, Seehydrologie, Strömungsintrusion, Nährstoffträger, Meteorologie, Sedimentprozessen und Seemorphologie. Die beträchtliche Heterogenität dieser Faktoren innerhalb einzelner Seen begünstigt die Ausbreitung räumlicher Gradienten auch innerhalb der Phytoplanktongemeinschaft. Die Fähigkeit, die raumzeitliche Hydrodynamik und die Variabilität der Wasserqualität zu beschreiben und ihre Treiber zu identifizieren, kann zum Verständnis der Seeökosysteme und ihrer Reaktion auf Umweltstressoren beitragen.

In dieser Thesis wurde das dreidimensionale hydrodynamische und ökologische Modell AEM3D (3D-Aquatic Ecosystem Model) herangezogen, um mehr Einblicke in die räumliche und zeitliche Variabilität hydrodynamischer und ökologischer Bedingungen im morphologisch komplexen Untersees (LLC, Lower Lake Constance) zu geben. Die Ergebnisse über mehrere Jahre laufende Simulationen der Eisdeckenbildung, des Austauschs zwischen den Becken und der Phytoplanktongemeinschaft wurden zwischen den Teilbecken des Sees über mehrere Jahre verglichen. Die Forschungsreihe besteht insgesamt aus drei getrennten Studien.

Zunächst wurde das mit einem Eismodell gekoppelte Modell AEM3D kalibriert und validiert, um mehrjährige hydrodynamische Bedingungen und Eisdeckenbildung im LLC zu simulieren. Die Modellergebnisse zeigten, dass AEM3D bei der Reproduktion der jahreszeitlichen Variabilität der Eisdecken empfindlich auf die jährliche Variabilität des Klimas reagiert und geeignet ist, dünnes Eis (<10 cm) zu simulieren und um Eisdeckenbildung zwischen benachbarten Becken in einem See mit komplexer Morphometrie zu differenzieren. Diese Studie war ein bisher einzigartiges Beispiel im Bereich der 3D-Eismodellierung für die Verwendung von Daten aus mehreren Quellen, um eine Eismodellierungsstudie als alternativen Ansatz zu einer Fernerkundungsstudie zu validieren.

Das Modell wurde dazu verwendet, um das zwischenjährliche und saisonale Muster des Austauschs der Zwischenbecken zu untersuchen, um festzustellen, wann die Unterbecken stärker voneinander getrennt sind und somit seitlich homogenere Bedingungen begünstigt werden. Im Fokus der Studie stand der Wasseraustausch der Unterbecken Zeller See und Gnadensee, getrennt durch eine flache Schwelle und zusätzlich dem Seerhein. Darüber hinaus haben wir untersucht, inwieweit die Klimaerwärmung und die damit verbundenen Wasserstandsänderungen den

Austausch der Zwischenbecken und die Ausbreitung des Seerheins in den Gnadensee auf saisonalen Zeitskalen beeinflussen.

Die Ergebnisse zeigten, dass zwischen dem Gnadensee und Zeller See ein saisonales Muster des seitlichen Austauschs von Wasser, und damit von gelösten Substanzen und Organismen, existiert, das im Sommer zu homogeneren Nährstoffverhältnissen als im Winter führen kann. Der jahreszeitliche Verlauf des Wasseraustausches wird vor allem durch die jahreszeitliche Änderung der Strömungsgeschwindigkeit über der Schwelle bestimmt, aber auch durch Änderungen im Bereich des Querschnitts oberhalb der Schwelle durch Wasserstandsänderungen, durch die jahreszeitliche Änderung der Schichtung und durch Bildung einer Eisdecke. Im Sommer steht der Gnadensee zudem stärker unter dem Einfluss des Wassers des Seerheins und damit den Bedingungen des vorgelagerten Obersees (ULC, Upper Lake Constance).

Die Auswirkungen der Klimaerwärmung und des hydrologischen Wandels auf den Wasseraustausch variieren saisonal. Die Klimaerwärmung führt zu einer geringeren Eisdecke und einem früheren Einsetzen und einer längeren Dauer der Schichtenbildung, was insbesondere im Winter und Frühjahr zu einem verstärkten Austausch zwischen den Becken führt, jedoch nicht im Sommer. Dies könnte zusammen mit der veränderten Tageslichtverfügbarkeit aufgrund einer kürzeren Dauer der Eisdecke oder des Fehlens einer Eisdecke einen starken Einfluss auf die Phytoplanktonblüte haben, die normalerweise zu Beginn des Jahres auftritt. Darüber hinaus kann das künftig reduzierte Muster des Wasserstands zwischen den Jahreszeiten im Untersee (LLC) größere horizontale Unterschiede von gelösten Substanzen und Organismen zwischen seinem Teilbecken während der Sommermonate implizieren. Schließlich steigt mit der Klimaerwärmung der Wasseranteil aus dem Obersee, der das eher abgeschiedene Becken Gnadensee erreicht, was einen größeren Einfluss der flussaufwärts gelegenen Bedingungen auf den Gnadensee impliziert.

Schließlich wurde das Modell mit dem biologischen Modul von AEM3D gekoppelt, um die räumliche und zeitliche Variabilität der Phytoplanktongmeinschaft und die Nährstoffdynamik zwischen den Teilbecken des Sees über 2 Jahre mit sehr unterschiedlicher Eisdeckenbildung und Wasserstandsdynamik zu simulieren.

Die Ergebnisse zeigten, dass das Modell in der Lage war, die wichtigsten räumlichen und zeitlichen biogeochemischen Variationen zu erfassen, darunter den fortschreitenden sommerlichen Sauerstoffmangel am Grund des Sees sowie die typische saisonale algendominante Abfolge im Untersee (LLC), selbst wenn Zeiträume mit Eisdecke einbezogen wurden. Letztendlich gelang es

durch das Modell, das Vorhandensein eines tiefen Chlorophyllmaximums (DCM) durch Cyanobakterien in Gnadensee zu simulieren. In Übereinstimmung mit den Daten erfolgte die simulierte DCM nur im Gnadensee, nicht jedoch in den anderen Becken des Untersees (LLC).

Zusammenfassend ist diese Studie die erste Untersuchung, die eine Charakterisierung der raumzeitlichen Variabilität von Hydrodynamik und Ökologie im Untersee (LLC) liefert und das Verständnis des Zusammenspiels von hydrodynamischen und ökologischen Prozessen in einem morphologisch komplexen See auch unter Berücksichtigung eines sich ändernden Klimas fördert.

1

General introduction

Freshwater lakes are important ecosystems worldwide and essential for humankind. People rely indeed on them for recreation, water supply, and fish production, whereas they are for wildlife habitats to live, feed, and reproduce. Unfortunately, during the last centuries lake ecosystems have been under severe pressure by a multitude of anthropogenic and environmental stressors, such as anthropogenic increases of nutrients (Smith & Schindler, 2009), rising temperatures and changes in water level dynamics due to climate change (Paerl & Huisman, 2008; Williamson et al., 2009), and the invasion by neobiota (Higgins & Zanden, 2010; Mack et al., 2000). That has raised the need to deeply understand ecosystem baseline conditions and their response to changes or restoration measures.

Lakes conditions are the result of the complex interaction between the lake hydrodynamic (e.g. flow velocity, thermal structure), chemical characteristics (e.g. dissolved oxygen and nutrients), and biological community. Indeed, lake hydrodynamic plays an important role for nutrient flows and related ecological processes (Alavian et al., 1992; De Cesare et al., 2006; Romero et al., 2004), and thermal stratification alters velocity profiles and hinders oxygenation in the hypolimnion (Elçi, 2008). On the other hand, for example, the transport of sediments may influence flow density and velocity (Liu, 2018).

As result of these complex interactions substantial heterogeneity exists between littoral and pelagic zones, between surface and deep water, and between sub-basins in lakes with complex morphometry. Therefore, within individual lakes, a complex set of phenomena, e.g. stratification, stream intrusions, partial ice cover and lake morphometry, leads to both horizontal and vertical heterogeneous conditions. The spatial variation in physical properties affects nutrient distribution,

primary production and trophic interactions and thus leads to spatial and temporal patterns in plankton community (Neill, 1994). Moreover, lakes are constantly exposed to changes in time as result of both natural and human forces. Changes are over both long and short periods of time, from centuries (e.g. climate change), to decades (e.g. eutrophication and re-oligotrophication), to few days (e.g. storm events) or even hours (e.g. irradiance fluctuations).

To fully grasp the complexity of the spatiotemporal variation in lakes and their dynamic response to changes, a mechanistic approach is required. Lake numerical models are essential tools that help to seize the lake complexity, to extend our understanding of physical, chemical and, biological processes of the ecological systems (Gal et al., 2009). Moreover, they enhance the interpretation of available data, compensate for the lack of frequent and extended field measurements, and allow to test different scenarios. Lake numerical models play an increasingly larger role in water resources management and the results of such models are commonly integrated into a decision support system to meet water quality regulatory requirements (Lung, 2001; Trolle et al., 2014).

A water quality model (WQM) is an integrated simulation model, composed of two and in some cases of three sub-models or modules: (1) the hydrodynamic module, which determines the velocity field, thermal structure and turbulent mixing in the lake, (2) the biogeochemical module, which simulates transport, dispersion and the growth or decay processes of the relevant quantity (i.e. contaminants, plankton), and in some cases (3) the sediment transport module, which simulates the transport-dispersion, sedimentation, and resuspension of suspended particles (Rajar & Cetina, 1997). The modelling of biogeochemistry and sedimentation depends entirely on the hydrodynamic circulation and turbulent mixing obtained by the hydrodynamic module (Nihoul et al., 1993). Apart from particular cases where the concentration of a particular substance significantly influence water density and its circulation (Freeman et al., 2015; Kjaran et al., 2004) and accepting to neglect the effect of suspended particle on shortwave penetration into the water column (Heiskanen et al., 2015; Rinke et al., 2010) , the hydrodynamic module can be also run as standalone. WQMs often include other several coupled submodules for different physical, chemical, biological process, such as wind wave, ice cover, sediment diagenesis and submerged aquatic vegetation module. As an example, figure 1.1 illustrates the major component of the model AEM3D (3D-Aquatic Ecological Model).

WQMs can be classified based on their dimensionality. Mix box models, also mentioned as zero-dimensional (0-D), consider vertical and horizontal conditions in the lake as homogenous.

One-dimensional (1D) models provide a realistic representation of stratification and mixing processes in lakes (Hamilton et al., 1997; Imberger & Patterson, 1989) and they are suitable to investigate vertical heterogeneous conditions. However, in lakes characterized by significant differences between pelagic and shore zones or by complex morphometry the vertical 1D assumption may be restrictive and the impact of lake morphometry and hydrodynamic on ecological processes not negligible (Fragoso Jr et al., 2008; Kalff, 2002; Missaghi & Hondzo, 2010; Wetzel, 2001). Hence, horizontal bi-dimensional (2D) models or three-dimensional (3D) models can then offer more insight in the factors determining heterogeneous conditions (Fragoso Jr et al., 2008). Whereas 2D models are more suitable in shallow lakes where vertical differences along the water column are negligible, 3D models are required in stratified deep or medium-deep lakes allowing for a comprehensive representation of heterogeneous conditions both vertically and horizontally.

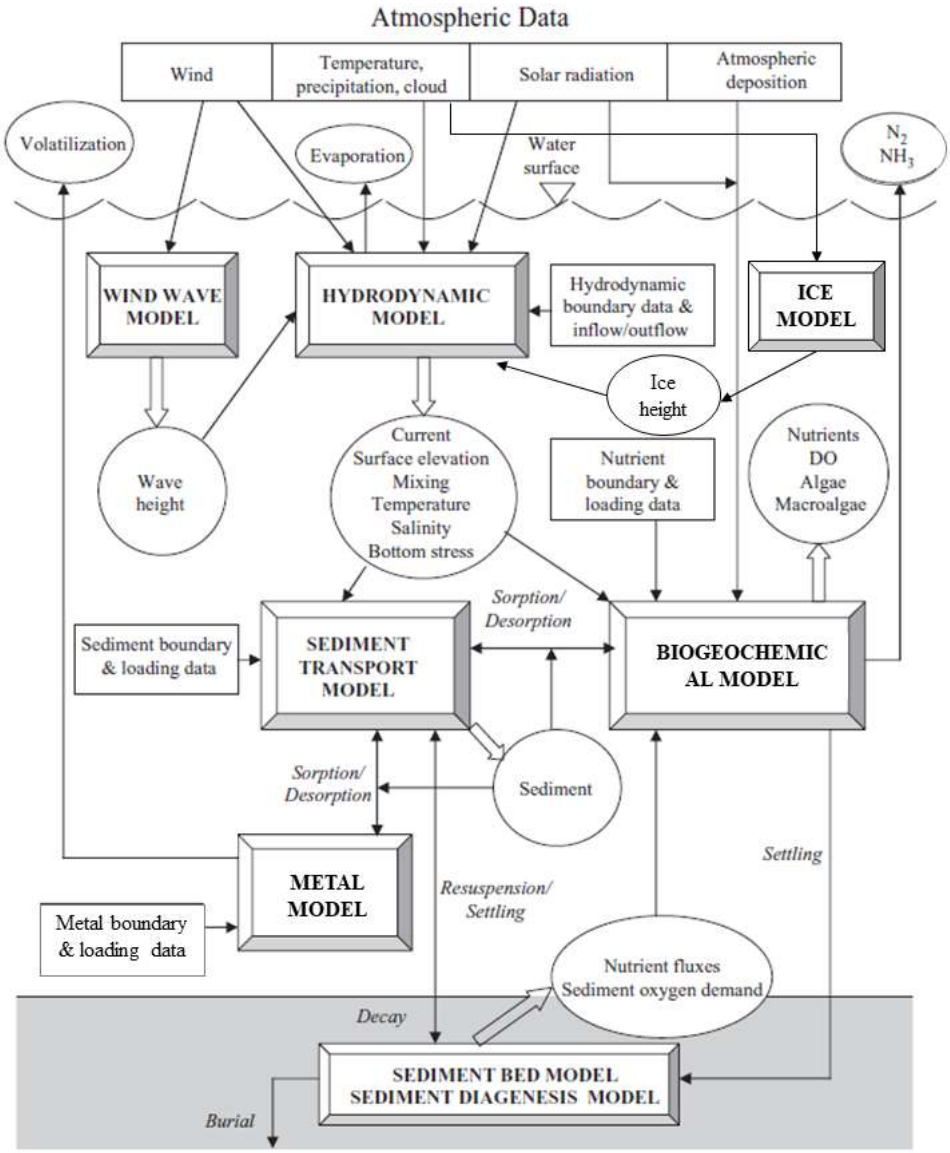

Figure 1.1: Major components (sub-models) of the model AEM3D.

The rapidly advancing computing power and improvements in 3D-WQMs in the past two decades have provided more opportunities to use them for lakes and reservoirs. 3D-WQMs are in particular fundamental tools to describe the individual morphological features of morphologically complex lakes, e.g. bays and sills, and to capture their significant hydrodynamic gradients and water quality heterogeneity. However, only few studies exist that attempt to provide a characterization of the spatiotemporal variability of hydrodynamic and ecology in morphologically complex lakes (Leon et al., 2011; Missaghi & Hondzo, 2010) and they are limited to the example of Great Lakes (Lake Minnetonka and Lake Erie). Moreover, none of these studies has considered the importance of ice cover on lake hydrodynamic and biogeochemistry.

Therefore, the correct simulation of ice cover formation is an important requirement for the correct description of the hydrodynamic and ecological processes in lakes that freeze partially or completely. The formation of ice cover on lakes alters indeed heat and energy transfer with the water column, affecting thus hydrodynamics, the seasonal development of stratification and related ecosystem processes. The development of partial ice cover contributes to create really spatial heterogeneity in the system since it determines completely different conditions in terms of light availability, temperature and turbulence for the phytoplankton growth within the lake. Furthermore, ice cover slows lake circulation and reduces vertical mixing (Fujisaki, Wang, Bai, Leshkevich, & Lofgren, 2013).

In this study the water quality model AEM3D coupled with an ice model was applied to the morphologically complex lake Lower Lake Constance (LLC, 9°18´E, 47°39´N, 62 km^2) with its 3 sub-basins, 2 peninsulas (Reichnau and Mettnau), 87 km of shoreline. The lake's measured data reflect a large temporal and spatial variability between the lake's sub-basin in terms of thermal structure, phytoplankton community and nutrient distribution (IGKB, 2018) and they raise the needs to better understand the spatiotemporal variability in the lake, its drivers and response to environmental changes. Hence, the results of multi-annual continuous simulations of ice cover formation, inter-basin exchange and phytoplankton community were compared between years and between lake sub-basins. Moreover, the response of the lake physic to climate change was assessed with simulations of climate warming and water level scenarios.

1.1 Context and scope of the study

The study presented here was undertaken in 2017 – 2021 as a contribution to the Research Training Group (RTG) "R3 – Responses to biotic and abiotic changes, Resilience and Reversibility of lake ecosystems" founded by the German Research Foundation (DFG). The RTG aims to improve the understanding of the response of ecosystems to changing conditions to predict the impact of environmental changes or restoration measurements.

During the last centuries, lake ecosystems have been affected by a multitude of environmental stressors (e.g. eutrophication, climate change, neobiota), those impact is really difficult to be assessed as the ecosystem response encompasses the response at several level of the ecological organization (Oliver et al., 2015). For instance, depending on the lake abiotic conditions, environmental stressors cause very different response pattern of the ecosystem (Genkai-Kato et al. 2012, Hilt 2015). Hence, in morphologically complex lakes, where large horizontal gradients of abiotic parameters between sub-basins exists, we expect different responses within the lake to the same environmental stressor.

In order to predict ecosystem development, it is therefore important to increase our understanding of how spatiotemporal variability of abiotic parameters respond to environmental changes. In this thesis we investigate, on the example of morphologically complex lake Lower Lake Constance, the processes that cause the spatiotemporal heterogeneity between lake sub-basins at inter-annual and seasonal scales. We study spatiotemporal variability in ice cover, thermal structure and inter-basin water exchange as important criteria for the distribution of phytoplankton and nutrients and investigate their spatiotemporal response to climate change.

1.2 Dissertation outline

Along with the introduction (Chapter 1), this thesis consists of three chapters that each have been prepared as independent manuscripts and submitted or ready for submission for publication in peer-reviewed journals. Each chapter is, therefore, in the style of a manuscript published or prepared for the specific journal. The three chapters (2-4) provide research methods and results of

the application of the 3D-water quality model AEM3D to simulate the spatiotemporal conditions in Lower Lake Constance.

In Chapter 2, the model AEM3D coupled with an ice model (3D-Aquatic Ecosystem Model, AEM3D) was calibrated and validated to simulate nine consecutive years of thermal structure and the spatial distribution and temporal course of ice cover in the three basins of Lower Lake Constance (LLC). The ice information gathered from citizen reported data showed that the different basins do not necessarily freeze each year and are characterized by a large inter-annual and spatial variability of ice cover. Model results are compared to observations of water temperature and ice cover in the three lake basins of LLC to test model performance with respect to inter-annual variability and spatial heterogeneity of the thin ice cover that develops in a lake with complex morphology, as prerequisite for further investigations with the model.

In Chapter 3, multi-annual hydrodynamic simulations with AEM3D under current and possible future conditions were then combined with numerical tracer experiments to study the seasonal pattern of inter-basin exchange in LLC and its modification due to climate warming and associated changes in hydrology. The study focused on the water exchange between the sub-basins Zeller See and Gnadensee, separated by a shallow sill, and between this latter and the river Seerhein. We expect that the water exchange between Gnadensee and Zeller See and the entrance of water from the river Seerhein in Gnadensee have a seasonal pattern linked to the one of lake's water level, thermal stratification and winter ice cover formation. We also hypothesized that climate warming and water level changes can alter them not only in absolute terms but also their seasonal patterns. For example, the reduction of ice cover formation in a warmer climate could enhance the lateral winter exchange between the two basins, whereas lower summer water level may imply larger horizontal differences of dissolved substances and organisms between lake sub-basins.

In Chapter 4, we applied the model AEM3D to simulate water quality and phytoplankton community in the three sub-basins of LLC. This study was the first investigation that provided a characterization of the phytoplankton community and nutrient distribution in the lake. The complex morphometry of the lake causes difference in hydrodynamic conditions and thermal structure among its three sub-basins leading also to large spatial gradients in water quality and phytoplankton community. Here, we assessed if the simulation of the spatiotemporal dynamics of water quality and phytoplankton community can compare well with the field data in all the three sub-basins in two years with different meteorological forcing, flow dynamics and ice cover formation.

The final chapter (Chapter 5) summarizes the results and discusses their implications, with an outlook for further research ideas.

2

Modeling inter-annual and spatial variability of ice cover in a temperate lake with complex morphology

I. Caramatti, F. Peeters, D. Hamilton, & H. Hofmann

Journal of Hydrological Processes (2020), **34**, 691-704

Abstract

The formation of ice cover on lakes alters heat and energy transfer with the water column. The fraction of surface area covered by ice and the timing of ice-on and ice-off therefore affects hydrodynamics and the seasonal development of stratification and related ecosystem processes. Multi-year model simulations of temperate lake ecosystems that freeze partially or completely therefore require simulation of the formation and duration of ice cover. Here we present a multi-year hydrodynamic simulation of an alpine lake with complex morphology (Lower Lake Constance, LLC) using the three-dimensional (3D) model AEM3D over a period of 9 years. LLC is subdivided into three basins (Gnadensee, Zeller See and Rheinsee) which differ in depth, morphological features, hydrodynamic conditions, and ice cover phenology and thickness. Model results were validated with field observations and additional information on ice cover derived from a citizen science approach using information from social media. The model reproduced the occurrence of thin ice as well as its inter-annual variability and differentiated the frequency and extent of ice cover between the three sub-basins. It captured that full ice cover occurs almost each winter in Gnadensee, but only rarely in Zeller See and Rheinsee. The results indicate that the 3D model AEM3D is suitable for simulating long-term dynamics of thin ice cover in lakes with complex morphology and inter-annual changes in spatially heterogeneous ice cover.

2.1 Introduction

The presence, formation and duration of ice cover substantially affects mixing conditions and biogeochemistry of lakes during winter months (Hampton et al., 2017). Furthermore, timing and duration of ice cover have a substantial influence on seasonal plankton succession, on the duration of the growing season and oxygen depletion, and thus also on the occurrence of anoxia in deep water.

During ice cover, the water column hydrodynamics are significantly modified by lack of wind stress at the water surface, which decreases vertical mixing (Fujisaki et al., 2013). Ice and snow cover limits penetration of solar radiation into the water column (Gerbush et al., 2008) and reduces the exchange of water, heat and gases (Loose et al., 2009). However, clear ice conditions can be favorable for winter phytoplankton blooms, since the water column is inversely thermally stratified and vertical mixing is limited (Vanderploeg et al., 1992; Lizotte et al., 1996; Arrigo et al., 2012; Hampton et al., 2017).

Climate change is likely to affect lake ice cover due to a predicted increase of air temperature in winter. This will cause a reduction in the occurrence of ice cover related to a delay in ice-on, earlier ice-off and thinner ice cover (Magnuson et al., 2000; Hodgkins et al., 2002; Austin & Colman, 2008; Dessai et al., 2009; Mishra et al., 2011; Hamilton et al., 2018).
Ice cover in European alpine lakes as well as in lakes worldwide (Magnuson et al., 2000; Weyhenmeyer et al., 2007; Wang et al., 2012; Sharma et al., 2019) has decreased significantly in the past 50 years associated especially in lakes with seasonally and inter-annually intermittent formation of ice (Franssen & Scherrer 2008). Earlier ice breakup may lead to longer periods of water column stratification, warmer surface water temperature and increased heat storage in the lake during summer (O'Reilly et al., 2003; Livingstone, 2003; Mishra et al., 2011). Furthermore, a shorter duration of ice cover causes an extension of the stratified period and thus the growing season, which increases the probability of the development of anoxic conditions in deep waters at the end of the growing season (Livingstone, 1993). Assessment of the implications of global change, in particular climate warming, on hydrodynamics, primary production and water quality can be aided by numerical models that simulate ice-cover in temperate lakes with seasonal ice cover (Oveisy et al., 2012). Furthermore, coupled hydrodynamic models that simulate spatial and

temporal evolution of thin ice (< 10 cm thickness) are required to assess the climate warming impacts on the water column.

A wide variety of lake models has been developed to simulate hydrodynamics, thermal stratification and water quality in lakes. One-dimensional models are based on the assumption that horizontal gradients are negligible and that the vertical mixing can be described as a 1D process (Perroud et al., 2009; Kirillin et al., 2011; Oveisy & Boegman, 2014b; Yao et al., 2014). These models have difficulty in describing deep vertical mixing mechanistically because boundary mixing, the dominant cause of vertical mixing in the hypolimnion (Goudsmit et al., 1997), and internal waves, the main sources of kinetic energy in deep waters, are inherently three dimensional processes (Goudsmit et al., 2002). In large lakes or those with complicated morphology, 3D hydrodynamic models can capture the spatial variability of physical and biogeochemical properties, and overcome the difficulties described above for 1D models. However, it is quite common to investigate the long-term trend of ice cover with 1D models (Fang & Stefan, 1996; Duguay et al., 2003; Dibike et al., 2012; Yao et al., 2014) because multi-year simulations with 3D models require a high computational time.

Application of 3D models to simulate multi-year conditions in mid-latitude, temperate lakes that freeze partially or completely need to consider ice formation (Oveisy et al., 2014a) to adequately reproduce not only winter conditions but also the seasonal changes in stratification after ice-off. 3D hydrodynamic models coupled with an ice formation module have the potential to simulate not only the development and thickness but also the temporal evolution of the spatial distribution of the ice cover in lakes.

One of the first applications of a three dimensional ice simulations used a four-layer model (atmosphere, snow, ice and ocean) to qualitatively simulate the spatio-temporal evolution of ice cover in Arctic and Antarctic lakes (Parkinson & Washington 1979). More details of the ice-formation process were captured with the snow and ice version Dynamic Reservoir Simulation Model (DYRESM) by Patterson and Hamblin (1988), although the model was monodimensional. It incorporates a thermodynamic lake mixing model of the water column and it considered the 2-dimensional effect of partial ice cover. In Rogers et al. (1995) the Mixed Lake with Ice (MLI) cover model extended the DYRESM model, including new processes such as snowmelt due to rain, formation of white ice, and variability of snow density and albedo, specifically for mid-latitudes lakes. Oveisy et al. (2012) incorporated the ice-formation model of

Rogers et al. (1995) in the 3D-hydrodynamic model Estuary and Lake Computer Model (ELCOM), extending its application to 3D ice-formation studies. This coupled model was validated by comparing model simulations with observations in a large lake (Ontario) and a small lake (Harmon, British Columbia, Canada) for one winter (Oveisy et al., 2012). Afterwards, Oveisy et al. (2014a) used the ice module coupled to ELCOM to investigate the effect of ice cover on the hydrodynamics and water quality in Lake Erie. ELCOM has recently been revised and renamed as the Aquatic Ecosystem Model, AEM3D (Hodges & Dallimore, 2018), which is based on the former model ELCOM, including the ice-formation module of Oveisy et al. (2012). There are several other ice models coupled with 3D hydrodynamic model, for example the 3D ice-formation model used in Wang et al. (2010) and in Fujisaki et al. (2012). They both used the 3D Princeton Ocean Model (POM) coupled with the ice thermodynamic formulation of Hibler (1979). This model allows for dynamic advection of ice but it is mostly used for coarse-resolution simulations in large systems (i.e. oceans, Great Lakes).

ELCOM has been used widely to represent the thermal structure and circulation patterns in many lakes (Leon et al., 2012) and has also been applied to address several research questions in the deepest basin of Lake Constance (Fig. 2.1), Upper Lake Constance, (Appt et al., 2004; Eder et al., 2008; Lang et al., 2010; Dissanayake et al., 2019). But none of these studies focused on ice formation, cover and break-up, or on Lower Lake Constance (Fig. 2.1), the shallowest basin of Lake Constance, that experiences occasional ice cover in winter. The correct simulation of ice formation in this lake is an important requirement for further assessments of the implications of environmental changes on the system and to compare them with the response to the same forcing of the deeper neighboring system, Upper Lake Constance. The possibility to couple the hydrodynamic model ELCOM, together with its ice module, to a water quality model rendered it a suitable tool for further research applications to Lake Constance. Therefore, the understanding of the possible alterations of Lake Constance ecosystem due to environmental changes and the ecological, cultural, social and economic implications are relevant, since Lake Constance is a vital resource for human uses (bathing, irrigation, tourism, drinking water supply, winter recreation) and one of the most representative and important wetland habitat for plants and animals in Central Europe.

In this study we applied AEM3D to simulate nine consecutive years of water column thermal structure and the spatial distribution and temporal course of ice cover in the three basins of Lower Lake Constance (LLC). LLC is a temperate lake with a complex shape, subdivided into three basins. The ice information gathered from citizen reported data showed that the different basins do not necessarily freeze each year and are characterized by a large inter-annual and spatial variability of ice cover. Model results are compared to observations of water temperature and ice cover in the three lake basins of LLC to test model performance with respect to the inter-annual occurrence of ice, the areal percentage of ice cover, the representation of differences in the occurrence and extent of ice cover, and the timing of ice formation and ice break-up. The objective of this study is to test whether AEM3D reproduces inter-annual variability and spatial heterogeneity of the thin ice cover that develops in a lake with complex morphology. Moreover, this work provides a unique example of ice model validation with data derived from a citizen science approach.

2.2 Methods

2.2.1 Study site

Lake Constance (9°18'E, 47°39'N) is an Alpine lake of glacial origin located in the southwest of Germany that conjointly borders Switzerland and Austria. Lake Constance (LC) consists of two main parts, Upper Lake Constance (ULC) and Lower Lake Constance (LLC), which are connected by the river Seerhein. ULC has a surface area of 473 km^2 and a maximum depth of about 251 m, whereas LLC is significantly smaller having a surface area of 63 km^2 and maximum and mean depth of 46 and 25 m, respectively. LLC is subdivided into three basins of different depths and hydro-geological features (Fig. 2.1). The southern part, where the river Seerhein enters, is called Rheinsee (RS). It is the deepest sub-basin of LLC and is influenced by the high discharge of the river Seerhein entering the sub-basin in the East and leaving it in the West. RS has a maximum depth of 46 m and it is connected to Zeller See (ZS) in its northern part. This basin is strongly influenced by the exchange with RS and experiences large density-driven intrusions at intermediate depth due to the influence of the Seerhein. The second main

inflow of LLC, Radolfzeller Aach, discharges into this sub-basin. The most northern sub-basin of LLC is Gnadensee (GS) having a maximum water depth of 20 m. GS is the most enclosed sub-basin without significant inflows. It is connected to ZS via a narrow and shallow sill (average water depth of about 4 m; Fig. 2.1), that limits the horizontal exchange of water to the two other basins.

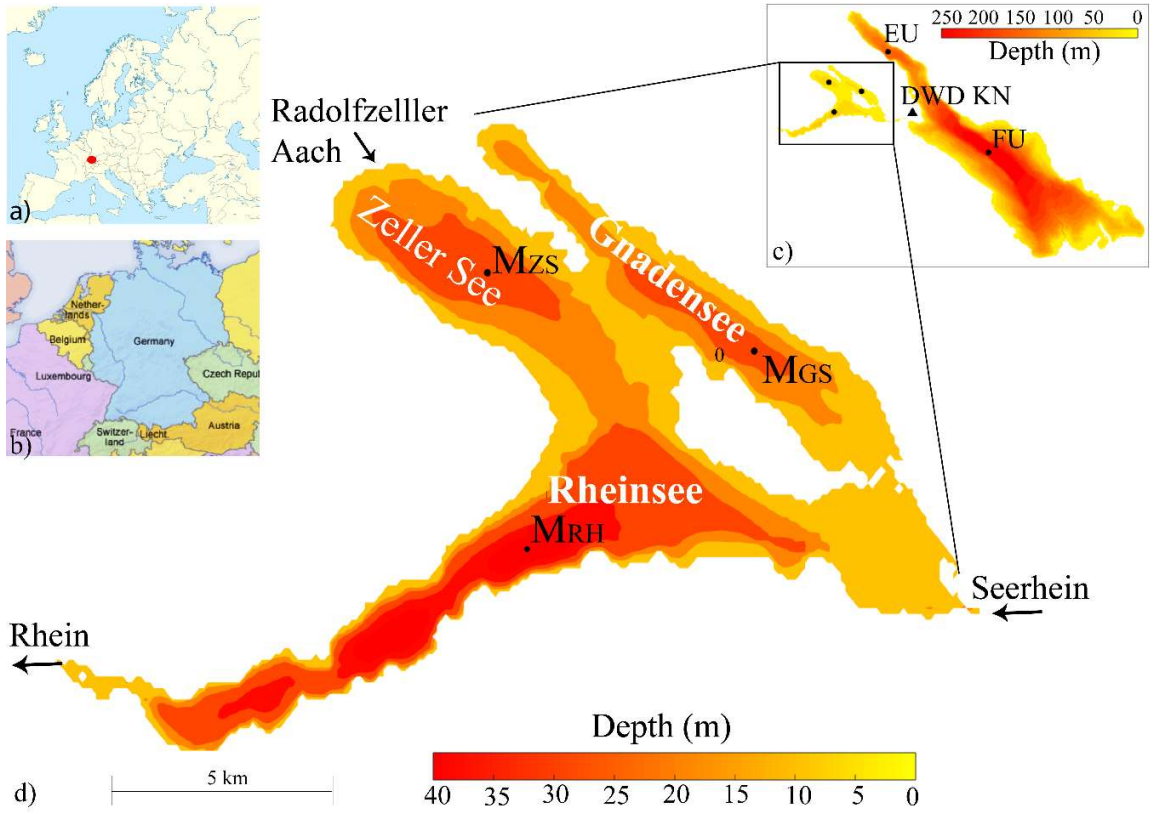

Figure 2.1: Bathymetry of the study site. a) and b) Location of Lake Constance in Europe. c) Bathymetry of Lake Constance and location of the meteorological station (DWD KN) and the stations used to initialize the model applied to LC. b) Bathymetry of Lower Lake Constance, distinguishing between the sub-basins and showing the main inflows and the outflow. Monitoring stations, used to initialize the model applied to LLC, were shown: M_{GS} is in the basin of Gnadensee, M_{ZS} in Zeller See and M_{RS} in Rheinsee.

In contrast to ULC, LLC develops regularly partial or complete ice cover during winter. According to Franssen and Scherrer (2008) complete or almost complete ice cover was observed 36 times in the last century but is less frequent nowadays. During the last decade, only in 2010,

2012 and 2017 ice cover developed in all the three sub-basins of LLC, resulting in almost full ice cover of the entire lake. However, full areal ice cover rarely develops in ZS and RS, while in GS it occurs much more frequently. The official documents from the Water Police of Constance did not describe the formation of ice cover thicker than 10 cm. The collected multimedia information showed that the undeformed ice is the dominating ice form in LLC but along the shores it is common to find brash ice or even pancake ice, formed by the action of wind on the water surface.

2.2.2 Model description

In order to simulate the lake hydrodynamic and thermal structure, we used the three dimensional model Hydrodynamic-Aquatic Ecosystem Model (AEM3D, Hodges & Dallimore, 2018). The hydrodynamic model, based on ELCOM, uses the unsteady Reynolds-averaged Navier-Stokes equations for heat and momentum and considers heat and momentum transfer across the water surface due to wind and atmospheric thermodynamics (Leon et al., 2011). The equations are solved numerically using a Cartesian Arakawa C-grid in the horizontal dimension and the vertical discretization is based on fixed Z-layers (Hodges, 2000). The equations are solved in all wet cells and a turbulent kinetic energy based mixed-layer model is used for vertical turbulent mixing. The model includes Earth rotation, wind stress at the surface, surface thermal forcing, and inflows and outflows. More details can be found in Hodges (1998) and Hodges and Dallimore (2018).

The ice-formation algorithm described in Oveisy et al. (2012) was implemented in the model to simulate ice cover and its influence on lake hydrodynamics and thermal structure. Thus, multi-annual simulations can be performed for water bodies that experience regular ice cover. The ice-model is based on the formulation of Rogers et al. (1995) utilizing a one-dimensional steady-state equation of heat fluxes between ice, atmosphere and water column. The equations are applied independently in each grid cell, allowing spatially variable ice thickness and concentration due to spatially heterogeneous cooling and heat capacity of the surface mixed layer of the lake (Oveisy et al., 2012), without horizontal influence between the grid cells. The model cannot reproduce the horizontal transport of ice and ice deformation, since the advective transport is not modelled.

2.3.3 Model set up

AEM3D was set up for a continuous run from 4 March 2009 to 31 March 2018 based on the availability of meteorological input data and field observations. Because no data on water temperature of the main inflow of LLC, the river Seerhein, was available, the water temperature of the river Seerhein was derived from an independent hydrodynamic simulation of the entire LC (Suppl. 2B).

The computational grid of LLC was described by a regular, horizontal grid of 100 m x 100 m and 79 vertical layers, refined to 0.5 m near the surface and decreasing up to 1 m near the bottom. The two main inflows Seerhein and Radolfzeller Aach, and the outflow of river Rhein (Fig. 2.1) were set as boundary conditions by using the time series of measured discharge and water temperature. In case of Seerhein the water temperature was taken from the output of the simulation of LC. The outflow of LLC was derived from a water balance based on the inflows and the measured change in water level (gauge Berlingen). This approach corrected for discrepancies in the water balance arising from neglecting discharge of smaller tributaries and evaporation from the lake surface. Water temperatures in LLC were initialized using temperature profiles measured with a CTD-probe (Conductivity, Temperature, Depth) at the stations M_{ZS}, M_{GS}, M_{RS}. The model internally interpolated water temperatures over the entire water volume using an inverse distance weighting method. Spatially resolved wind fields were available for ULC (see below) and linearly interpolated to the computational grid. Except for the wind field, the model was driven with horizontally uniform meteorological data. Heat fluxes were calculated from air temperature, relative humidity, cloud cover and solar radiation. Longwave radiation was calculated in the model internally from an empirical relation from the Stefan-Boltzmann equation as a function of air temperature, cloud cover and relative humidity (Hodges, 1998).

A more detailed description of the model parametrization can be found in Tab. 2.4.

2.3.4 Data

Meteorological data

Hourly meteorological data on air temperature (Fig. 2.2), relative humidity, air pressure, cloud cover and solar radiation were available from the climate station in Konstanz maintained by the German National Meteorological Service (DWD: 47°40’390’’N, 09°11’24’’E; 442 m

above sea level; Fig. 2.1). Spatially resolved wind fields were obtained from the numerical weather system of the Consortium for Small Scale Modeling (COSMO), which is operationally run at the National Swiss Weather Service (Doms & Baldauf, 2018). COSMO is a forecasting model to calculate future atmospheric conditions with a temporal output interval of 1 hour and a spatial resolution of 2.2 km (COSMO-2) and, since April 2016, 1.1 km (COSMO-1). The model COSMO-1 is initialized every hour with a field obtained by combining observation data, previous model runs and climatological information, in order to provide higher accuracy.

Inflow and outflow data

Daily or hourly river discharge data and river water temperature data were obtained from different sources: the Landesanstalt fuer Umwelt Baden-Wuerttemberg (LUBW), the Hydrographische Dienst Vorarlberg (VA), and the Federal Office for the Environment (BAFU). The latter also provided daily data on water level of LLC (gauge Berlingen).

Temperature data

Profiles of water temperature are available for station EU and FU in ULC and stations M_{GS}, M_{ZS}, and M_{RS} for LLC. At station EU, data are collected by a thermistor chain with a vertical resolution from 0.5 to 2 m in the upper mixed layer (down to 20 m depth) and a coarser vertical resolution in the hypolimnion. From regular monitoring programs by the IGKB (the International Commission for water protection of Lake Constance) and LUBW, CTD profiles are available for the stations M_{ZS} and M_{GS} and less resolved data at station M_{RS} and FU (resolution 2.5 – 5 m and 5 – 20 m respectively).

Ice data

Data on ice cover have been rarely recorded for Alpine lakes that do not freeze regularly (Franssen & Scherrer, 2008). For LLC, no continuous and systematic records on ice cover exist. However, Franssen and Scherrer (2008) reconstructed the ice history of LLC in the 20th century, combining sporadic records by the Water Police and information from local newspapers. We extended this time series on ice cover by collecting all available information on ice data, e.g., reports of the Water Police, local newspapers, news blogs, and social media for the winters between the years 2010 and 2018. The collected data set was employed to define when ice was abundant and in which lake basins.

The most valuable sources of information on ice cover were from reports of the Water Police. These reports provide a qualitative description of the ice cover pattern for specific dates, mentioning if the frozen areas were safe or not to bear the load of people. This information from the police reports was complemented with information from newspaper articles (Suedkurier Online, St. Gallen Tagblatt), descriptions on blogs and pictures or videos from people spending time on the ice that were posted on social media (Instagram, YouTube). Especially for recent winters, such as in 2017 and 2018, ice data from social media were an important source of information. These data can be assumed as useful information to define the timing of ice-on and -off and whether it is thick enough to bear the load of people.

An additional source of information, especially for the year 2011, were reports of the LUBW which mentioned in their field protocols the accessibility of the different monitoring stations in the three sub-basins of LLC. A detailed list of the sources and the collected data is provided in Tab 2.3. In some years, we could not find any information in any report or in the media about ice cover the sub-basins of LLC. In such cases, we assumed that no significant ice cover in the specific lake basin was formed.

We checked whether satellite images could provide additional information on the occurrence of ice and the spatial distribution of ice cover. But most of the time obscuring effects due to cloud cover and fog typical for LLC during wintertime as well as difficulties in distinguishing blue ice from water prevent obtaining better information on ice than evaluated from the ground truth data.

Ice data was interpreted with respect to the reference scale of the US Army Corps of Engineers (CRREL-US Army Corps of Engineers). They defined ice ≥5 cm as safe ice, thick enough to bear the load of a single person per square meter. Hence, the distinction made by the Water Police between safe and dangerous frozen areas was interpreted in the same way: the frozen areas stated as safe in the ice reports provide information on the presence of ice with a thickness ≥5 cm, while dangerous frozen areas refer to thinner ice. Pictures or videos with only a few people on ice were referred to thinner ice (~3 cm) in case they were taken before the Water Police mentioned safe ice. The available data do not provide information on very thin ice (<3 cm), because it is too dangerous to attract people to walk on it and thus unlikely to find pictures of people on the ice. Further, the Water Police typically does not report on very thin ice.

The onset of observed ice cover, $ONSET_{obs}$, was defined as the date of the first observation of ice cover within the respective winter. This information was always a picture showing people on the ice along the shores, where ice typically starts to freeze and thus safer than further offshore. These pictures at $ONSET_{obs}$ were always taken before the Water Police reported safe ice. Hence, ice thickness at $ONSET_{obs}$ was assumed to be ~3 cm in accordance to the interpretation of the ice data described above. The onset of modelled ice cover $ONSET_{sim}$ was defined as the date at which the simulated mean ice thickness over the ice area was thicker than 3 cm and covered at least 10% of the surface area of the basin. $ONSET_{sim}$ was evaluated separately for each basin for the winters 2017 and 2018, when the most frequent ice data was available.

2.2.5 Analysis of the air temperature data

Air temperature is a key parameter that relates to the formation and break-up of ice (Franssen & Scherrer 2008). A derived parameter often used for this purpose is the sum of Negative Degree Days (NDD) that discriminates very cold winters from mild ones. The sum of NDD was computed from the time series of the daily mean air temperature according to Franssen and Scherrer (2008) during the period 1 October to 31 March for each of the simulated winters (Fig. 2.2). In the same study, Franssen and Scherrer (2008) defined that for Lower Lake Constance the sum of NDD for which the lake freezes with a probability of 10, 33, 50, 67 and 90% are respectively 128, 156, 170, 187 and 228°C·days, respectively. The sum of NDD corresponding to a probability of 10% (128°C·days) was used to discriminate between cold and mild winters.

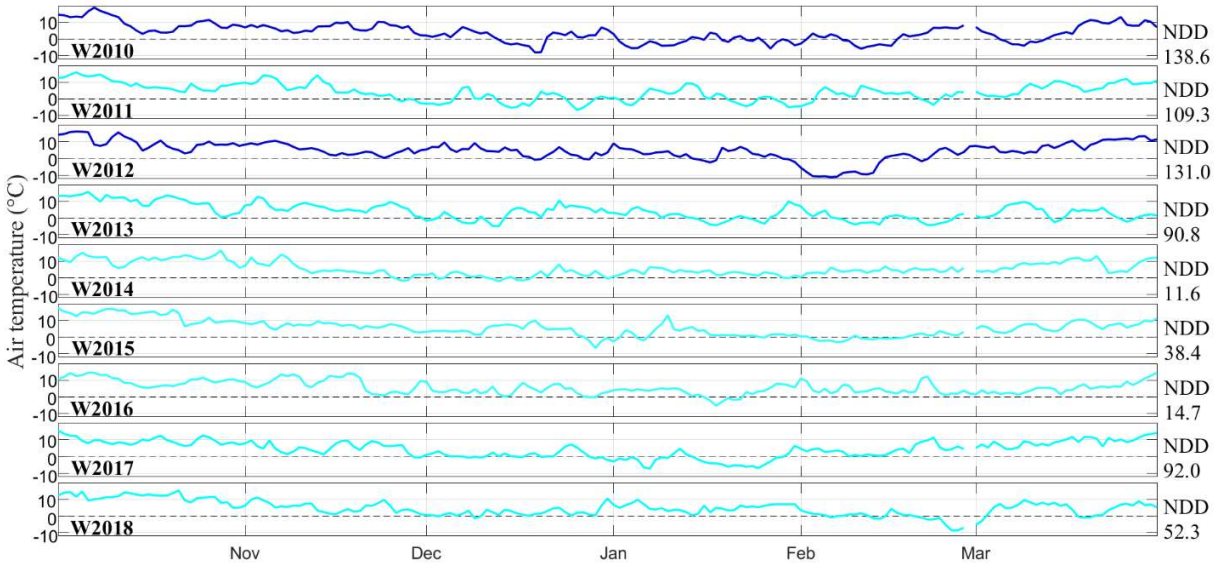

Figure 2.2: Time series of the air temperature at the DWD-station Konstanz between 1 October and 31 March for each of the simulated years. The sum of negative degree days (NDD in °C·days) is indicated on the right hand side of each panel. The color coding classified winters in two categories according to the sum of NDD: NDD <128 as mild winters and NDD ≥128 as cold winters.

2.2.6 Model validation: simulated thermal structure

At stations M_{GS} and M_{ZS} the results of the model simulations were compared to temperature profiles focusing on different stratification regimes of three consecutive years (2010, 2011, 2012): mixed or inversely-stratified at the beginning for December - March; initially stratified in April - May; stratified in June - September; stratified before the overturn in October-November.

The accuracy of the simulated thermal structure was evaluated using the root mean square error (RMSE) between each temperature profile and the output of the model at the same date t_j:

$$RMSE(t_j) = \left[\frac{1}{N}\sum_{i=1}^{N}(x_i(t_j) - y_i(t_j))^2\right]^{1/2} \quad (1)$$

where x_i and y_i are the measured and simulated temperatures at the date t_j, respectively. Both model and data were interpolated to a vertical grid of 0.1 m, where i=1,..,*N* represents the number of points in the vertical profile. The RMSE of each of the four periods was computed as the average RMSE of the profiles in each period.

The accuracy of the water temperature simulation in winter was computed as the RMSE between the modeled temperature at 1 m depth, y_s, and the temperature observations at 1 m depth, x_s:

$$RMSE_{surface} = \left[\frac{1}{M}\sum_{j=1}^{M}(x_s(t_j) - y_s(t_j))^2\right]^{1/2} \quad (2)$$

where *M* is the number of temperature profiles collected in the winter 2010, 2011 and 2012.

2.2.7 Model validation: simulated ice cover

Simulated lake ice cover was validated with the available observations between the winter 2010 (W2010) and 2018 (W2018; Fig. 2.4). We used the notation WYYYY to designate the time period from 1 December of the previous year to 30 April of the named year YYYY. Although the lack of detailed records documenting the ice timing, the sourced validation data provided a very useful avenue for qualitative information on the abundance of ice cover.

The model output consists of a time series on the spatial distribution of ice thickness in LLC. The simulated ice thickness was subdivided into four classes: 1 - 3 cm, 3 - 5 cm, 5 - 7 cm and ≥ 7 cm. Then, the simulated percentage of the lake area covered by ice of a specific thickness class was computed as the ratio between the number of ice covered surface cells of the considered class and the overall number of surface cells. In addition to the surface fraction covered by ice of different thickness, ice volume was calculated as well.

The simulated ice cover was compared to observations of the different lake basins separately (Fig. 2.5). The amount of ice in each basin was expressed as the specific volume of ice cover (cm), which was defined as the ratio between the simulated ice volume in each basin and

the corresponding surface area. This allows a comparison of the volume of ice between basins with different surface area.

A detailed comparison between model and observation on the spatial distribution of ice coverage and thickness in LLC was conducted for three different dates in W2017 (21, 26 and 29 January), because for these dates the reports from the Water Police were particularly detailed.

2.3 Results

3.3.1 Long-term simulation of thermal structure

Lower Lake Constance (LLC) shows stable stratification during the summer and inverse stratification during the winter months, and further, can be considered as dimictic showing complete mixing during autumn overturn as well as in spring after ice-off. According to the model output, inverse stratification develops 10-15 days before the occurrence of ice cover and it is established in the top 1-2 m below the ice (Figs 2.10, 2.11). The inverse stratification disappears due to vertical convective mixing during ice-off.

Model results and observations were compared at two sites (M_{GS} and M_{ZS}) and for three consecutive years (2010, 2011, and 2012) to validate the model performance in terms of thermal structure throughout the season and among years (Fig. 2.3). The simulated temperature profiles during ice-free periods in winter adequately represented conditions observed in the water column, while the simulated temperatures during the stratified period deviated more from observations.

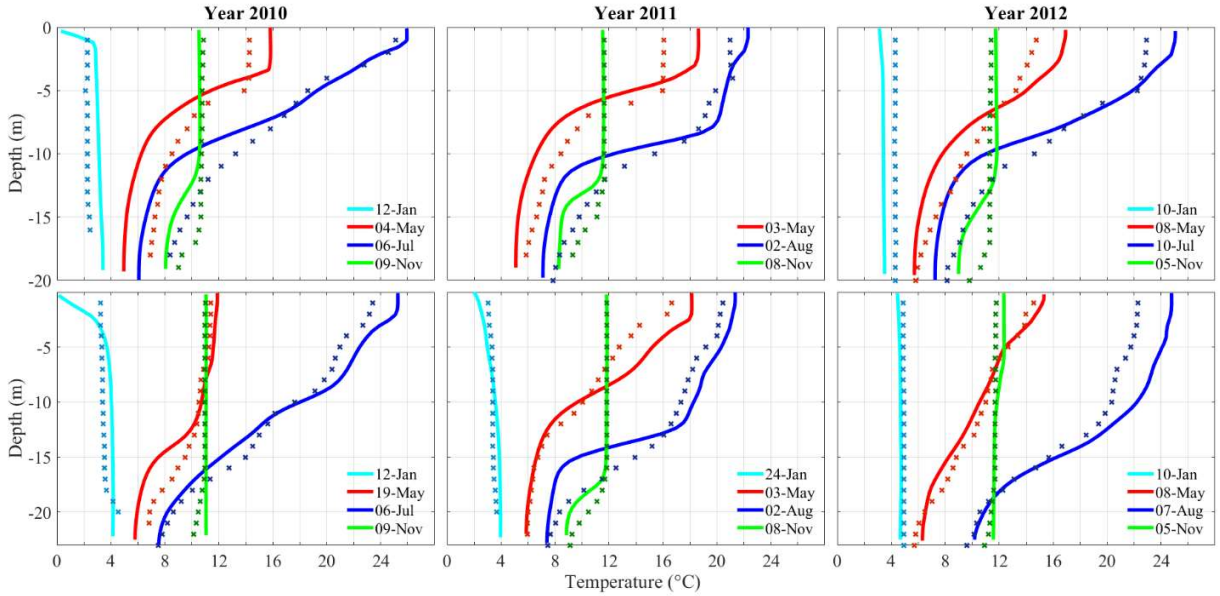

Figure 2.3: Seasonal differences in thermal structure and model validation. Comparison of observed (continuous line) and simulated (dotted line) temperature in Gnadensee (GS) and Zeller See (ZS) for characteristic snapshots (thermal structure) of three consecutive years (2010, 2011 and 2012).

The agreement between simulated thermal structure and monthly temperature profiles was evaluated using the root mean square error (RMSE). A mean RMSE was computed for each of the four periods described above (December-March; April-May; June-September; October-November) and is presented in Tab. 2.1. The model represents the thermal structure most accurately between October and March, with a mean RMSE between 0.37 and 1.08°C in ZS and 0.97 and 1.82°C in GS. During the winter months (from December to March), the mean RMSE was 0.85, 0.37, 0.45 °C in ZS for the years 2010, 2011, 2012 and 1.03, 0.98 °C in GS for the years 2010, 2012 (no data available in 2011). The simulation was least accurate in the period June to September, with a maximum mean RMSE of 1.49 in M_{ZS} and 2.34°C in M_{GS}. In each case, the model reproduced the thermal structure more accurately at station M_{ZS} than M_{GS}. In the period December to March, the $RMSE_{surface}$ at 1 m depth was 0.80°C and 0.89°C in M_{ZS}.

Table 2.1: Model validation based on temperature. RMSE between measured and simulated temperature profiles of the sub-basins Gnadensee and Zeller See.

Gnadensee				
RMSE (°C)	Dec. - March	April - May	June – Sept.	Oct. – Nov.
2010	1.03	2.16	2.26	1.03
2011	-	2.01	2.06	1.82
2012	0.98	1.59	2.34	0.97

Zeller See				
RMSE (°C)	Dec. - March	April - May	June – Sept.	Oct. – Nov.
2010	0.85	1.12	1.32	1.02
2011	0.37	0.97	2.22	1.08
2012	0.45	0.51	1.49	0.35

2.3.2 Inter-annual variability of ice cover

Between 2010 and 2018, winters ranged from cold to mild, causing a wide range of ice coverage and duration. W2010 and W2012 can be regarded as cold winters with NDD ≥128°C·days. The other winters were characterized by a smaller sum of NDD and can be then considered as mild winters, in particular W2014, W2015 and W2016 with a sum of NDD <40°C·days (Fig. 2.2). During the simulated decade, abundant ice cover was observed in W2010, W2011, W2012 and W2017. Less ice cover was observed in W2016 and W2018, during which significant ice cover only developed in GS. For the remaining years, no information was documented, suggesting no or at most very little and intermittent ice cover.

The pattern of ice occurrence simulated with AEM3D agrees rather well with the observed pattern (Fig. 2.4). The simulated ice coverage of LLC showed a marked inter-annual variability. In the years when abundant ice cover was observed, the model results showed the largest extent of ice, with up to 80-90% coverage of the lake surface. In W2014 and W2016, an ice thickness >5 cm did not form or covered <20% of the lake surface area.

Ice coverage does not contain information on ice thickness and ice cover can be misleading with respect the amount of ice formed. For example, in W2015 a large percentage of

the ice cover was thin, with only 13% of the ice cover of thickness ≥5 cm. While the percentage of lake ice coverage in W2015 was similar to that in W2011, the corresponding simulated ice volume was only half with respect to W2015. The pattern of inter-annual variability in simulated ice volume agrees very well with observations of the abundance of ice cover: the four years for which abundant ice was reported correspond with the largest simulated ice volumes (Fig. 2.4b).

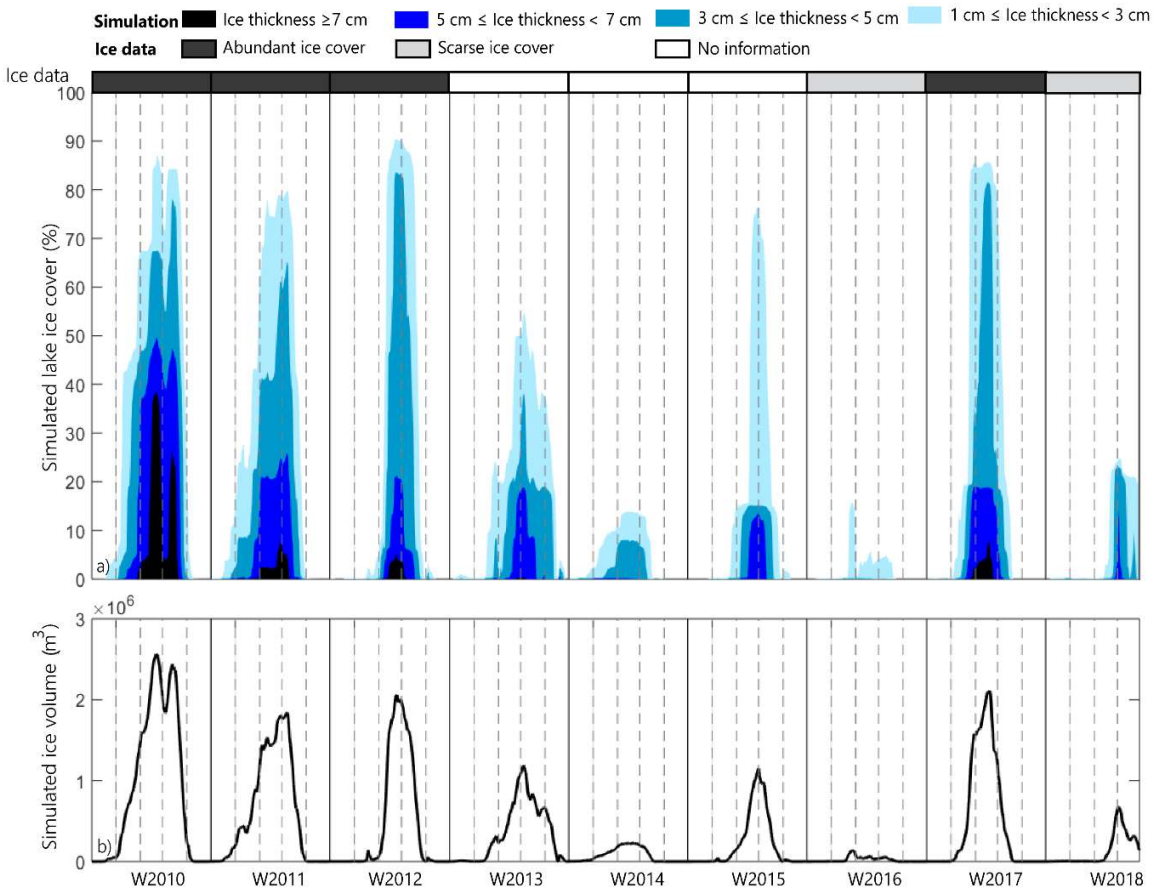

Figure 2.4: Annual variability of ice cover in Lower Lake Constance (LLC) in the period 2010 – 2018. a) Simulated lake ice cover percentage, distinguishing between four categories of ice thickness, compared to observed ice data. b) Time series of the simulated ice volume in LLC.

2.3.3 Inter-basin variability of ice cover

The observations indicate that ice formation and spatial coverage developed differently between the three basins of LLC. Almost complete ice cover regularly develops on GS, which is documented by abundant observations. In contrast to GS, ZS and RS have much less ice cover and the ice forms only infrequently. GS was almost fully ice covered in W2010, W2011, W2012, and W2017, partially frozen in W2018, and barely frozen in areas along the shores in W2016. Ice cover in ZS was observed in W2010, W2012 and W2017, while it was ice free in W2018. Very small ice covered areas were reported in RS in W2012 and W2017, but not in the other years.

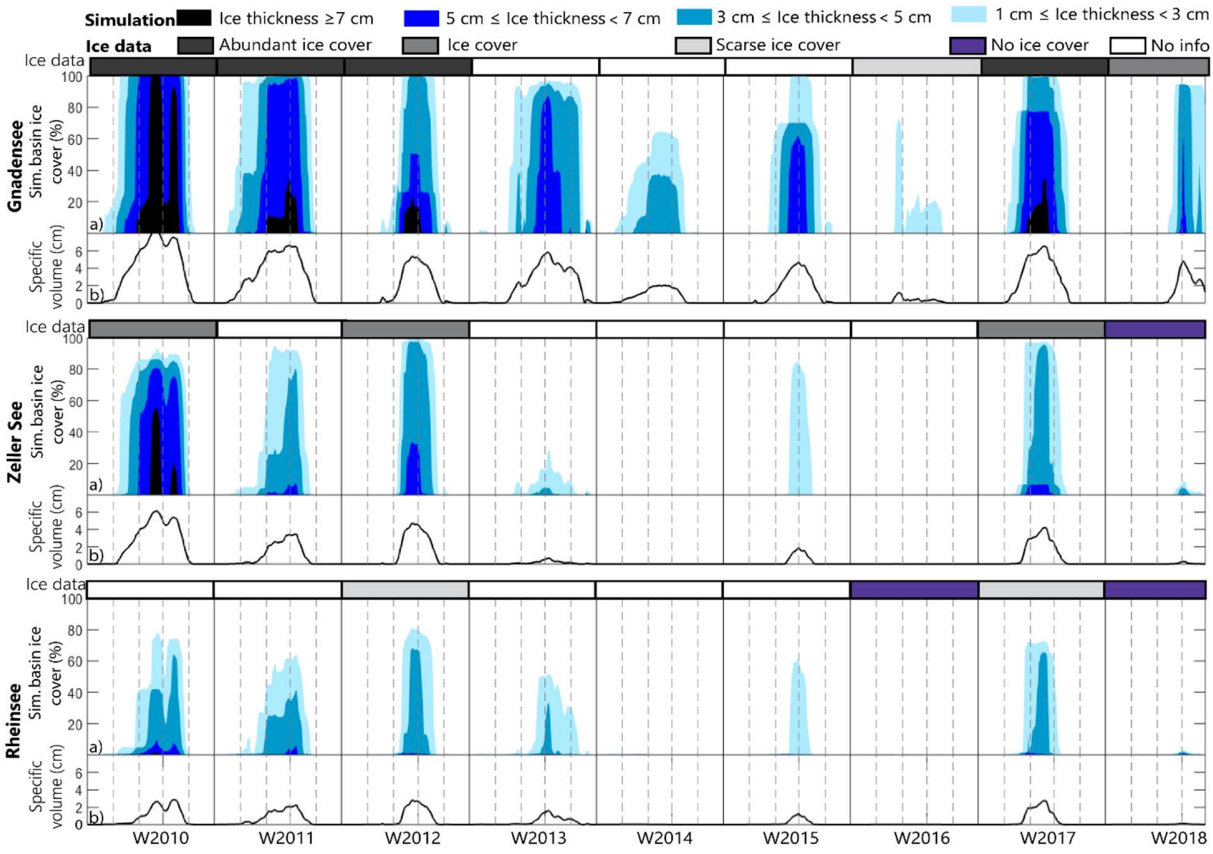

Figure 2.5: Inter-basin and annual variability of ice cover during the observation period (2010-2018). a) Comparison between simulated ice cover (%), distinguishing between four categories of ice thickness, and observed ice data for each of the basins. b) Specific volume given by the ratio between the simulated ice volume and the corresponding surface area of the basin.

Consistent with the data, the model simulation showed a significant difference in occurrence and specific volume of ice among the basins (Fig. 2.5). In the model, a thick ice cover developed in GS almost every winter, except for the W2015 and W2016, when only thin ice was formed. In contrast to GS, ZS was ice covered in the model only in W2010, W2011, W2012 and W2017, and RS developed only thin ice in these years. The model also captured the absence of ice in RS in W2016 and W2018. Furthermore, the model always reproduced thicker ice in GS than in the other basins. Ice ≥5 cm occurred in GS in all winters except in W2014 and W2016. In ZS, ice ≥5 cm was less frequent than in GS and occurred in the W2010, W2011, and W2017. In contrast, in RS ice ≥5 cm was almost never formed, except at very low percentage area in W2010 and W2011. Hence, the simulated specific ice volume was always highest in GS and decreased from GS over ZS to RS (Fig. 2.5b).

A quantitative measure to compare the extent and duration of ice cover between the different sub-basins was defined by counting the number of days during which ice cover exceeds 50% and 80% of the basin surface area. GS showed the highest number of days above these thresholds (Tab. 2.2): 50% of the basin surface area was ice covered every year for 8 to 87 days and 80% of the basin surface area was covered in all winters except in W2014 and W2016. When ice cover was >80% of the basin surface area, it lasted between 28 and 85 days. Ice cover in the other two sub-basins was less extensive (Tab. 2.2). In ZS ice coverage >50% of the surface area occurred for more than half of the winters (W2010, W2011, W2012, W2015 and W2017) and lasted between 21 and 79 days. Periods of ice cover in ZS that exceeded 50%, also exceeded 80%, but for a shorter period, i.e. 10 to 60 days. In RS, 50% of ice cover occurred in the same years as in ZS, and as well in W2013 for7 days. Ice coverage >80% occurred only in W2012 for 8 days. In RS ice was typically formed for shorter periods than in the two other lake basins.

Table 2.2: Number of days during which ice cover exceeds 50% and 80% of the basin surface area. The dash indicates winters that did not exceed the threshold. GS = Gnadensee, ZS = Zeller See and RS = Rheinsee.

(days)	GS >80%	ZS >80%	RS >80%	GS >50%	ZS >50%	RS >50%
W2010	85	60	-	87	79	37
W2011	82	40	-	85	46	35
W2012	41	39	8	47	44	37
W2013	80	-	-	82	-	7
W2014	-	-	-	33	-	-
W2015	28	10	-	57	21	15
W2016	-	-	-	8	-	-
W2017	46	39	-	66	43	36
W2018	38	-	-	39	-	-

Simulated and measured ice cover distributions in the sub-basins were investigated in more detail for two consecutive winters (W2017 and W2018). For these two winters the most detailed information on ice cover were available but the meteorological conditions differed substantially between these years (Figs. 2.2 and 2.6). Moreover, the spatial distribution of ice cover and the timing of ice-on and ice-off differed substantially between the two winters. W2017 was characterized by a long, cold period in January, with almost four consecutive weeks of negative daily mean air temperature and 92°C·days negative degree days between October and March (Fig. 2.2). Ice cover formed in all three sub-basins of the lake. In GS ice records were documented for the entire month of January and February, but only at the end of January in the other two basins. Instead, in W2018 continuous negative daily mean air temperature was recorded for 11 days between 20 February and 2 March and in total 52.3°C·days negative degree days between October and March (Fig. 2.2). In this winter, only GS froze over between the end of February and the first week of March (documented by observations).

The model reproduced well the ice that formed in all three basins in W2017 and only in GS in W2018. In W2017 ice cover reached 100% in GS, with a maximum specific volume (ratio between the simulated ice volume of the basin and its surface area) of >4 cm from 26 January to 28 February and a maximum specific volume of 5.6 cm (Fig. 2.6). In W2018 the ice cover reached almost 100%, but the specific volume >4 cm was present only for a short period (29

February to 5 March) and the maximum specific volume was more than 1 cm smaller than in W2017. In W2017 the model reproduced ice cover in the other two basins too, but the ice volume was considerable smaller: the maximum specific volume was 3.8 cm and 2.5 cm in ZS and RS, respectively.

In GS, the first observation of ice cover ($ONSET_{obs}$) was on 6 January in W2017 and on the 25 February in W2018. The simulated onset of ice cover ($ONSET_{sim}$) was on the 16 January in W2017and on the 25 February in W2018. In GS, $ONSET_{sim}$ was later in W2017 and agreed very well in W2018 with $ONSET_{obs}$. In the other basins, $ONSET_{obs}$ was on 17 January in ZS and on 23 January in RS in W2017, whereas $ONSET_{sim}$ was on 29 January in ZS and 3 February in RS.

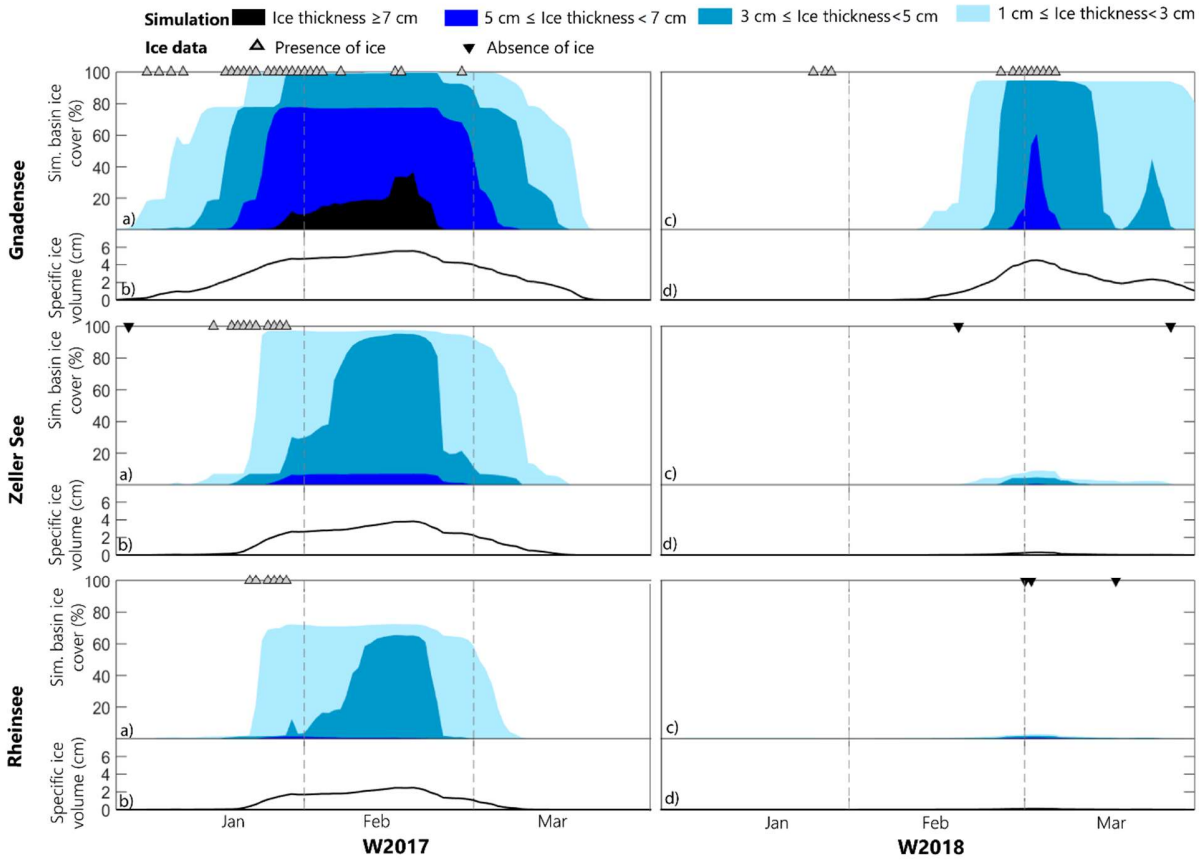

Figure 2.6: Inter-basin variability of ice cover in winter 2017 and 2018. a) Simulated ice cover (%) in Gnadensee (GS), Zeller See (ZS) and Rheinsee (RS) distinguishing between four categories of ice thickness, versus ice data. b) Specific ice volume given by the ratio between the simulated ice volume and the corresponding surface area of the specific basin.

The simulated ice cover was compared qualitatively to the pattern of ice cover derived from the report of the Water Police (Fig. 2.7) in order to validate model results regarding the spatial distribution of ice, ice coverage and timing of ice-on and -off. From the description of the reports, the first dangerous frozen areas (<5 cm) were distributed along the shore of GS on 21 January 2017. A safe frozen area (≥5cm) was observed in the southern part of the basin at this time. After 5 days, the ice around the shore of GS became thicker and extended toward offshore up to 300 m. During that time, the center of the basin was covered by thin ice, regarded as not safe by the Water Police. At the same time, ice started to develop along the shores of ZS and RS. On 29 January, the safe frozen areas along the shores of GS become wider (up to 400 m) and the frozen area in the south enlarged. At this time, the center of the basin was completely covered by ice, but was still regarded as dangerous in the reports. On the last day analyzed, ice cover along the shores of ZS and RS had extended and thickened. The model simulation showed a predominance of ice between 3 and 5 cm in the basin of GS on 21 January (Fig. 2.7). Ice ≥5 cm thick was found in a small area in the southern part of Gnadensee, while the center of the basin was characterized by ice with thickness between 1 and 3 cm. On 26 January, the ice in GS became thicker and reached ≥7 cm in the southern part of the lake. Ice between 3 and 5 cm also extended along the shores of ZS and RS and a layer of thin ice covered this basin completely and almost half of RS. On 29 January, GS was almost covered by ice with a thickness ≥5 cm, beside the area of the sill between GS and ZS. 3-5 cm thick ice was present along the shores of ZS and RS, as well as an extended layer of thin ice.

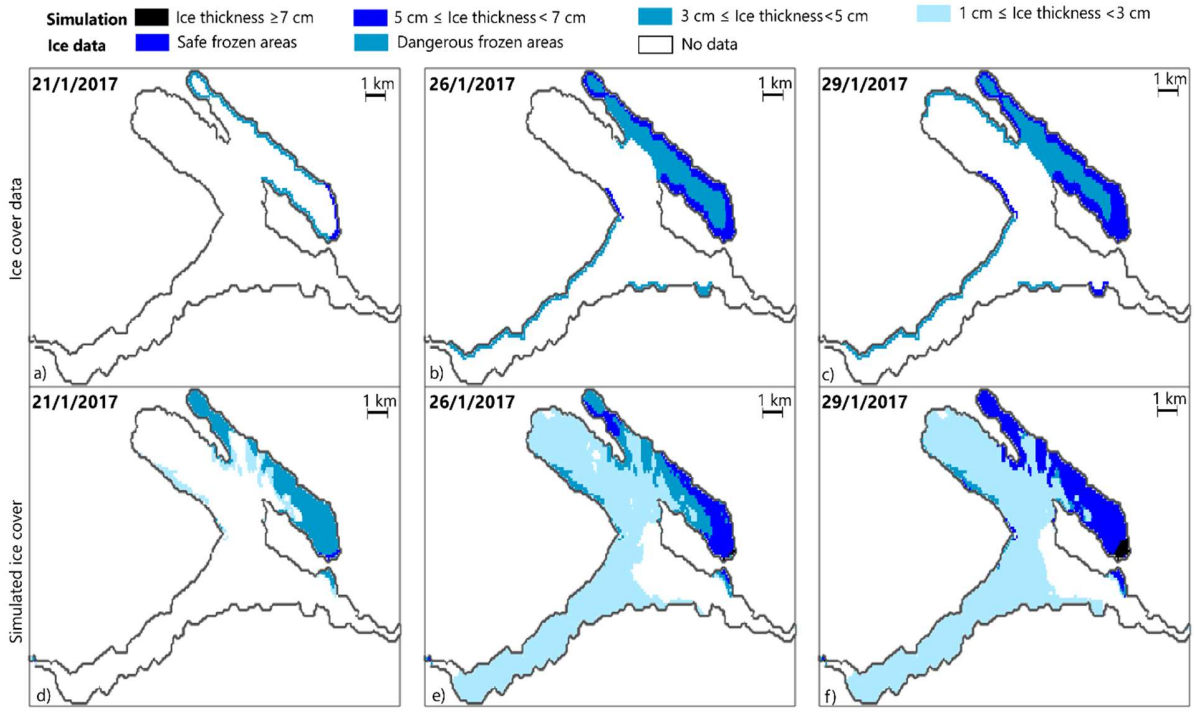

Figure 2.7: Detailed comparison of observed and simulated spatial distribution of ice cover for three days during the formation of ice (21st, 26th and 29th of January 2017).

2.4 Discussion

2.4.1 Ice data

In many studies investigating the spatial distribution of ice, model results have been validated against ice-cover information derived from satellite images. Ground truth data were available in Fujisaki et al. (2013), but not in the studies by Oveisy et al. (2012) and Oveisy et al. (2014a). In LLC, cloud cover and fog are typical features during wintertime, limiting the applicability of commonly used satellite imagery for ice detection. In addition, the differentiation between ice covered areas and open water was not possible, presumably due to the presence of thin black ice without snow cover. The use of multi-sourced data to validate an ice modelling study is an interesting alternative to a remote sensing approach to collect ice data that rendered this work unique in the field of 3D ice modelling.

2.4.2 Model simulations vs. observations

Considerations of the thermal structure

We first investigated the ability of the model to reproduce the seasonal thermal structure of the lake and the surface water temperature, with particular attention to the winter months. The vertical thermal structure during ice-free winters was well reproduced by the model, as indicated by a maximum mean RMSE of only 1.0°C, which is similar to the error obtained in Oveisy et al. (2012). Specifically, the RMSE of the surface water temperature in the ice-free winters was 0.89°C in ZS and 0.80°C in GS. In Oveisy et al. (2014a) the comparison of simulated temperatures with the satellite-derived lake surface temperatures showed a similar deviation (RMSE=0.87°C).

The RMSE obtained in summer periods were larger than in winter because during stratified periods the exact vertical position of the thermocline is difficult to simulate, which is a known challenge. In general, the model showed a tendency to reproduce a deeper thermocline than observations and this deviation was largest in GS, the most enclosed sub-basin. Multi-annual

simulation in Lake Erie showed similar deviations between modelled and observed thermocline depth (Fujisaki et al., 2013).

According to the model in the top 1-2 m of the water column, a weak inverse stratification is established during wintertime (Figs. 2.10, 2.11). The development of inverse stratification starts up to 10-15 days before the formation of ice cover and it disappears during ice-off. Since the sampling interval of the regular monitoring was comparatively large, the probability capturing periods of inverse stratification before ice cover occurs is low, and measurements from the ice are typically not conducted because of safety reasons.

Considerations of the simulation of ice cover

The model demonstrated its sensitivity to the annual variability of climate in reproducing the occurrence of ice in LLC: in W2014, W2015, W2016 and W2018 simulated ice extents were small, whereas they were large in W2010, W2011, W2012 and W2017, which is in accordance with the observations (Fig. 2.3).

The model differentiated frequent and abundant occurrence of ice in GS from less frequent and less abundant ice cover in the other two sub-basins. The simulation results showed that GS was fully covered almost every year, while the other basins were ice-free or characterized by only partial ice cover and thinner ice. Hence, the resulting simulated specific ice volume was always larger in GS than in the other basins. Moreover, the simulated ice cover lasted longer and occurred more often in winters in GS than in the other basins (Tab. 2.2).

The onset of freezing was in reasonable accordance with observations (Fig. 2.6): in W2017 the simulated $ONSET_{sim}$ in GS occurred about 10 days later than $ONSET_{obs}$, while in W2018 $ONSET_{sim}$ coincided with $ONSET_{obs}$. Also in the other two basins, $ONSET_{sim}$ gave reasonable description of the freezing time in W2017 and W2018. The frequently collected data for these two winters allowed a detailed comparison between the simulated and observed timing of ice cover that was not possible in previous studies using the same ice module. For example, in the model application to Lake Erie by Oveisy et al. (2014a) the comparison between data and simulations is based on monthly observations the first of which already indicates a full ice cover with a lake-wide average ice thickness of about 4 cm. In the study of Yao et al. (2014) comparing the application of four different 1D models for multi-years ice simulations, the deviation between data and model on the timing of ice-on and-off was up to 20 days, thus larger than in our study.

The model agreement with the ice data for multi-years simulations resulted to be even more difficult with a 3D model, like in Fujisaki et al. (2013), where the deviations model-data for some years were off of about 30 days.

The model results in the study here not only agreed reasonably well with the observed onset of freezing but also represented well the differences in the spatial ice extent in the three sub-basins at specific dates. The spatial coverage of simulated ice ≥5 cm replicated the frozen area classified as safe by the Water Police, while the dangerous frozen areas overlap with the pattern of the simulated ice with a thickness between 3 and 5 cm. The simulations show also the development of thin ice <3 cm, which is typically formed during the onset of ice. Without modeling the process of thin ice break-up by surface waves, the model is likely to simulate an earlier onset of very thin ice cover (Oveisy et al., 2014a). Additionally, the lack of advective ice dynamics in the ice-formation model limits the description of the deformed ice, that can develop along the shores of LLC. Nevertheless, these consequences will be less pronounced in lakes with limited fetch (e.g. in small lakes) and consequently smaller surface waves and thus will lead to better model representation of ice cover and duration in small compared to large lakes.

Application of 3-D hydrodynamic models to simulate multi-year changes in ice cover are rare (e.g. Fujisaki et al., 2013). Previous studies applying the model AEM3D to ice covered lakes have considered only single winters (Oveisy et al., 2012; Oveisy et al., 2014a), but did not include continuous multi-year simulations.

Applications of 3D hydrodynamic models to ice cover development and ice cover distribution have focused mainly on large lakes, e.g. Lake Ontario (Oveisy et al., 2012) or Lake Erie (Fujisaki et al., 2013; Oveisy et al., 2014a). The only application of a coupled 3D hydrodynamic - ice model to a small lake was conducted on Lake Harmon (Oveisy et al., 2012). However, the latter study focused on the increase and decline in ice thickness above 10 cm but did not consider the development and melt away of ice nor ice cover with a thickness below 10 cm. In general, previous 3D studies have typically not investigated ice formation in lakes where ice thickness remains below 10 cm during the entire winter season, as it is common in LLC and many other medium-sized to small, temperate lakes. In the study on Lake Erie by Fujisaki et al. (2013) observed ice cover was up to 50 cm thick and most of the observations available referred to ice thickness >10 cm. In the cases when ice thickness was <10 cm the agreement between

model and observations was rather low: the model simulated up to 30 cm of ice, even where there was no ice cover (Fujisaki et al., 2013).

The study here applying the coupled 3D hydrodynamic-ice model AEM3D to LLC simulating ice cover development and ice cover distribution continuously over several years in a sub-divided lake that partially freezes and typically develops thin ice cover with thickness below 10 cm extends the range of 3D model applications to ice cover simulation in lakes. The model results demonstrate that comparatively thin ice with thickness below 10 cm can be simulated reasonably well and that differences in ice cover between adjacent basins in a lake with complex morphometry can also be captured well by the model. The results also show that inter-annual variability of partial and spatially heterogeneous ice cover in LLC is captured well by the model.

2.5 Conclusion

The 3D hydrodynamic model AEM3D coupled with an ice module allows seasonally resolved as well as multi-year simulations of water temperature and ice cover and in temperate lakes. The application of the model to LLC, a lake consisting of three distinct but connected basins with hydrodynamically different conditions showed a good agreement between the simulated and observed inter-annual variation in the spatial distribution of ice cover, ice thickness and duration of ice cover. The ice formation and extent differed gradually between the three sub-basins. In temperate lakes, inter-annually variable and partial ice formation is a common feature, and the adequate simulation of such conditions requires reliable reproduction of thin ice with thickness below 10 cm.

The results suggest that the 3D hydrodynamic model AEM3D with its ice module is a powerful tool cover in lakes or reservoirs with partially and inter-annually variable ice. It can be useful to reconstruct the history of ice in lakes lacking spatiotemporal ice records or to forecast ice formation, distribution and thickness under future scenarios, e.g. climate change. In this respect, the application of 3D models can help to understand the impact of climate warming on partially and intermittent ice covered lakes regarding hydrodynamic conditions and water quality, e.g. phytoplankton growth and oxygen.

Acknowledgments

We thank Chris Dallimore and Chris O'Neil from Hydronumerics for their help and support with the model setting. We are grateful to Orlane Anneville (French National Institute for Agricultural Research) who provided expertise that greatly assisted the research. We acknowledge the Water Police for the ice data, MeteoSchweiz for the COSMO wind data and the German Weather Service (DWD) for the meteorological data. The field data (CTD profiles, inflows, outflows, water level) was provided by the Landesanstalt fuer Umwelt Baden-Wuerttemberg (LUBW), the BOWIS- Water information system of Lake Constance from the International Commission for water protection of Lake Constance (IGKB), the Hydrographic Service Vorarlberg (VA), and the Swiss Federal Office for the Environment (BAFU). We also would like to thank Leon Walther that helped with the translation of the ice reports of the Water Police.
This study was financially supported by the German Research Foundation (DFG) within the framework of the RTG R3 (Research Training Group – Responses to biotic and abiotic changes, Resilience and Reversibility of lake ecosystems), grant number 298726046/GRK2272/A4.

Supplements

2A. Ice data

Table 2.3: Ice data for Lower Lake Constance collected by various sources.

2010		
5 January	https://www.bild.de/regional/stuttgart/polizei-warnt-bodenseeeis-traegt-noch-nicht-11003144.bild.html	Ice around Reichnau (GS) and from Mettnau to Radolfzell (ZS)
7 January	https://www.tagblatt.ch/ostschweiz/mit-schlittschuhen-auf-gnadensee-ld.176908 Tagblatt	Presence of ice skaters in the area Reichnau – Hegne (GS) Also in Radolfzell and Markelfingen (ZS and GS)
9 January	https://www.tagblatt.ch/ostschweiz/platzwarte-auf-dem-gnadensee-ld.376254 Tagblatt	Presence of ice skaters in the area Reichnau – Hegne (GS)
12 January	CTD profiles	Basin of GS and ZS not completely covered because LUBW collected CTD profiles
2 February	CTD profiles	Basin of GS and ZS not completely covered because LUBW collected CTD profiles
13 February	Wasser Polizei	Ice starts to form in GS and Markelfinger Winkel (limited bearing capacity nearshore and in shallow-water zones)
2 March	CTD profiles	Basin of GS and ZS not completely covered because LUBW collected CTD profiles
7 April	CTD profiles	Basin of GS and ZS not completely covered because LUBW collected CTD profiles
2011		
24 January	CTD profiles	Basin of GS completely closed: Point M_{GS} was not reachable by boat and it was not possible for the LUBW to collect CTD profiles

		ZS not completely covered because LUBW collected CTD profiles in M_{ZS}
8 February	CTD profiles	Basin of GS completely closed: Point M_{GS} was not reachable by boat and it was not possible for the LUBW to collect CTD profiles ZS not completely covered because LUBW collected CTD profiles in M_{ZS}
28 Febraury	CTD profiles	Basin of GS and ZS not completely covered because LUBW collected CTD profiles
2012		
18 January	Wasser Polizei	Ice around the coast of GS
20 January	CTD profiles	Basin of GS and ZS not completely covered because LUBW collected CTD profiles
4 February		Almost no ice in Radolfzell (ZS)
		Ice in Markelfinger Winkel (GS)
		Ice in Markelfinger Winkel (GS)

	 http://www.hikr.org/tour/post46071.html	
5 February		Ice in Markelfinger Winkel (GS)
		Ice in Markelfinger Winkel (GS)
	 http://www.hikr.org/tour/post46102.html	Ice in Markelfinger Winkel (GS)
6 February	Wasser Polizei	Abundant ice in GS Markelfinger Winkel completely closed (GS)

		Ice on the shore of ZS and RS
9 February	Wasser Polizei	Abundant ice in GS Markelfinger Winkel completely closed (GS) Ice on the shore of ZS and RS
10 February	  http://www.hikr.org/tour/post46318.html	Ice cover in the area Mettnau (ZS/GS) Ice cover in Markelfinger Winkel (GS)
11 Febraury	Wasser Polizei	Almost closed ice cover in GS Abundant ice in ZS
12 Febraury	Wasser Polizei	Almost closed ice cover in GS
13 February	https://www.nikon-fotografie.de/vbulletin/bilderforum/187181-der-untersee-ist-zugefroren.html	It was possible to skate from Stein am Rhein almost to KN: not bearing ice cover along the shores of RS
20 Febraury	Wasser Polizei	Almost closed ice cover in GS
21 February	CTD profiles	Basin of GS completely closed: Point M_{GS} was not reachable by boat and it was not possible for the LUBW to collect CTD profiles ZS not completely covered because LUBW collected CTD profiles in M_{ZS}

6 March	CTD profiles	Basin of GS completely closed: Point M_{GS} was not reachable by boat and it was not possible for the LUBW to collect CTD profiles ZS not completely covered because LUBW collected CTD profiles in M_{ZS}
3 April	CTD profiles	Basin of GS and ZS not completely covered because LUBW collected CTD profiles
2013		
8 January	CTD profiles	Basin of GS and ZS not completely covered because LUBW collected CTD profiles
12 February	CTD profiles	Basin of GS and ZS not completely covered because LUBW collected CTD profiles
8 April	CTD profiles	Basin of GS and ZS not completely covered because LUBW collected CTD profiles
2014		
14 January	CTD profiles	Basin of GS and ZS not completely covered because LUBW collected CTD profiles
4 February	CTD profiles	Basin of GS and ZS not completely covered because LUBW collected CTD profiles
4 April	CTD profiles	Basin of GS and ZS not completely covered because LUBW collected CTD profiles
2015		
3 January	Instagram	No ice in Markelfinger Winkel (GS)
12 January	CTD profiles	Basin of GS and ZS not completely covered because LUBW collected CTD profiles
21 January	https://bodenseewellen.blogspot.com/2015/01/	"It doesn't look as LC or part would freeze over the winter- As in the last and penultimate winter"
3 February	CTD profiles	Basin of GS and ZS not completely covered because LUBW collected CTD profiles
2 March	Instagram	No ice around Mettnau (ZS/GS)
3 March	CTD profiles	Basin of GS and ZS not completely covered because LUBW collected CTD profiles
2016		

19 January	Instagram	No ice in Steckborn (RS)
22 January	 https://bodenseewellen.blogspot.com/2015/01/	A ice skater in Hegne (GS)
23 January	 https://bodenseewellen.blogspot.com/2015/01/	Ice in the area Hegne – Reichnau (GS)
25 January	Instagram	GS partially cover
2017		
3 January	Instagram	No ice in ZS
6 January	Instagram	Ice skaters in Hegne (GS)
8 January	Instagram  https://bodenseewellen.blogspot.com/2015/01/	Ice in front of Reichnau (GS) Ice in the area of Hegne – Allensbach (GS)

	 https://bodenseewellen.blogspot.com/2015/01/	Ice and ice skaters between Reichnau – Allensbach (GS)
10 January	 https://bodenseewellen.blogspot.com/2015/01/  https://bodenseewellen.blogspot.com/2015/01/ 	Ice in Hegne (GS) Ice on the northern shore of of Reichnau (GS) Ice around Reichnau (GS)

	https://bodenseewellen.blogspot.com/2015/01/	
12 January	Südkurier Online https://www.suedkurier.de/region/kreis-konstanz/reichenau/Schlittschuhlaufen-und-Sicherheit-Wie-Eislaeufer-sicher-auf-dem-Gnadensee-unterwegs-sind;art372456,9083412	Ice between Reichnau and Hegne (GS)
17 January	Instagram	Ice in ZS
19 January	Instagram	Ice in Allensbach (GS)
20 January	Instagram Wasser Polizei	Ice skaters in the area of Hegne – Reichnau (GS) Ice around the coast of LC: width of 40 m around the north shore of Reichnau; Hegne 100 m width; 10 - 50 m width around Markelfinger Winkel (GS)
21 January	Instagram Wasser Polizei	Ice in the harbor of Reichnau (GS) Ice around the coast of LC: width of 60 m around the north shore of Reichnau; Hegne 100 m width; Allensbach 30 m; 30 - 80 m width around Markelfinger Winkel (GS)
22 January	Instagram Instagram Instagram	Ice skaters in Hegne (GS) GS completly covered Ice in Berlingen (RS) Ice arounf the Liebinsel (ZS)
23 January	Wasser Polizei	Around the coast of LC: Width of 100 m around the north shore of Reichnau; Hegne 200 m width; Allensbach 150 m; 40 - 150 m width around Markelfinger Winkel (GS); Ermantiger up to 100 m; from Horn to Ohningen up to 30 m width (RS); Mettnau up to 100m; Hori up to 50 m (ZS).
24 January	Wasser Polizei	Extensive ice cover in GS: Width of 300 m around the north shore of Reichnau; Hegne 300 m width; Allensbach 300 m; 50 - 150 m width around Markelfinger Winkel

		Ice around the coast of ZS: Mettnau up to 150m; north Hori up to 50 m Ice around the coast of RS: Ermantiger up to 150 m; from Horn to Ohningen up to 30 m width
	 GS	
	 GS: picture from a drone	
	https://www.wetteronline.de/fotostrecken/2017-01-25-ei?galleryIndex=1&part=single	
26 January	Instagram Instagram Wasser Polizei	Ice in front of the Schloss Gaienhofen (RS) Ice skaters in the area of Hegne (GS) Extensive ice cover in GS: Harbor of Reichnau; ice width of 300 m around the north shore of Reichnau; Hegne 300 m width; Allensbach 300 m; 50 - 150 m width around Markelfinger Winkel. Ice around the coast of ZS: Mettnau up to 150m; northern shore of Hori ice width up to 50 m. Ice around the coast of RH: Ermantiger up to 150 m; from Horn to Ohningen up to 30 m width.
27 January	Instagram Instagram Wasser Polizei	Complete ice cover between Reichnau and Allensbach (GS)

		Extensive ice cover in GS: harbor of Reichnau; width of 300 m around the north shore of Reichnau; Hegne 300 m width; Allensbach 300 m; 50 - 100 m width around Markelfinger Winkel. Ice around the coast of ZS: Mettnau up to 100m; northern shore of Hori ice width up to 80 m. Ice around the coast of RH: Ermantiger up to 100 m; from Horn to Ohningen up to 30 m width.
28 January	Instagram Instagram   	Ice skaters in the area of Hegne - Reichnau (GS) Ice in Markelfinger Winkel Ice around Mettnau (ZS) Ice around Mettnau (ZS) Ice around the Liebinsel (ZS)

	 http://www.hikr.org/tour/post117092.html	Ice closed to Radolfzell (ZS)
29 January	Instagram Instagram Instagram Instagram Instagram Instagram Wasser Polizei https://www.youtube.com/watch?v=DfEf6hvJOmE	Ice skater in the area Radolfzell – Mettnau (RZ) Ice in Markelfinger Winkel (GS) Ice skaters in the area of Hegne (GS) Ice in the harbor of Reichnau (GS) Full ice cover between Reichnau and Allensbach (GS) Ice in Allensbach (GS) Extensive ice cover in GS: harbor of Reichnau; width of 300 - 400 m around the north shore of Reichnau; Hegne 400 m width; Allensbach 300 m; 50 - 100 m width around Markelfinger Winkel. Ice around the coast of ZS: Mettnau up to 150m; northern shore of Hori ice width up to 80 m. Ice around the coast of RH: Ermantiger up to 200 m; from Horn to Ohningen up to 30 m width. Complete ice cover in GS
30 January	Instagram Instagram	Ice skaters in the area of Hegne - Reichnau (GS) Full ice cover and ice skaters between Reichnau and Allensbach (GS) Complete cover in Markelfinger (GS)
31 January	Instagram	Complete cover in GS (until the northern extreme of Reichnau)
1 Febraury	Instagram	Ice skaters in GS
2 February	Instagram (Schwarzwalddrohne) https://www.youtube.com/watch?v=JxkbyRSSEBY	Complete cover in GS and ice skaters Complete cover in GS and ice skaters

3 February	Instagram	Ice cover in Allensbach (GS)
4 February	Instagram	Ice skaters in the area of Hegne (GS)
	Instagram	Ice cover in Allensbach (GS)
7 Febraury	Instagram	Ice cover in Allensbach (GS)
16 Febraury	Instagram	Ice skaters in the area of between Reichnau and Allensbach (GS)
17 Febraury	Instagram	Ice cover in the harbor of Reichnau (GS)
	Instagram	Ice around Mettnau (ZS)
27 February	Instagram	Ice cover in Allensbach (GS)
7 March	Instagram	No ice Mettnau (ZS)
2018		
18 February	Instagram	No ice in ZS
22 February	Instagram	No ice in Markelfinger Winkel (GS)
25 Febraury	Instagram	Ice in Hegne (GS)
27 Febraury	Instagram	Ice in the harbor of Reichnau (GS)
28 Febraury	Instagram	Ice in Allesbach (GS)
	Instagram	Ice in the harbor of Gaienhofen (ZS)
1 March	Instagram	Ice in Hegne (GS)
	Instagram	No ice in Berlingen (RS)
2 March	Instagram	Ice in Allensbach harbor (GS)
	Instagram	Ice along the shore of Allensbach (GS)
	Instagram	No ice in Berlingen (RS)
	Instagram	Ice in Markelfinger Winkel (GS)
	Instagram	Frozen lake near Mettnau (ZS/GS)
3 March	Instagram	Ice in Allesbach (GS)
4 March	Instagram	Ice near Mettnau (ZS/GS)
5 March	Instagram	Ice near Mettnau(ZS/GS)
6 March	Instagram	Ice in Markelfingen (GS)
16 March	Instagram	No ice in Steckborn (RS)
18 March	Instagram	No ice cover around Mettnau (ZS/GS)
25 March	Instagram	No ice in ZS
28 March	Instagram	No ice in Markelfinger Winkel (GS)

2B. Application of AEM3D to Lake Constance

The hydrodynamic model of LC had a computational grid of 300 m x 300 m and 81 vertical grid cells with a thickness of 1 to 15 m. The major inflows of LC, according to Stewart (1988), were considered and the water level was kept constant to the mean water level during the simulated period (396 m a. s. l.), by adjusting the outflow discharge with a water balance.
Water temperature in LC was initialized by means of data from a thermistor chain (RBR-solo, vertical resolution 0.5 to 2 m in the upper 20 m and coarser below) at the station EU and data with a coarser resolution (from 5 to 20 m) from the Landesanstalt fuer Umwelt Baden-Wuerttemberg (LUBW) at station FU. Spatially resolved wind fields were linearly interpolated to the computational grid of LC. Except for the wind field, the model was driven with horizontally uniform meteorological data.

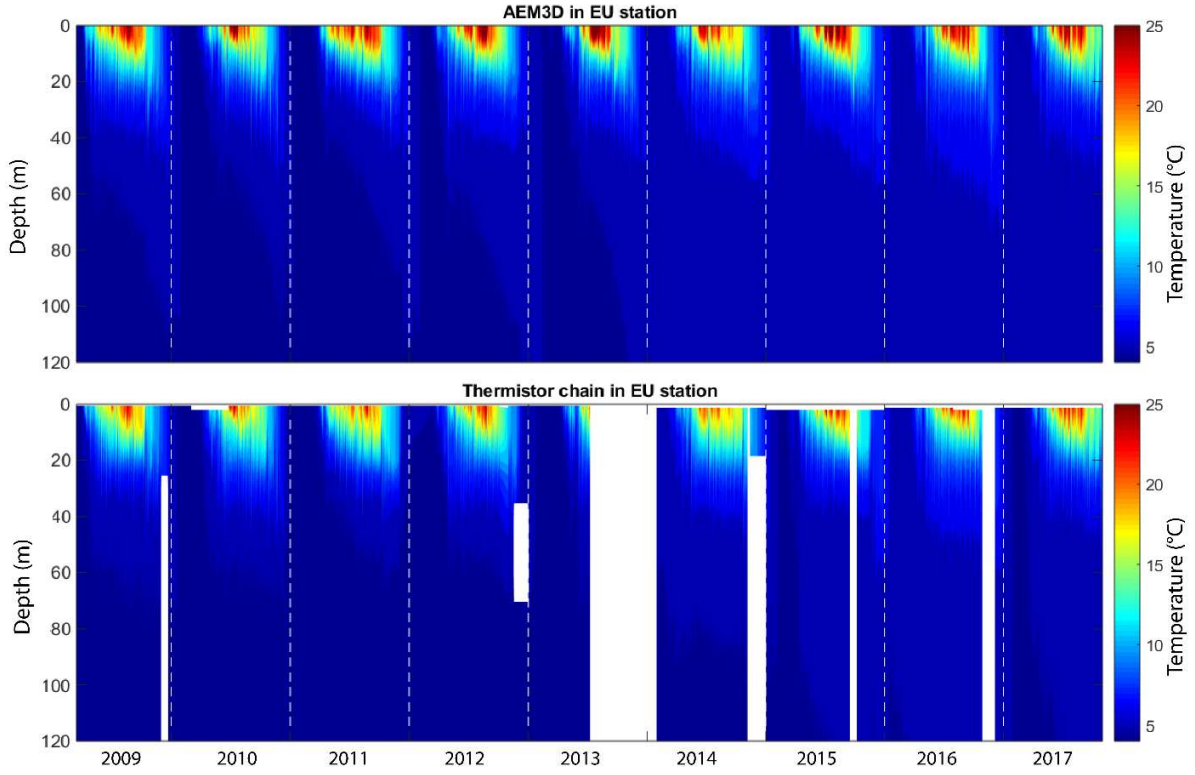

Figure 2.8: Observed and simulated thermal structure in the simulated period in the station EU.

2C. Model parameters

The major model parameters for the simulations of LLC and LC are listed in Table SB1, while Table SB2 shows the ice module parametrization of AEM3D. Most of the parameters were set to their default values, except for the photosynthetically active radiation (PAR) extinction coefficient and the horizontal diffusivity (Tab. SB1). According to the study of Tilzer (1983) the background value of the PAR extinction coefficient in Lake Constance is 0.27 m^{-1} in the absence of phytoplankton and the extinction coefficient increases linearly with the chlorophyll *a* concentration at a rate of 0.015 mg Chla m^{-3} m^{-1}. As our focus is on winter conditions when algal concentration are low, we used 0.3 m^{-1} for the PAR extinction coefficient. A horizontal diffusion coefficient of 1 m^2 s^{-1} was employed in the model for Lake Constance. In the model of LLC we used a smaller horizontal diffusion coefficient, i.e., 0.5 m^2 s^{-1}, because the horizontal diffusivity increases with the length scale of the horizontal dimension considered (Okubo, 1971; Peeters & Hofmann, 2015) and the grid size in LLC was three time smaller than in the simulation of the entire lake.

Table 2.4: Model parameters used in AEM3D. LC is Lake Constance and LLC is Lower Lake Constance.

Parameters	**LC**	**LLC**	**Setting**
Mean albedo (-)	0.8	0.8	Default
Wind drag coefficient (-)	0.0013	0.0013	Default
Bottom drag coefficient (-)	0.005	0.005	Default
PAR extinction coefficient (m^{-1})	0.3	0.3	Calibrated
Near infrared extinction coefficient (m^{-1})	1.0	1.0	Default
UVA extinction coefficient (m^{-1})	1.0	1.0	Default
UVB extinction coefficient (m^{-1})	2.5	2.5	Default
Horizontal diffusivity (m^2 s^{-1})	1	0.5	Calibrated
Surface heat transfer coefficient (W m^{-2} $°C^{-1}$)	0.0013	0.0013	Default
Time step (min)	5	2	

Table 2.5: Parametrization of the ice module in AEM3D.

Parameters	LLC	
Ice depth initialization (m)	0.001	
Density of blue ice (kg m^{-3})	917	Rogers et al. 1995
Density of white ice (kg m^{-3})	890	
Blue ice conductivity (W m^{-1} $°C^{-1}$)	2.3	Rogers et al. 1995
White ice conductivity (W m^{-1} $°C^{-1}$)	2.0	Rogers et al. 1995
Attenuation coefficient of solar radiation through snow (m^{-1})	6	
Attenuation coefficient of solar radiation through blue ice (m^{-1})	3.75	
Attenuation coefficient of solar radiation through white ice (m^{-1})	1.5	
Max snow density (kg m^{-3})	400	
Min snow density (kg m^{-3})	50	
Latent heat of fusion of water (J kg^{-1})	$3.34 \cdot 10^5$	Rogers et al. 1995

2D. Sub-basins delimitation in Lower Lake Constance

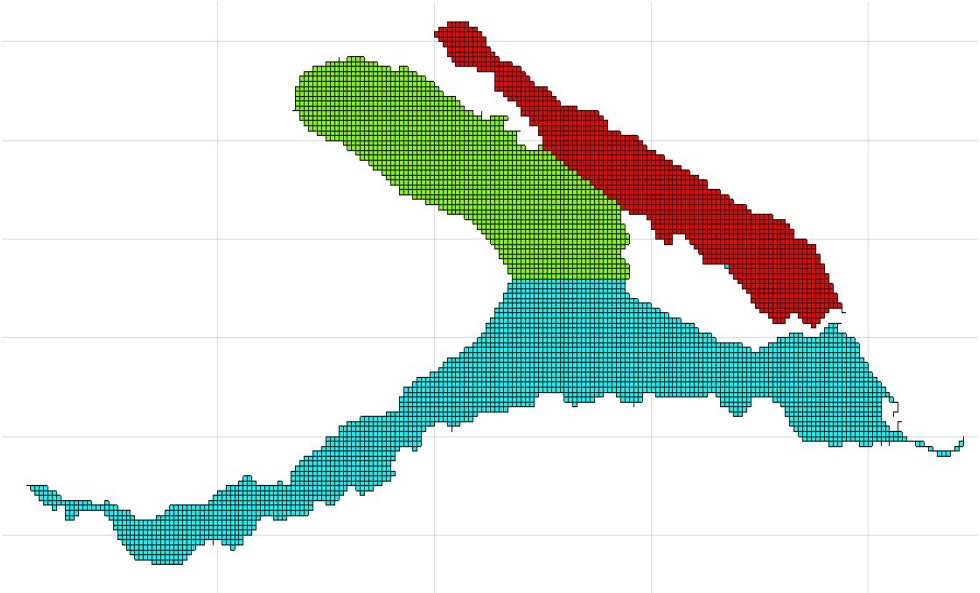

Figure 2.9: Delimitation of the sub-basins, based on the morphological shape of the lake.

2E. Winter inverse stratification in Lower Lake Constance

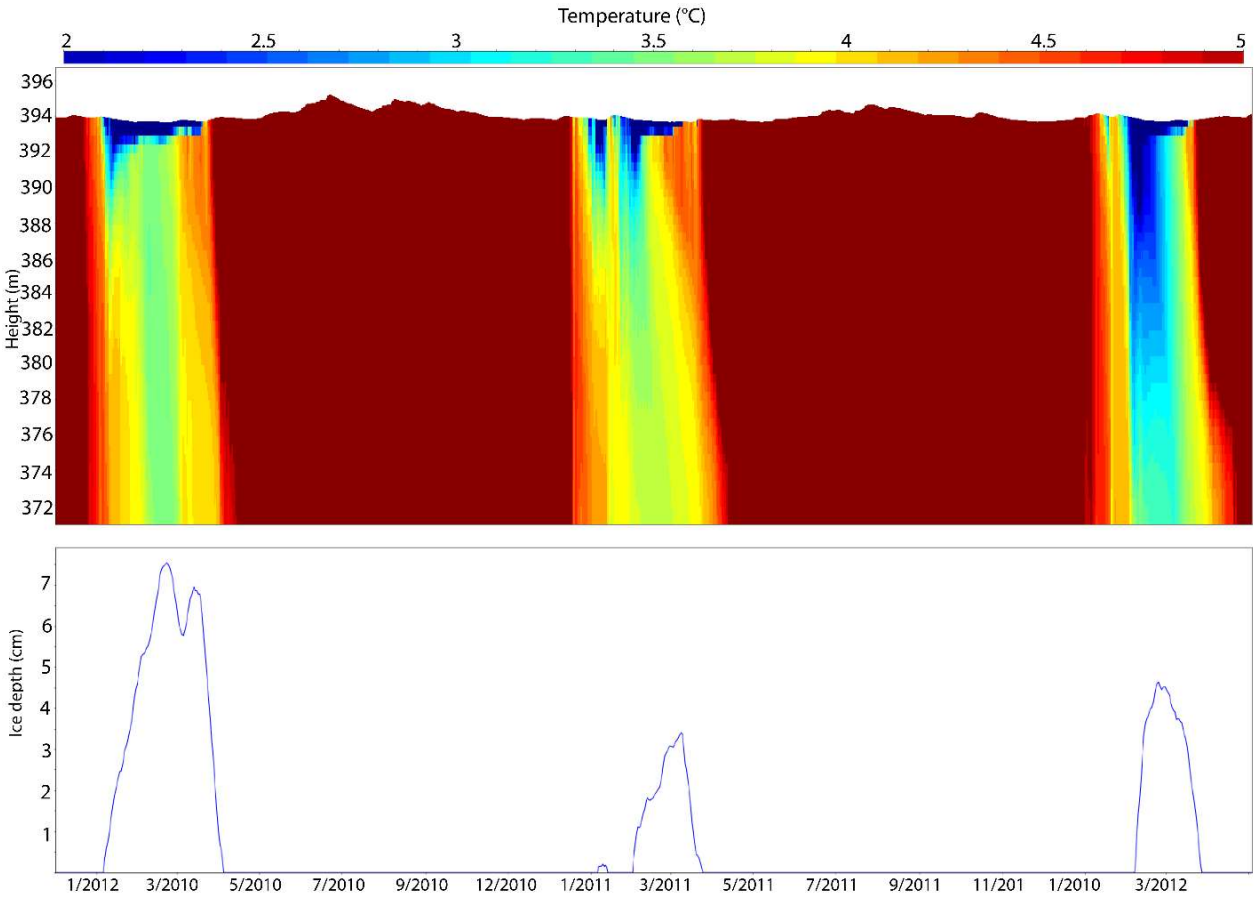

Figure 2.10: Inverse stratification in winter months in M_{ZS}.

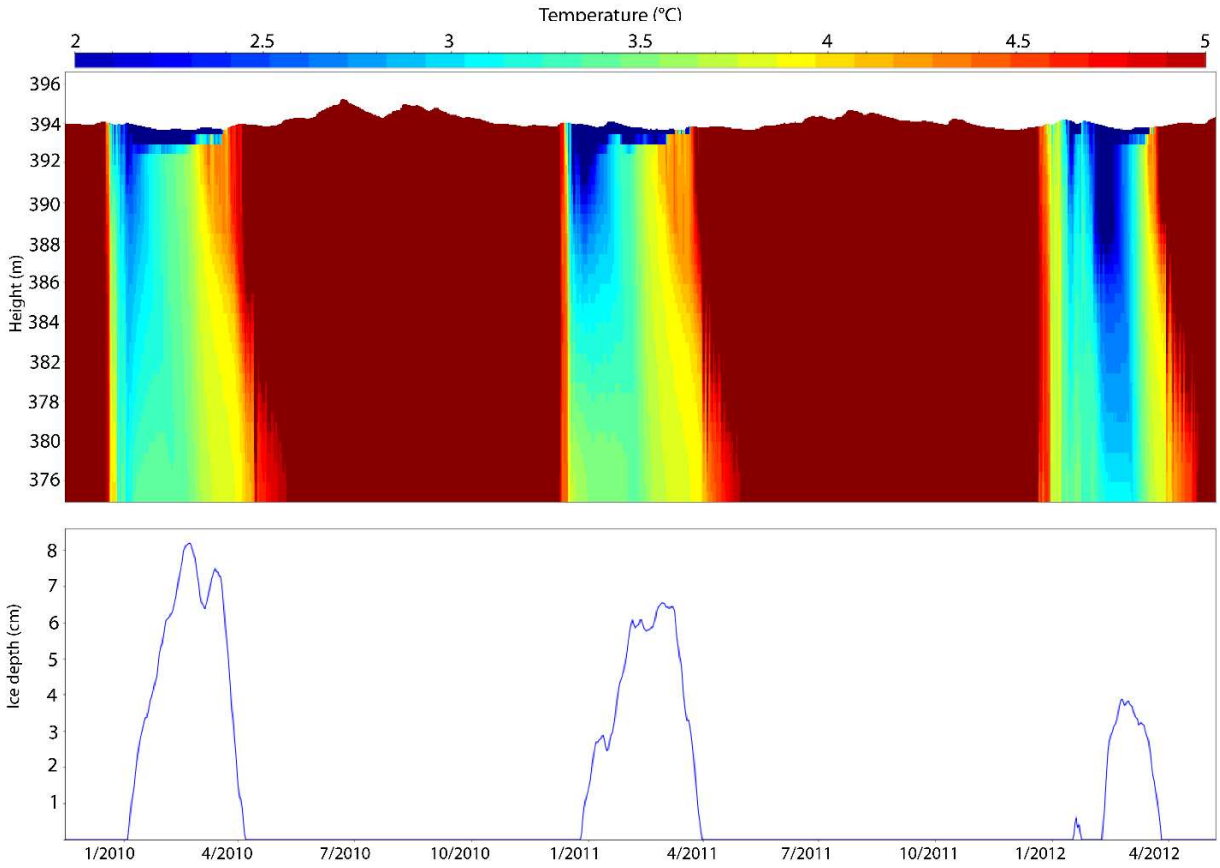

Figure 2.11: Inverse stratification in winter months in M_{GS}.

3

Effects of climate change on inter-basin exchange in Lower Lake Constance

I. Caramatti, H. Hofmann, & F. Peeters

(in prep.)

Abstract

Inter-basin exchange of water and dissolved substances in lakes is often limited by topographic constrictions leading to spatially heterogeneous distributions of nutrients and plankton. Here, we identify the main factors controlling inter-basin exchange on seasonal and inter-annual time scales and investigate the impact of changes in climate and hydrology focusing mainly on the exchange between two basins of Lower Lake Constance (LLC). The analysis is based on multi-annual simulations of LLC, a sensitivity analysis, and numerical tracer experiments with a coupled 3-D hydrodynamic ice model (AEM3D). The seasonal course of water exchange is predominantly determined by the seasonal change in the current speed across the sill, v_S, but also by changes in the area of the cross-section above the sill resulting from water level changes. The seasonal pattern of v_S is linked to the presence of ice cover, the seasonal change in stratification and in water level. The impact of climate warming and hydrological change on water exchange therefore varies seasonally. Climate warming results in reduced ice cover and an earlier onset and longer duration of stratification, leading to enhanced inter-basin exchange especially during winter and spring, but not in summer. In contrast, increased water levels enhance inter-basin exchange especially in summer, because the increase in cross-sectional area associated with increased water levels coincides then with high v_S. Finally, the

fraction of water from Upper Lake Constance reaching the rather secluded basin Gnadensee increases with climate warming, implying a larger influence of the upstream conditions on Gnadensee.

3.1 Introduction

Hydrodynamic processes affect bio-geochemistry, water exchange and the distribution of dissolved substances and suspended particles in lakes (Rueda & Cowen, 2005). Topographic constrictions, such as a shallow sill separating semi-enclosed basins from the main basin of a lake, can substantially limit inter-basin exchange and thus cause spatially heterogeneous distributions of nutrients, other water constituents, and plankton. Identification of the main factors controlling the exchange between semi-enclosed basins and the main water body is important for the assessment of potential consequences of climate change and associated changes in hydrology for inter-basin exchange and for the resulting distributions of dissolved substances and organisms.

Transport in lakes is predominantly controlled by wind forcing, ice cover suppressing wind forcing at the lake surface, stratification, river inflow, and water level determining the effective cross sections for inter-basin exchange across sills. All these factors are affected by climate change and hydrologic alterations in the catchments of lakes. E.g. climate warming reduces ice cover formation and duration (Magnuson et al., 2000), causes earlier ice breakup and thus longer periods of water column stratification, and results in warmer surface water temperature, increased stratification, and heat storage during summer (Livingstone 2003; Mishra et al., 2011; O'Reilly et al., 2015). Reduced or absent ice cover leads to more energetic winter circulation driven by wind shear on the open water (Fujisaki et al., 2013), whereas stronger stratification during summer may restrict the transfer of wind forcing input to horizontal currents in a narrower surface layer and may thus result in larger wind-driven surface currents (Bennett, 1974). Climate change and/or modifications of the hydrology in the catchment of lakes may modify the water level dynamics in lakes (Haghighi & Kløve, 2015) thus also affect inter-basin exchange across sills.

Exchange of water and dissolved substances has been studied in lakes using different approaches ranging from tracer measurements to numerical models. E.g., field data on tracers and inverse modelling of tracer concentrations combining a simple inter-basin exchange model with vertical transport have been employed to investigate deep water renewal in Lake Baikal (Weiss, Carmack, & Koropalov, 1991; Hohmann et al., 1998; Peeters, 2000). Similar tracer studies and exchange models have been used to demonstrate that horizontal exchange between sill-separated lake basins during winter can be a dominant process controlling deep water renewal and deep water oxygenation in lakes (Aeschbach-Hertig et al., 1996; Schlatter et al., 1997). In these studies, as well as in MacIntyre et al. (2002), inter-basin exchange is mainly driven by inter-basin density differences. Other mechanisms affecting inter-basin exchange were discussed by Bartish (1987), e.g. riverine inflow, pressure-gradient-driven subsurface flows as cumulative result of wind-driven surface flows, flushing due to oscillating seiche motions, and turbulent horizontal diffusion.

During the last decades, three-dimensional (3-D) hydrodynamic models have been increasingly used to investigate hydrodynamics in lakes (e.g. Hodges et al., 2000; Beletsky & Schwab, 2001; Appt et al., 2004; Razmi et al., 2014; Wahl & Peeters, 2014; Dissanayake et al., 2019), but numerical simulations focusing on the exchange between sub-basins in lakes are not very common. One of the first applications of a 3-D hydrodynamic model to study the inter-basin exchange in standing freshwaters was focused on the exchange between a freshwater embayment and Lake Ontario through a long, shallow channel (Rueda & Cowen, 2005). Rao et al. (2009) simulated the circulation and the temperature and pollutant distribution in Hamilton Bay in Lake Ontario, and the exchange between a harbor and the lake. In Lake Huron, a 3-D hydrodynamic model was combined with field measurements and drifter experiments to examine exchange between the open lake and the Saginaw Bay during summer months of three consecutive years (Nguyen et al., 2014). The exchange in the same system was also studied during the winter season by employing the same model coupled with an ice model (Nguyen et al., 2017). This study demonstrated that the ice cover significantly dampens water movement producing almost stagnant conditions around February in the Saginaw Bay (Nguyen et al., 2017). This result agreed with the study of Fujisaki et al. (2013) showing that ice cover slowed down surface water velocities in Lake Erie.

Three-dimensional hydrodynamic models have also been employed to assess the implication of modified boundary conditions on hydrodynamics and inter-basin exchange. Niu et al. (2015) investigated the sensitivity of inter-basin exchange in the three basins of Lake Erie to modification of the thermal regime. The effect of modifications of the wind field on inter-basin exchange has also been investigated, e.g., in Lake Taihu (China) (Liu et al., 2018), in Lake Geneva (Switzerland) (Umlauf & Lemmin, 2005), and in Lake Argyle (Western Australia) (Woodward et al., 2017).

However, most of these studies were conducted in very large lakes and focused on short, selected time periods. In the study here, we employed a 3-D model to investigate the exchange between sill-separated basins in detail resolving seasonal time scales in multi-annual simulations. With this approach, we asses to which extent climate warming and water level changes affect inter-basin exchange at seasonal time scales. The 3-D Aquatic Ecosystem Model (AEM3D) was used to simulate hydrodynamic conditions in Upper (ULC) and Lower Lake Constance (LLC), investigating in detail the water exchange between the basins of LLC in nine consecutive years. The main focus was on the water exchange between Gnadensee (GS) and the adjacent basin Zeller See (ZS), which are separated by a shallow sill. The model was employed to study the main drivers of water exchange and its modifications due to climate warming and hydrological changes. Additionally, we conducted numerical tracer experiments providing information on the spreading of the water from the main tributary to LLC, river Seerhein, which originates from ULC and enters into the basin Rheinsee, from where its water spreads via ZS into GS. We hypothesized that climate warming and water level changes alter the water exchange between GS and ZS and the contribution of water from Seerhein in GS not only in absolute terms but also the seasonal patterns of the exchange.

In the following, we first explain the lake system, provide details on the model and the numerical simulations, and describe the scenarios considered. Afterwards we present and discuss the results from our numerical investigations.

3.2 Methods

3.2.1 Study site

Lake Constance (LC, Germany) is a large pre-alpine lake of glacial origin (Fig. 3.1). The lake consists of two main parts, Upper Lake Constance (ULC) and downstream Lower Lake Constance (LLC), which is connected to ULC via river Seerhein (Fig. 3.1c). ULC has a surface area of 473 km^2 and a maximum depth of about 251 m, whereas LLC has a surface area of 63 km^2 and maximum and mean depth of 46 m and 25 m, respectively.

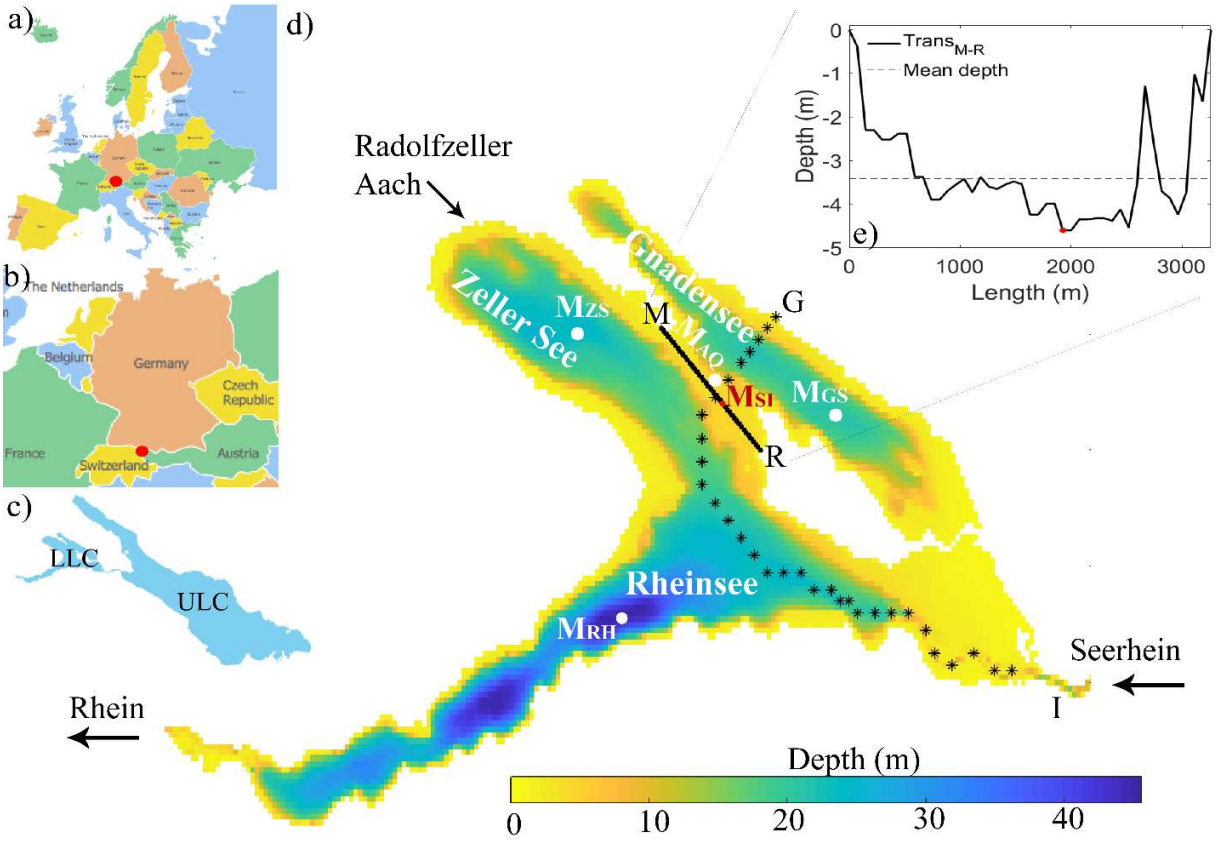

Figure 3.1: Bathymetry of the study site. a) and b) Location of Lake Constance in Europe. c) Bathymetry of Lake Constance and location of the meteorological station (DWD KN) and the stations used to initialize the model applied to LC. b) Bathymetry of Lower Lake Constance, distinguishing between the sub-basins and showing the main inflows and the

outflow. Monitoring stations, used to initialize the model applied to LLC, were shown: M_{GS} is in the basin of Gnadensee, M_{ZS} in Zeller See and M_{RS} in Rheinsee.

LLC is subdivided into three sub-basins (Fig. 3.1d) that differ in maximum water depth, hydro-geological features, thermal structure, ice formation and coverage (Caramatti et al., 2020), phytoplankton community and nutrient distributions (IGKB 2018). Rheinsee (RS) is the most southern basin with a maximum water depth of 46 m. In the north, RS is connected to Zeller See (ZS), which has a maximum water depth of 24 m. The most northern sub-basin of LLC is Gnadensee (GS) with a maximum water depth of 20 m. GS is the most enclosed sub-basin. It has no significant inflows and is connected to ZS only via a shallow sill of about 3.3 km length. The sill extends from the peninsula of Mettnau to the island of Reichenau (Fig. 3.1d,e) and has a mean and maximum depth of 3.4 m and 4.6 m, respectively, relative to a water level of 395 m.a.s.l. River Seerhein, which is the discharge from ULC and the main inflow into LLC, enters in the most eastern part of RS. The second largest inflow to LLC is the river Radolfzeller Aach, which enters in the most western part of ZS. The outflow of LLC is located in the most western part of RS (Fig.3.1d).

A specific emphasis of this investigation is on the water exchange across the sill between GS and ZS. Model results are therefore evaluated at 42 regular spaced stations between M and R on a transect along the sill, denoted as $Trans_{M\text{-}R}$ (Fig. 3.1d,e). $Trans_{M\text{-}R}$ follows a straight line that is turned clockwise at angle 47.6° to the west-east axis. The deepest station on the sill is M_{SI}. In addition, we investigate the transport of dissolved and suspended substances from the inflow Seerhein to GS and consider 32 stations along a 12 km long transect between I and G, $Trans_{I\text{-}G}$ (Fig. 3.1d).

Lower Lake Constance is typically stratified from April to November and inversely-stratified during winter months (January-March), when LLC develops regularly partial or complete ice cover (Caramatti et al., 2020). Further, the lake can be considered as dimictic showing complete mixing during autumn overturn as well as after ice-off. During the last decade only in the years 2010, 2011, 2012 and 2017 ice cover developed in all three sub-basins of LLC, whereas full areal ice cover developed frequently in GS.

The water level of Lake Constance is unregulated and is mainly determined by the Alpine climate determining the discharge of river Rhein, the main tributary to ULC. The water level in ULC and LLC shows a pronounced seasonal course, with highest levels in summer due to inflow of melt water from the Alps and lowest levels at the end of February, when precipitation is stored as snow in the mountains of the catchment (Fig. 3.2b). The seasonal amplitude of the water level in LLC in the years 1991 – 2019 ranged between 1.0 and 2.9 m.

3.2.2 Model description

We used the 3-D Hydrodynamic-Aquatic Ecosystem Model (AEM3D, Hodges & Dallimore, 2018) to study the inter-annual and seasonal water exchange between GS and ZS in LLC under different forcing scenarios. The model was applied by coupling a coarse model for LC with a refined model for LLC. This model set up was already successfully employed to simulate the thermal structure and ice cover formation in LLC for 9 consecutive years (Caramatti et al., 2020).

The hydrodynamic model, which is based on ELCOM, solves the three-dimensional unsteady Reynolds-averaged Navier-Stokes equations, and scalar transport equations to model velocity and temperature distributions in space and time (Hodges, 2000). The equations are solved numerically using a Cartesian Arakawa C-grid in the horizontal dimension and the vertical discretization is based on fixed Z-layers (Hodges, 2000). Scalars and momentum are mixed vertically according to the amount of turbulent kinetic energy available from wind stirring and shear production compared to the potential energy due to the water column stratification (Laval et al., 2003). The model includes Earth rotation, wind stress at the surface, surface thermal forcing, inflows and outflows. The hydrodynamic model is coupled to an ice module (Hodges & Dallimore, 2018). More details can be found in Hodges (1998), Oveisy et al. (2012) and Hodges and Dallimore (2018).

3.2.3 Model set up and validation

LLC was represented by a regular horizontal computational grid of 100 x 100 m and 79 vertical layers, whose thickness varies with depth. The vertical resolution was 0.5 m in the upper 60 layers and 1 m in the lowest 15 layers. Between the 61th and the 64th layer the vertical resolution increased gradually from 0.5 to 1 m. Time series of discharge and water temperature were prescribed at the locations of the inflows Seerhein and Radolfzeller Aach. The time series of the discharge at the outflow from LLC (river Rhein) was derived from a water balance based on the measured inflows and the measured change in water level (gauge Berlingen). The time series of the water temperature of river Seerhein was derived from the simulation of LC. LC was represented by a horizontal computational grid of 300 x 300 m and 70 vertical layers (Suppl. 3A). The data for all other inflows (temperatures and discharges) were provided by the Landesanstalt fuer Umwelt Baden-Wuerttemberg (LUBW), the Federal Office for the Environment of Switzerland (BAFU) and the Hydrographic Service Vorarlberg (VA).

Water temperature in LLC was initialized using temperature profiles measured with a CTD-probe (RBR) at the stations M_{ZS}, M_{GS} and M_{RH} that were interpolated internally by the model using an inverse distance weighting method. A spatially resolved wind field was obtained by linear interpolation of the horizontally resolved COSMO wind field of MeteoSwiss (resolution of 2.2 km before April 2016 and 1.1 km afterwards, Doms et al., 2018) to the computational grid. Except for the wind field, the model was driven with horizontally uniform meteorological data (German Weather Service - DWD, station Konstanz). The model was operated by conducting continuous simulations from 4 March 2009 to 31 March 2018. For more details on model set up and input data see Caramatti et al. (2020).

The accuracy of the model to simulate the lake thermal structure and ice cover formation over the simulated period was evaluated in Caramatti et al. (2020). In the study here, we additionally compared simulated currents with currents measured with the Aquadopp Profiler HR (Nortek) at location M_{AQ} (Suppl. 3B).

3.2.4 Determination of ice cover and lake thermal structure

The model results were used to quantify the fraction of the surface area covered by ice, the depth of the surface mixed layer (SML), i.e. the mixed layer depth *MLD*, and the onset and duration of lake stratification. The fraction of ice coverage was computed as the ratio between the number of surface cells covered by ice to the number of open water surface cells. A winter in which ice covered more than 70% of the lake surface is identified as a "winter with abundant ice cover", while a winter with smaller ice coverage as a "winter with little ice cover". The *MLD* was defined as the shallowest depth at which the water density exceeds the density at the lake surface by a prescribed threshold value (Andersen et al., 2017). If the threshold is not exceeded at any depth, the surface mixed layer extends to the lake bottom and *MLD* is equal to the maximum water depth. We used a threshold value of 0.04 kg m^{-3} which is within the range of values used in other studies (Read et al., 2011; Giling et al., 2017). The *MLD* was derived from density profiles, calculated from the simulated temperature using the empirical relations of Chen-Millero (Chen & Millero, 1986). Prior to the calculation of density, the temperature profiles were linearly interpolated to a vertical resolution of 0.1 m.

The *MLD* was calculated at the deepest location in Gnadensee, i.e. at station M_{GS} (MLD_{GS}), at the deepest location in Zeller See, i.e. at station M_{ZS} (MLD_{ZS}), and at the deepest station along the sill, i.e. at M_{SI} (MLD_{SI}) (Fig. 3.1e), and along the entire $Trans_{M\text{-}R}$ (MLD_S).

The onset of stratification in GS and ZS was defined as the first time in the year at which MLD_{GS} and MLD_{ZS}, respectively, are smaller than the maximum water depth of the corresponding basin. The stratification period of the specific year ended as soon as the mixed layer depth became the maximum water depth of the basin again. Note that inverse temperature stratification can occur during winter at temperatures below 4°C resulting in shallow *MLD*. The time period of inverse temperature stratification is shown in Suppl. 3C, but was not included as part of the time period referred to as stratified period, which is here restricted to the period with a stratification characterized by decreasing water temperatures with increasing water depth.

3.2.5 Quantification of the water exchange across the sill between GS and ZS

The model results were used to compute the water exchange across the sill between GS and ZS by analyzing the water flow at 43 stations along $Trans_{M\text{-}R}$ (Fig. 3.1d). The 43 stations were spaced by a regular distance of 74 m. The components of the velocity vector simulated with the model at each of the numerical grid points were interpolated with an inverse distance-weighted method to these 43 stations on $Trans_{M\text{-}R}$. This interpolation was conducted for each depth layer separately providing depth profiles of velocities with the same vertical resolution as in the model grid. The velocities at the 43 stations were then expressed in velocity components along and across the transect $Trans_{M\text{-}R}$. The discharge of water into GS at each of these locations and at each depth layer, $d_{i,j}$, is:

$$d_{i,j} = across\_speed_{i,j} * L * h_j$$

where $i = 1,..,43$ identifies the station along the transect, $j = 1,..,N$ the depth layer, N the maximum number of vertical layers, $across\_speed$ the speed of the velocity component perpendicular to the transect positive into GS, L the distance between the stations and h_j is the vertical height of the depth layer j. The water volume entering (V_{in}) and the water volume leaving (V_{out}) GS per hour were calculated from the sum of all the positive and all negative discharges $d_{i,j}$, respectively. Note that V_{in} and V_{out} were both taken as positive numbers. We characterized water exchange as the total water volume exchanged between neighboring basins per hour, i.e. $V_{exc} = V_{in} + V_{out}$. Annual mean, minimum and maximum water exchange were computed from the time series of V_{exc}. Analogously, we calculated the water exchange above and below the mixed layer depth at $Trans_{M\text{-}R}$, $V_{exc,ML}$ and $V_{exc,B}$, respectively.

The exchange velocity across the sill, v_S, was determined by dividing V_{exc} with the area of the cross-section along $Trans_{M\text{-}R}$ above the sill, A_S, i.e. $v_S = V_{exc} / A_S$. According to this definition, the exchange velocity v_S is equivalent to the average magnitude of the velocity component across the sill along $Trans_{M\text{-}R}$, with averaging performed along the transect over the entire water column above the sill. In addition, we calculated analogously the exchange velocity within and below the *SML* at $Trans_{M\text{-}R}$, i.e. above and below the MLD_S ($v_{S,ML}$ and $v_{S,B}$, respectively).

The maximum water depth at the sill, D_S, was determined from the maximum water depth along $Trans_{M\text{-}R}$ at station M_{SI} (Fig. 3.1e). The water level at the sill is denoted as WL_S and WS is the wind speed at a location close to the sill (Fig. 3.1e, Suppl. 3D).

3.2.6 Climate warming scenario

The sensitivity of water temperature, stratification, ice cover, and water exchange to climate warming was assessed by a climate warming scenario assuming an increase in air temperatures by 4°C. This approach is the same as in earlier studies investigating the consequences of climate warming in lakes (Peeters et al., 2007a; Trolle et al., 2011; Kupisch et al., 2012; Straile et al., 2015; Wahl & Peeters 2014) and it is in the range of pessimistic projections of climate warming in the region (IPCC 2014). The climate warming scenario was applied to LLC and to LC. The latter is required to determine the water temperature of Seerhein used as inflow temperature in the corresponding climate warming simulations of LLC (Fig. 3.10). The water temperature of the other inflows, both for LLC (Radolfzeller Aach) and for ULC, were increased by 95% of the air temperature warming, in accordance to the findings of Michel et al. (2020).

The initial conditions for the warmer climate scenario were derived from a pre-run simulation of LC and LLC in which the model was driven by constructed forcing conditions: the inflow and meteorological conditions of the year 2009 with air temperatures increased by 4°C were repeated three times. The final output of a consecutive simulation of these three years was used as initial condition of the warmer climate simulations. The scenario with air temperature increased by 4°C is denoted as scenario T4 and the reference scenario as scenario T0.

3.2.7 Water level scenarios

The sensitivity of inter-basin exchange in LLC to changes in water level was investigated based on several scenarios with altered water levels. Two scenarios, referred to as “fixed-shift water-level scenarios”, assume that the water level is at all times 30 cm higher (W+), or 30 cm

lower (W-) respectively, than in the reference scenario T0. Additionally, four "seasonal water level scenarios" were considered: Scenario W_m assumes a seasonal course of water level that corresponds to the mean seasonal course of water level over the last 200 years measured at station Berlingen in LLC (Luft & van den Eertwegh, 1991). The scenario W_{m+} assumes a 30 cm higher and W_{m-} a 30 cm lower water level than W_m at all times. W_{m+} and W_{m-} are thus analogous to scenarios W+ and W- but refer to W_m as reference scenario. The scenario $W_{m,w+s-}$ assumes a 30 cm higher minimum water level in winter and a 30 cm lower maximum water level in summer than W_m. The transition between winter and summer water level is represented by a spline (Fig. 3.24). The latter scenario assumes a seasonal course of water level along the lines of the expectations for a warmer climate (Ostendorp et al., 2020). In a warmer climate less snow will be stored in the catchment of ULC during winter and snowmelt in spring will therefore provide less water than today. Hence, compared to the water levels in ULC and LLC today, water levels in a warmer climate are expected to be higher in winter and lower in summer resulting in a reduced amplitude of the seasonal water level dynamics (Ostendorp et al., 2020).

In all water level scenarios, the meteorological conditions were the same as in T0, but inflow and outflow conditions were adjusted to match the seasonal course of water level of the respective water level scenario considering the relation between water level and output discharge obtained from the water balance of the field observations.

Simulations of W+ and W- covered the entire time period from 2009 to 2018, whereas simulations of the seasonal water level scenarios W_m, W_{m+}, W_{m-}, and $W_{m,w+s-}$ focused on two years with very different ice coverage, i.e. November 2009 – December 2010 (abundant ice cover) and November 2015 – December 2016 (little ice cover).

3.2.8 Analysis of the simulation results with respect to the seasonal pattern of V_{exc} and the impact of climate warming and water level changes

The identification of seasonal patterns and the impact of climate warming and water level changes is based on monthly averages of V_{exc}, v_S, WL_S, D_S, MLD_{SI}, A_S, and WS. Potential links between the seasonal change of these parameters during the open water period were assessed

using linear regression. This analysis was performed using monthly-mean data averaged over the years 2010 to 2017 considering only the ice-free period, i.e. all month between April and December. The multi-annual averages of monthly-mean values are denoted by the subscript *m*. The impact of climate warming and water level change was assessed by determining the difference between the results obtained with the scenario considering changing conditions (scenario T4, W+ or W-) minus the results from the reference scenario T0. The focus was on a comparison of monthly-mean V_{exc}, ΔV_{exc}, and monthly-mean v_S, Δv_S, respectively, but changes in other parameters were also considered. These monthly mean differences were additionally averaged over all years providing e.g. $\Delta V_{exs,m}$ and $\Delta v_{S,m}$ and additional multi-annual means of monthly mean properties.

3.2.9 Tracer experiments

A numerical tracer experiment was conducted with AEM3D to investigate the spreading of water from river Seerhein along transect $Trans_{I\text{-}G}$ into GS. Between January 2010 and December 2017 each month a tracer was introduced continuously from river Seerhein by assigning a constant concentration of 1 mg m^{-3} to the inflowing water. At the end of each month the tracer concentration in the entire lake was set to zero to provide initial conditions (regarding the tracer concentration) for the following month or for the different scenarios of the same month. This experiment was conducted for the reference scenario T0, the climate warming scenario T4 and the water level scenarios W_+ and W-.

Monthly snapshots of the concentration distribution of the tracer along $Tans_{G\text{-}I}$ were taken 2 days after the beginning of each month to illustrate the transport of the tracer towards GS in the year 2010 (Figs. 3.26 – 3.29). Moreover, from the model output we computed the time series of tracer mass in GS ($M_{TR,GS}$) and of the tracer mass introduced in the lake (M_{TR}). Hence, the fraction of tracer mass introducted by river Seerhein reaching GS was defined as $m_{TR}=M_{TR,GS}/M_{TR}$. The time series of m_{TR} provides information on the time required of tracer to reach GS. The m_{TR} 25 days after the first introduction of the tracer in the respective month was indicated as $m_{TR,25}$.

3.3 Results

3.3.1 Temporal patterns of stratification, ice cover, currents, and water exchange

Under reference conditions (scenario T0) in all of the nine years simulated (March 2009-March 2018) stable stratification established between spring and fall in all basins of LLC. In GS stable stratification started between the 77th doy (day of the year) and the 104th doy and lasted about 7-8 months (Figs. 3.2, 3.13, Tab. 3.2). In ZS, onset of stratification occurred on average 1 day earlier and duration of stratification was on average 15 days shorter than in GS (Fig. 3.15, Tab. 3.2). In all simulated years, at least partial ice cover developed in LLC during winter (Fig. 3.2). Substantial ice cover occurred in all basins of LLC in 2010, 2011, 2012, 2015 and 2017, whereas in the other years, ice cover developed only in GS. Freezing typically occurred between January and March, but extent and duration of the ice coverage showed a pronounced inter-annual variability (Fig. 3.2). During periods with ice cover, inverse stratification developed in the uppermost 1-2 m of the water column (Figs. 3.13, 3.15). Monthly mean ice cover of more than 30% only occurred during months in winter (January to March). Between April and December all months in all years had average ice cover less than 30% of the lake surface, and this time-period of the year is therefore considered as the ice-free season.

Caramatti et al. (2020) have already shown that the model simulations of stratification and ice cover in LLC are in good agreement with observations (Suppl. 3B). Also simulated and observed current speeds at station M_{AQ} on the sill agree well with respect to the seasonal pattern, to the differences between stratified and mixed periods, and to the timing of high and low current speeds (Fig. 3.12). The comparison between measured and simulated velocity components across and along the transect $Trans_{M-R}$ indicated a RMSE of 1.0 cm s^{-1} and 0.5 cm s^{-1}, respectively, which is partially due to phase shifts in the time series and comparable with RMSE observed in other studies modelling the hydrodynamics in lakes (Nguyen et al. 2017; Dissanayake et al. 2019).

The simulated inter-basin water exchange showed a pronounced seasonal pattern characterized by higher water exchange during summer than during winter (Fig. 3.2a). The

annual maximum exchange typically occurred between June and July and ranged between 11.6×10^5 and 20.0×10^5 m^3 h^{-1}. The annual minimum exchange, ranging between 1.3×10^5 and 4.0×10^5 m^3 h^{-1}, occurred between February and March and was lowest in years with the largest ice coverage (year: 2010, 2011, 2012, 2015 and 2016 in Fig. 3.2a). Shortly before the development of ice cover, water exchange typically exhibited a secondary peak (Fig. 3.2a) which occurred at the same time as a corresponding secondary peak in water level (Fig. 3.2b). The amplitude and the details of the seasonal pattern of water exchange, and also the annual mean water exchange varied between years (Fig. 3.2a).

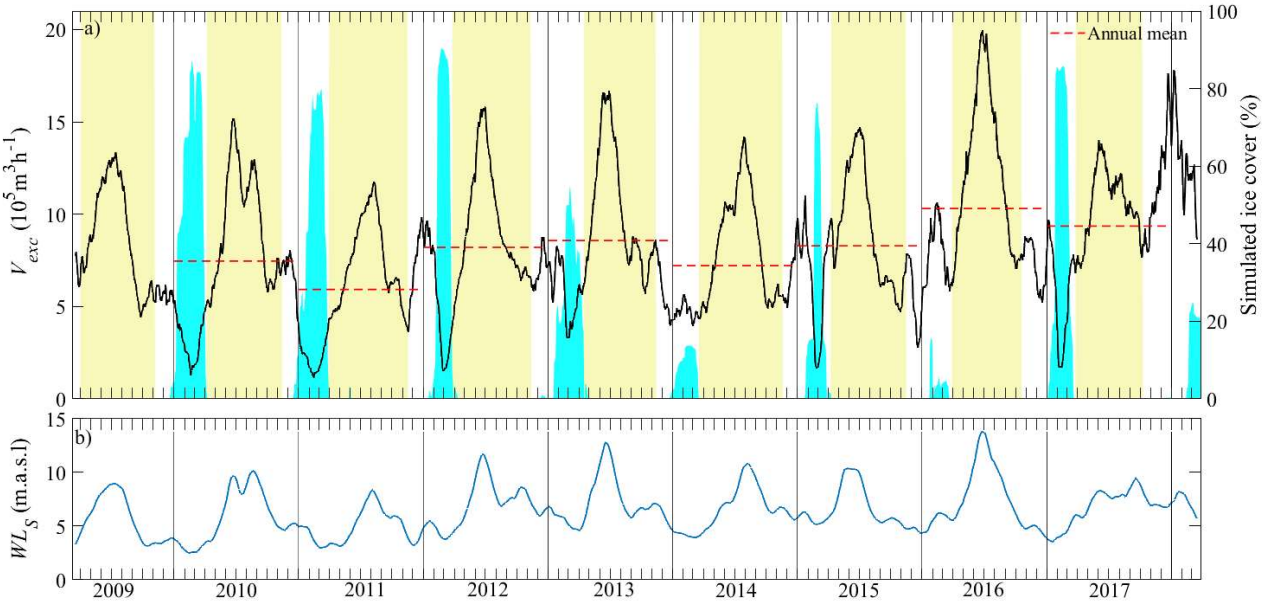

Figure 3.2: Simulated water exchange (V_{exc}) across the Trans$_{M\text{-}R}$ and water level (WL_S) between 2009 and 2018. The time series of hourly water exchange and water level were smoothed using a 30 days running mean. The annual mean water exchange is indicated by a red dashed line. The duration of the stratification period at M_{GS} is shaded in yellow, while the simulated percentage of lake surface covered by ice is shaded in cyan.

3.3.2 Relation between seasonal pattern in water exchange and other seasonally-varying parameters

The seasonal pattern of water exchange V_{exc} was compared to the seasonal change of v_S, WL_S, A_S, MLD_{SI}, and WS (Fig. 3.3). The seasonal course of V_{exc}, v_S, WL_S, and A_S was characterized by high values in summer and low values in winter. MLD_{SI}, however, was shallow in summer and progressively increased until it reached the maximum depth of the sill in November and December (Fig. 3.3f). During winters with little ice cover MLD_{SI} remained large until spring, whereas it was 2 m or shallower in ice-covered months due to inverse stratification below the ice. In contrast to all other parameters considered above, wind speed and wind direction, WS and wind direction, WD, did not show a seasonal pattern but remained rather constant throughout the year (Figs. 3.3i, 3.18).

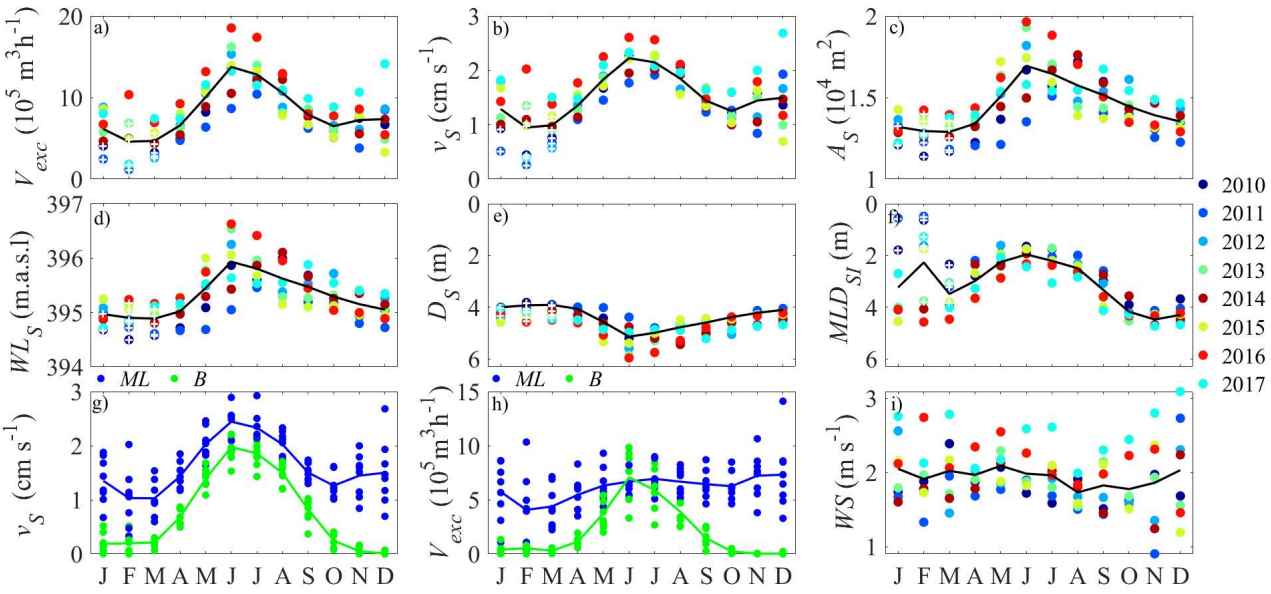

Figure 3.3: Seasonal pattern of water exchange V_{exc} and additional parameters relevant for the exchange across the sill. Seasonal pattern of a) V_{ex}, b) average current speed across $Trans_{M\text{-}R}$, v_S, c) area of the cross-section above the sill along of $Trans_{M\text{-}R}$, A_S, d) lake water level, WL_S, e) maximum depth along $Trans_{M\text{-}R}$, D_S, f) mixed layer depth at the deepest station of $Trans_{M\text{-}R}$, MLD_{SI}, g) seasonal pattern of the average current speed within and below the mixed layer along $Trans_{M\text{-}R}$ (MLD_S), $v_{S,ML}$ and $v_{S,B}$, respectively, h) seasonal pattern of the water exchange above and below MLD_S, $V_{exc,ML}$, and $V_{exc,B}$,

respectively, and i) wind speed *WS* close to the sill. The symbols represent the monthly-averaged quantity for each year. The black line connects the multi-annual average of the monthly values (years 2010 – 2017). The months with a monthly-mean ice cover above 30% of the lake surface are identified by a white "+".

Statistical analysis confirms a highly significant positive correlation between the multi-annual average (2010-2017) of the monthly-mean water exchange, $V_{exc,m}$, and the corresponding $v_{S,,m}$, $WL_{S,m}$, and $A_{S,m}$ (Tab. 3.5), whereas $V_{exc,m}$ is not significantly correlated with $MLD_{SI,m}$ (p = 0.06). Considering only the ice-free season, the correlations between $V_{exc,m}$ and $WL_{S,m}$, $A_{S,m}$, and $v_{S,m}$ (Fig. 3.4a-c), are similar as in the analysis based on all seasons, but additionally, $V_{exc,m}$ and $MLD_{SI,m}$ are significantly anti-correlated (Fig. 4d, Tab. 3.4). During the ice free season $v_{S,m}$ correlates similarly well with $WL_{S,m}$, $A_{S,m}$, and $MLD_{SI,m}$ as $V_{exc,m}$. E.g., $v_{S,m}$ is significantly correlated to $WL_{S,m}$ (r = 0.88, p <0.001) and significantly anti-correlated to $MLD_{SI,m}$ (r= - 0.82 , p = 0.01) (Fig. 3.4e-f, Tab. 3.4). However, neither $V_{exc,m}$ nor $v_{S,m}$ are significantly correlated to WS_m ($p \geq$0.4 in both cases, Fig.3. 4j-k, Tab. 3.4). Because the seasonal change in A_S is a direct consequence of the seasonal water level change, $WL_{S,m}$ explains essentially the entire variance of $A_{S,m}$ (R^2 = 1.00, Fig. 3.4i), and correlations of the other parameters with $WL_{S,,m}$ and $A_{S,m}$ provide the same results for r and p.

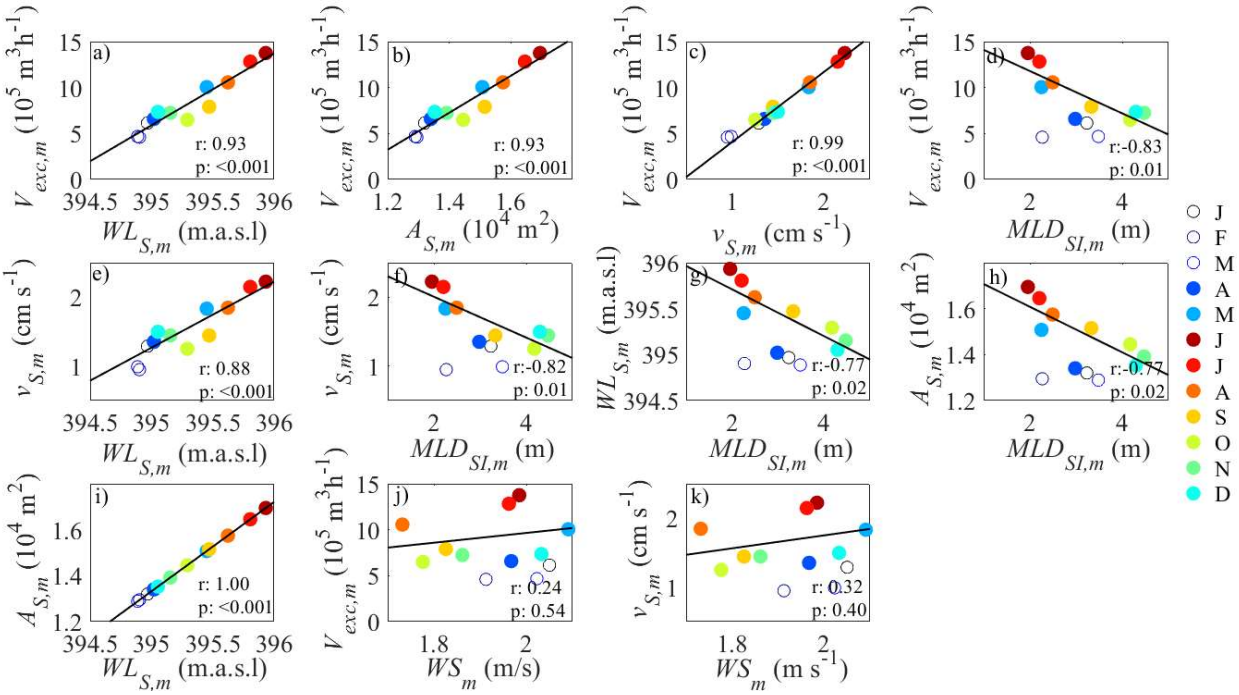

Figure 3.4: Correlations between the seasonal change of water exchange V_{exc} and other parameters relevant for water exchange at the sill. The symbols represent the simulated multi-annual averages (years 2010 – 2017) of the monthly-mean properties water exchange $V_{exc,m}$, water level $WL_{S,m}$, area of the cross-section along $Trans_{M\text{-}R}$ above the sill $A_{S,m}$, current speed across $Trans_{M\text{-}R}$, $v_{s,m}$, mixed layer depth at the station M_{SI}, $MLD_{SI,m}$, and wind speed close to the sill WS_m. Open circles indicate values for ice-covered months (January – March) that were not included in the regression analysis. The black line is the regression line. An overview on the statistical results of the linear regression analysis is provided in Tab. 3.6.

The exchange velocity across the sill was always substantially larger within the SML than below the SML (v_{S_ML} and v_{S_B}, Fig. 3.3g). Both, v_{S_ML} and $v_{S\_B,}$ showed a clear seasonal pattern with largest values in summer and smallest in winter and fall. The water exchange, however, followed a similar seasonal pattern only below the SML but not within the SML (V_{exc_ML} and V_{exc_B} Fig. 3.3h). Note, that v_{S_B} and V_{exc_B} become zero when MLD reaches the water depths D_S at the sill. During the ice-free season $v_{S\_B,m,}$, $v_{S\_ML,m}$, and $V_{exc\_B,m}$ were significantly anti-correlated to $MLD_{SI.m}$ (r = -0.92, p <0.001, r = -0.87, p <0.001, r = -0.92, p <0.001, respectively; Tabs. 3.4, 3.5) whereas the correlation between $V_{exc\_ML.m}$ and $MLD_{SI.m}$ was positive and not significant (r = 0.28, p = 0.47).

Seasonal water level changes not only affect the seasonal course of V_{exc}, but also that of v_s (Fig. 3.13). In a model run in which the outflow was adjusted to provide a constant water level from April until December, i.e. in which the water level in summer and fall was lower than in scenario T0, v_s is lower than in scenario T0. This result suggests that at lower water level the average frictional effect resulting from the interaction between currents and bottom boundary at the sill become larger.

In the open water at the deepest stations in GS and ZS, monthly mean vertical profiles showed a pronounced seasonal change in the vertical distribution of current speed (Fig. 3.19a-b). In the depth range from the surface down to the maximum depth of the sill current speed was almost uniform in July but decreased strongly with depth in December. In December currents were typically larger than in July. At the deepest station on the sill, M_{SI}, the vertical distribution of the monthly mean current speed was similar to that in the open water, but current speeds in July were larger than at M_{GS} and M_{ZS} (Fig. 3.19c). The monthly mean speed of the current across the sill was larger in July than in December and decreased only slightly with depth in both months (Fig. 3.19d).

The vertical averages of the monthly mean current speed from the surface down to D_S at M_{GS}, M_{ZS}, and M_{SI} showed a seasonal pattern during the ice-free period that was similar to that of v_S (Fig. 3.19, Fig. 3.3b), i.e. an increase between April and July and a decrease from July to October. From October onwards, the increase of the vertically averaged open water current speeds (Fig. 3.19e-f) was similar to that of the vertically averaged current speed at the sill (Fig. 3.19g), but more pronounced than the increase of the average speed of the current across the sill (Fig. 3.19h) and of the exchange velocity v_S (Fig. 3.3b).

3.3.3 Impact of a warmer climate on ice cover, stratification, and water exchange

In a warmer climate, characterized here by a 4°C increase in air temperature (scenario T4), all basins in LLC will be ice-free in all years. Therefore, inverse stratification did never develop in scenario T4 (Figs. 3.14, 3.16) and MLD_{SI} during January and February and in months

in March that were ice covered in scenario T0 was always larger than in the reference scenario T0 (Fig. 3.5c,f). In scenario T4, the onset of spring/summer stratification in GS and ZS was on average shifted forwards in time by 18 and 20 days, respectively, and the duration of stratification increased on average by 34 and 42 days, respectively (Tabs. 3.2—3.3). In April and May MLD_{SI} was shallower in scenario T4 than in scenario T0 whereas in summer and fall the absolute change in MLD_{SI} was small (Fig. 3.5c,f). In November and December $\Delta MLD_{SI} = 0$ because in scenario T0 and T4 the SML extends down to the maximum depth of the sill.

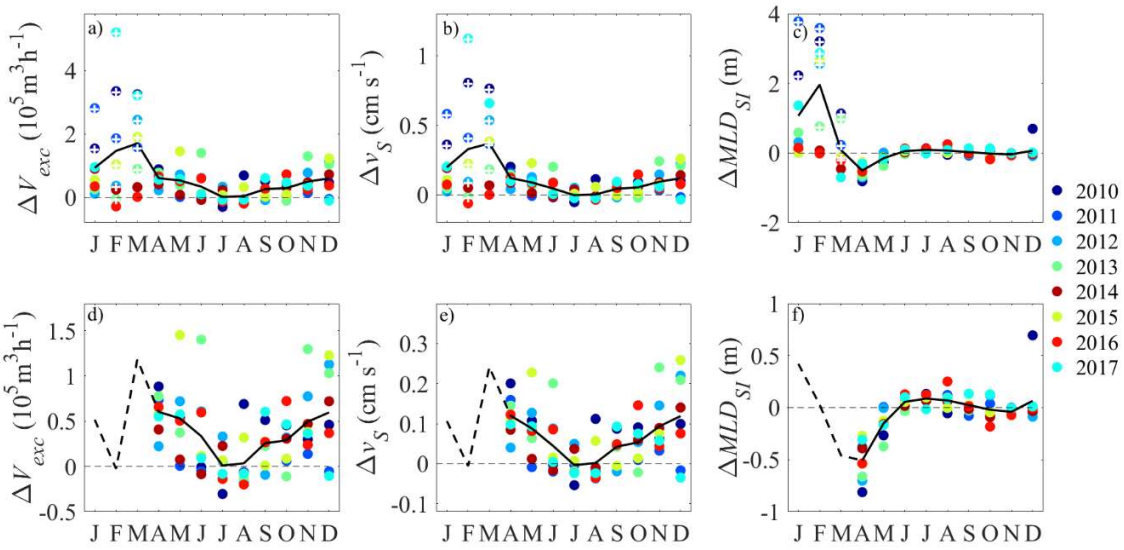

Figure 3.5: The impact of climate warming on water exchange, exchange velocity across the sill and mixed layer depth. Climate warming induced changes were determined from the monthly mean difference between the value of the parameters determined in scenario T4 minus its value in scenario T0. Depicted is the change in the monthly mean a) water exchange ΔV_{exc}, b) speed of the current across the sill Δv_S and c) MLD_{SI} (ΔMLD_{SI}). Panels d-f depict the corresponding parameters considering only the ice free season which allowed for a different scaling. The symbols represent monthly-averaged quantities in the years 2010-2017. The solid black line connects multi-annual averages, the dotted line connects multi-annual averages considering only ice-free month.

In years with abundant ice cover under reference conditions water exchange between January and March was substantially larger in scenario T4 than in T0 (ΔV_{exc} up to 5.2×10^5 m^3 h^{-1}, Fig. 3.5a,d). During the ice free season, the main increase in water exchange occurred in spring

(March – May) and also in late fall (November – December), but during the summer months ΔV_{exc} was close to zero (Fig. 3.5a,d).

Similar to V_{exc}, the exchange velocity v_S was typically larger in scenario T4 than in T0. Δv_S was particularly large during winter months, which were ice covered in scenario T0 (Fig. 3.5b,e). During the ice-free season v_s was larger in scenario T4 compared to scenario T0 especially in spring and late fall, whereas v_s remained essentially the same in both scenarios during the summer months (Figs. 3.5b,e).

During the ice-free season, the changes of V_{exc} and v_s, and of the corresponding properties within and below the SML, caused by climate warming, were linked to the change of MLD. ΔV_{exc} , $\Delta V_{exc,B}$, Δv_s , $\Delta v_{S,ML}$, $\Delta v_{S,B}$ were significantly anti-correlated to ΔMDL_{SI} (Tab. 3.6). Only $\Delta V_{exc,ML}$ showed a positive correlation to ΔMDL_{SI} which however was not significant (Tab. 3.6).

3.3.4 Impact of water level on ice cover, stratification, and water exchange

At the reduced water levels assumed in scenario W- the surface area covered by ice in winter was typically larger than at the increased water levels assumed in scenario W+ (Fig. 3.23). Nevertheless, the timing of ice-on and ice-off did not differ significantly between scenarios T0, W+, and W-. Also the onset, duration and strength of stratification was essentially the same in these three scenarios, i.e. monthly mean MLD_{SI} differed by less than 1.2 m between scenarios in all years and months, beside January 2011 for the scenario W+ (Fig. 3.6c,f).

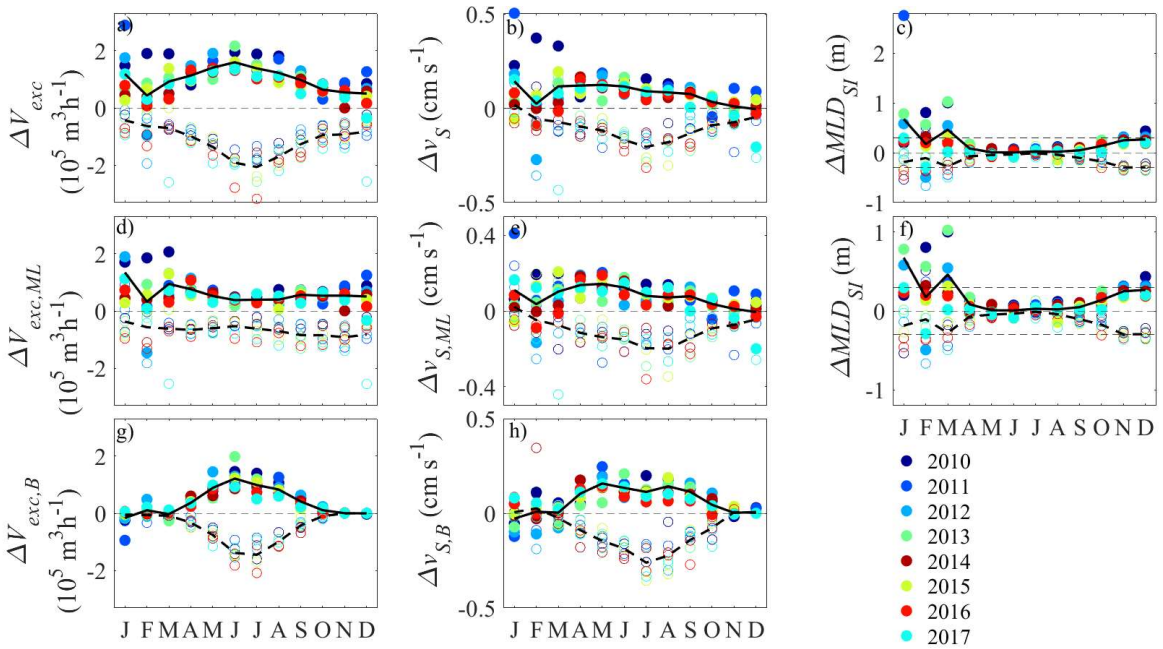

Figure 3.6: The impact of water level change (scenarios W+ and W-) on water exchange, exchange velocity across the sill and mixed layer depth. The panels depict the change of a) water exchange, ΔV_{exc}, considering the entire cross-section above the sill along $\text{Trans}_{\text{M-R}}$, d) water exchange above the MLD_S, $\Delta V_{exc,ML}$, and g) water exchange below the MLD_S, $\Delta V_{exc,B}$. The change of the mean speed of the current across the sill b) averaged over the entire cross-section between the basins, Δv_S, e) above the MLD_S, $\Delta v_{S,ML}$, and h) below the MLD_S, $\Delta v_{S,B}$. c) and f) The change in the mean layer depth at the station M_{SI} (ΔMLD_{SI}). The changes of the different properties, Δ are the monthly mean differences between the value of the property determined in scenario W+ and W-, respectively, minus its value in scenario T0. The symbols represent monthly-averaged quantities in the years 2010-2017. The solid black line connects multi-annual averages for the scenario W+, while the dashed black line connects multi-annual averages for W-.

Compared to scenario T0, V_{exc} increased in scenario W+ and decreased in scenario W- (Fig. 3.6a). The change in V_{exc} for the two water level scenarios is partially caused by the change in the area of the cross-section along $\text{Trans}_{\text{M-R}}$ above the sill: in scenario W+ A_S is larger and in scenario W- smaller than in scenario T0. However, not only V_{exc} and A_S but also v_s was larger in scenario W+ than in scenario T0 (Fig. 3.6b), although stratification did not change substantially.

The increase in V_{exc} and v_S in scenario W+ compared to scenario T0 was largest during summer and smallest in winter. In scenario W- not only ΔV_{exc} but also Δv_s was negative. In scenario W- the absolute values of ΔV_{exc} and Δv_s had a similar seasonality as in scenario W+ but were larger than in scenario W+.

The seasonal pattern of the impact of water level change on water exchange and current speed across the sill is dominated by the seasonal pattern of the changes below the SML, $\Delta V_{exc,B}$ and $\Delta v_{s,B}$ (Fig. 3.6g-h). The seasonal pattern of the changes of ΔV_{exc} and Δv_s within the SML, $\Delta V_{exc,ML}$ and $\Delta v_{s,ML}$, respectively, were weaker as those of $\Delta V_{exc,B}$, and $\Delta v_{s,B}$ (Fig. 3.6d-g). Future projections of the water level of Lake Constance suggest that water level change will be characterized by a reduced seasonal amplitude of the water level, i.e. higher levels in winter and lower levels in summer (scenario $W_{m,w+s-}$). In comparison to scenario W_m, that uses the average long term seasonal change of the water level, the simulations with scenario $W_{m,w+s-}$ predicted stronger inter-basin exchange during winter and reduced exchange during summer (Fig. 3.7). The annual mean impact of the water level change on water exchange assumed in scenario $W_{m,w+s-}$ was smaller than that of the water level changes assumed in scenario W_{m+} and W_{m-} and opposite between the year with abundant and the year with little ice cover (Fig. 3.7b,d).

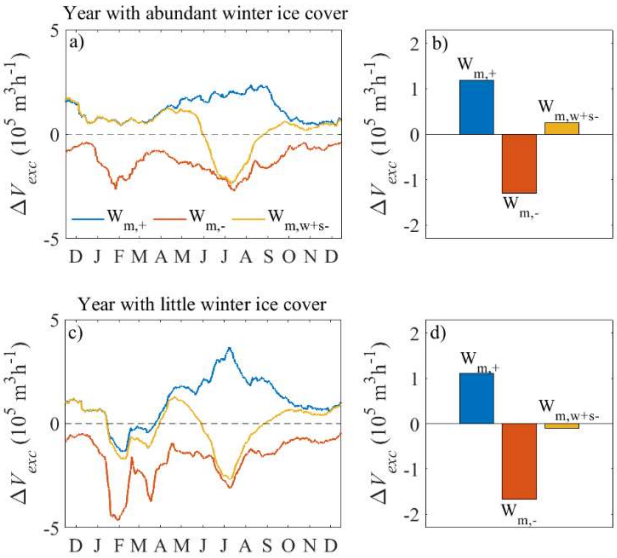

Figure 3.7: Impact of seasonally non-uniform changes in water level on water exchange V_{exc}. ΔV_{exc} is the difference between V_{exc} in the "seasonal water level scenarios" $W_{m,-}$ $W_{m,+}$, $W_{m,w+s}$ and scenario W_m. W_m assumes water levels that correspond to the multi-annual average seasonal course of the water level over the last 200 years (measured in LLC). $W_{m,w+s-}$ assumes 0.3 m higher water levels during the winter months and 0.3 m lower water levels during summer months than in W_m. Scenarios $W_{m,+}$ and $W_{m,-}$ assume a constant increase and decrease of the water level by 0.3 m, respectively. The time series of ΔV_{exc} is shown for the time period a) November 2009 – December 2010, as representative for years with abundant winter ice cover, and c) November 2015 – December 2016, as representative for years with little winter ice cover. Annual averages of ΔV_{exc} are provided b) for November 2009 – December 2010 and d) for November 2015 – December 2016.

3.3.5 Transport of dissolved substance from the main inflow to GS

Dissolved substances introduced into LLC by river Seerhein are transported from its mouth in RS via ZS to GS (Fig. 3.26). The vertical distribution of the tracer along $Trans_{I-G}$ changed substantially during the season in 2010. Two days after the introduction of the tracer at Seerhein, tracer was vertically mixed in RS before reaching GS during the winter months,

whereas between May and October the tracer concentrations were maximal within the thermocline of RS and ZS (Fig.3.26e-j). However, only in July and August 2010 tracer concentrations above the sill between ZS and GS were high (Fig. 3.26g-h). The tracer mass reaching GS within one month was substantially lower during winter than in summer (Fig. 3.8a). The seasonal pattern of the fractation of tracer mass introduced by Seerhein reaching GS (Fig. 3.8a) was positively correlated to WL_S (r = 0.55, p <0.001) and to the average $MLH_{I\text{-}G}$ (r = 0.37, p<0.001). Between June and September $m_{TR,25}$ was larger than in spring and winter (Fig 8) indicating a higher connectivity of surface water between inflow in RS, ZS and GS. Furthermore, in June and September a larger fraction of the river water reached GS faster than in spring and winter, as is indicated by the comparatively rapid increase of m_{TR} in these months (Fig. 3.31).

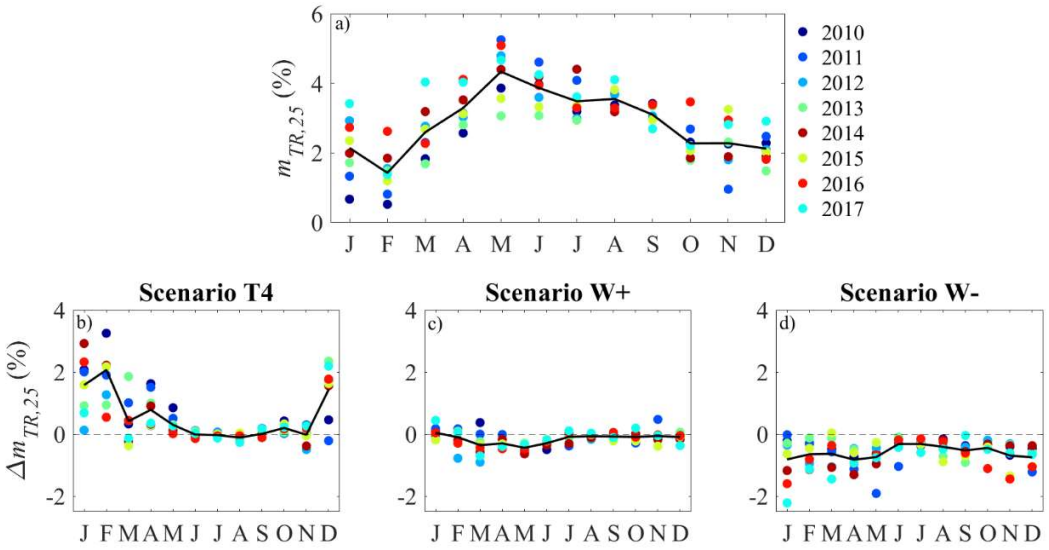

Figure 3.8: Seasonal pattern of the fraction of tracer mass introduced by river Seerhein reaching GS, $m_{TR,25}$, (a) and the impact of climate warming and water level change (b-d). Panels (b) to (d) depict monthly changes in $m_{TR,25}$, $\Delta m_{TR,25}$, that are caused by the scenarios T4, W_+ and W_-, respectively.

In a warmer climate (scenario T4) substantially more tracer reached GS in winter and late fall than under current conditions (scenario T0) (Fig. 3.8b). E.g. in January and February the tracer mass transported into GS in scenario T4 is typically twice as large as in the reference

scenario T0 and the increase of $m_{TR,25}$ between scenarios T4 and T0, $\Delta m_{TR,25}$, can be more than 600% larger than $m_{TR,25}$ under reference conditions (February 2010: $m_{TR,25}$= 0.53% and $\Delta m_{TR,25}$ = 3.3%). In contrast, climate warming has essentially no effect on the connectivity between river Seerhein and GS during summer. A seasonally constant water level change as in the scenarios W+ and W- results in a comparatively small impact on the tracer mass reaching GS(Fig. 3.8c-d).

3.4 Discussion

3.4.1 Inter-basin exchange in LLC: Controlling factors

The identification of the main drivers controlling seasonal and inter-annual changes in inter-basin exchange in lakes with complex morphometry is important for the understanding of spatial heterogeneities in the distributions of dissolved substances and organisms and for the assessment of the potential impact of climatic and hydrological changes on these distributions.

The numerical simulations revealed a strong seasonal pattern in the inter-basin exchange between GS and ZS. The seasonal change in $V_{exc,m}$ results from two effects: a) the change in the exchange velocity across the sill between GS and ZS and b) the change in the area of the cross-section through which water flows across the sill:

$$\delta V_{exc,m} = \delta v_{S,m} \cdot A_{S,m,r} + v_{S,m,r} \cdot \delta A_{S,m} + \delta v_{S,m} \cdot \delta A_{S,m}$$

where $\delta V_{exc,m} = \delta V_{exc,m} - V_{exc,m,r}$, $\delta v_{S,m} = \delta v_{S,m} - v_{S,m,r}$, and $\delta A_{S,m} = \delta A_{S,m} - A_{S,m,r}$, and $V_{exc,m,r}$, $v_{S,m,r}$, and $A_{S,m,r}$ are $V_{exc,m}$, $A_{S,m}$ and $v_{S,m}$ at a reference month. The contribution of $\delta v_{S,m}$ to the seasonal change in water exchange, $\delta v_{S,m} \cdot A_{S,m,r}$, is typically larger than the contribution to $\delta V_{exc,m}$ due to the change in A_{Sm}, $v_{S,m,r} \cdot \delta A_{S,m}$. The correlation of the changes in $v_{S.m}$ and $A_{S,m}$, $\delta v_{S,m} \cdot \delta A_{S,m}$, has only a very small influence on $\delta V_{exc,m}$ (Fig. 3.9).

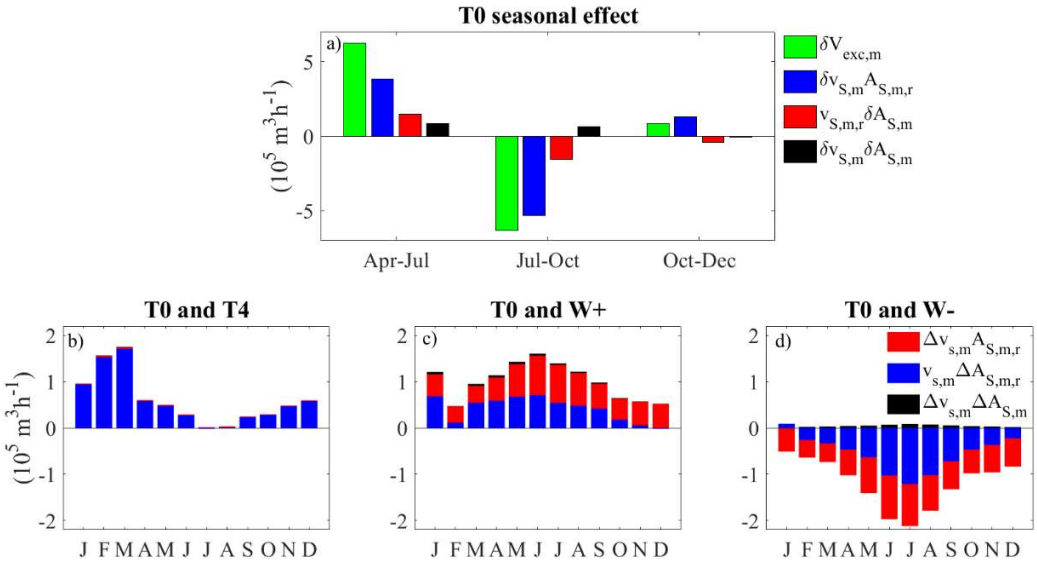

Figure 3.9: The contributions of exchange velocity and the cross-sectional area above the sill to the change in the exchange velocity. (a) Seasonal changes of $V_{exc,m}$ in scenario T0, $\delta V_{exc,m}$, and the contribution to $\delta V_{exc,m}$ of the seasonal change in the exchange velocity, $\delta v_{S,m}$, and in the cross sectional area above the sill, $\delta A_{S,m}$: $\delta V_{exc,m} = \delta v_{S,m} \cdot A_{S,m,r} + v_{S,m,r} \cdot \delta A_{S,m} + \delta v_{S,m} \cdot \delta A_{S,m.}$. $v_{S,m,r}$ and $A_{S,m,r}$ are $A_{S,m}$ and $v_{S,m}$ at the reference months April, July, and October, respectively. (b-d) The contribution of $v_{S,m}$ and $A_{S,m}$ to changes in $V_{exc,m}$ resulting from warming (b: Scenario T4) and water level changes (c: Scenarios W+ ; d: Scenario W-): $\Delta V_{exc,m} = \Delta v_{S,m} \cdot A_{S,m,r} + v_{S,m,r} \cdot \Delta A_{S,m} + \Delta v_{S,m} \cdot \Delta A_{S,m}$. Δ denotes the difference between a property in T4, W+, or W- minus its value in reference scenario T0 in the corresponding month. $A_{S,m,r}$ and $v_{S,m,r}$ are the values of $A_{S,m}$ and $v_{S,m}$ in the reference scenario T0.

During the ice-free period, $\delta v_{S,m} \cdot A_{S,m,r}$ was typically more than two times larger than $v_{S,m,r} \cdot \delta A_{S,m}$, e.g., from April to July and from July to October the change in the average current speed across the sill accounts for more than 70% of the increase and decrease, respectively, of the water exchange $V_{exc,m}$ (Fig. 3.9a). Between October and December, $v_{S,m}$ increased and $A_{S,m}$ decreased, but because the absolute value of $\delta v_{S,m} \cdot A_{S,m,r}$ was about two times larger than the absolute value of $v_{S,m} \cdot \delta A_{S,m,r}$, $V_{exc,m}$ increased (Fig. 3.9a).

Since the seasonal change of $V_{exc,m}$ results from the seasonal change in A_{Sm} and $v_{Sm,}$ it is controlled by the factors determining $A_{S,m}$ and v_{Sm}. The seasonal change in $A_{S,m}$ is proportional to the seasonal change in water level (Fig. 3.3d) and hence determined by the hydrology in the catchments, i.e. by the inflows and outflows of the lake system. The seasonal change in $v_{S,m}$ results from the complex interaction between wind forcing, stratification, and water level affecting the vertical distribution of currents. Furthermore, $v_{S,m,}$ is influenced by bottom friction, which depends on morphometry and water level at the sill (Fig. 3.22).

Wind speed and wind speed squared, which is proportional to forcing at the lake surface, remained rather constant over the season (Fig. 3.18). Thus, the seasonal course in $v_{S,m}$, and also of the current speed at the deepest stations in GS and ZS and at the sill, are not caused by the seasonal changes in wind forcing, but connected to the seasonal change in stratification, here indicated by the seasonal change in MLD, and in water level affecting friction.

Between April and October, $v_{S,m}$ and the vertical average of the current speed at M_{GS} and M_{ZS} in the upper part of the water column (down to the depth of the sill) are larger at shallower and smaller at larger MLD (Figs. 3.3b and 3.19). Apparently, the efficiency of the transfer of wind energy to kinetic energy in the horizontal current field in the upper ~5 m of the water column increases with increasing stratification. Stratification suppresses vertical motion and thus less of the kinetic energy transferred by wind forcing to horizontal motions may be lost to vertical motions and turbulence (Bennett, 1974). Furthermore, stratification supports internal seiching that channels wind energy into oscillatory motions of the entire water column and thus may support larger horizontal current speeds by enhancing energy transfer from wind to water. The vertical distribution of the current speed in summer at M_{GS} and M_{ZS} (Fig. 3.19) suggest the impact of seiching, as the current speed does not decrease much with depth but remains rather constant. Indeed, the velocity profiles at M_{GS} and M_{ZS} show strong opposing currents within the upper 5 m that change periodically with time (Fig. 3.20).

From October to December current speeds at M_{GS}, M_{ZS} and M_{SI} increase, while the lake is essentially fully mixed in November and December (Fig. 3.19). Monthly mean vertical profiles of current speed at M_{GS} and M_{ZS} show a larger but rather monotonous decrease from the surface

to larger depth than summer profiles. In this period, a large portion of the water column in the open water moves synchronously in one direction. The inertia of this water body supports more continuous flow throughout the water column by reducing the influence of changing directions of wind forcing. During stratified conditions in summer, the currents move instead in opposite directions within and below the SML (Fig. 3.20) as a consequence of seiching. Hence, during unstratified conditions, the losses by friction within the water column are reduced, resulting in increased wind driven current speeds. Also in Lake Erie strong wind-driven currents were the cause for large inter-basin exchange during unstratified conditions (Niu et al., 2015).

With shallowing of the MLD in summer, the exchange velocity within and below the SML increased (Fig. 3.3g). However, despite the seasonal increase of $v_{s,ML}$, $V_{exc,ML}$ did not show a strong seasonal pattern, because the shallowing of the MLD in summer is associated with a decrease of the area of the cross-section available for water exchange within the SML. The decrease in cross-sectional area of the SML apparently compensated the increase of $v_{s,ML}$. The seasonal change in V_{exc} was therefore dominated by the seasonal change in $V_{ex,B}$, which was a consequence of the combined effect of the seasonal change in $v_{S,B}$ and the seasonal increase in the cross-sectional area at the sill below the SML. The latter resulted from the decrease in MLD and additionally from the seasonal increase in water level.

The exchange velocity below the MLD increases more strongly than the exchange velocity within the SML (Fig. 3.3g). At same water depth, the shallower MLD the more currents from a larger distance to the bottom of the sill are included in the estimate of $v_{s,B}$. This may explain the comparatively large change in $v_{s,B}$ with decreasing MLD, because the effect of bottom friction on the current speed decreases with the distance to the bottom.

The scenario with constant water level in summer revealed that the seasonal increase in water level contributed to the increase of the overall exchange velocity v_s (Fig. 3.22). This result suggests that at higher lake water level the impact of bottom friction on average currents is reduced (Gregg, 2004; Rueda & Cowen, 2005) and that water level changes therefore have an indirect impact on the seasonal change of V_{exc} by altering the effects of bottom friction. Summarizing for the open water period, the seasonal changes in v_s, $v_{s,ML}$, and $v_{s,B}$ result from I) seasonal changes in the efficiency of the energy transfer from wind forcing to horizontal water

currents, II) seasonal changes in water level affecting the impact of friction on the current speed at the sill, and III) seasonal changes in cross-section available for exchange.

The formation or absence of ice is independently affecting water exchange causing high inter-annual variability of water exchange during winter months. The ice layer inhibits the transfer of wind energy to the water at the lake surface and thus leads to reduced horizontal current speeds and smaller inter-basin exchange (Fujisaki et al., 2013; Nguyen et al., 2017). Inter-basin exchange can therefore differ substantially between winters with the same water level but different ice coverage (Figs. 3.2a and 3.3a). However, the annual mean exchange is not necessarily larger in years with little winter ice cover than in years with abundant winter ice cover (Fig. 3.2) because water exchange is largest during the summer months, which compensates for low exchange during ice covered winters.

The spread of the river inflow into GS is affected by lake thermal structure (Fig. 3.26). In summer, river Seerhein intruded as density plume into the metalimnion of RS and ZS as its typical for river inflows during the stratified season (Serruya, 1974; Hebbert et al., 1979; LaBounty & Horn, 1997; Romero & Imberger, 2003; Effler et al., 2010; Laborde et al., 2010; Cortés et al., 2014) (Fig. 3.26). During unstratified conditions between late fall and spring, the introduced river water was typically vertically mixed already in RS and ZS before reaching the sill (Fig. 3.26). Hence, during strong stratification in summer tracer with high concentration was located at comparatively shallow depth in ZS and therefore could be more efficiently transported into GS than during other seasons. In addition, V_{exc} is maximal during summer supporting a larger transport of tracer mass into GS in summer than between fall and spring.

3.4.2 Impact of climate warming and long-term water level change

Our simulations demonstrate that climate warming and long-term changes in water level can significantly affect the seasonal and the inter-annual pattern of inter-basin exchange in lakes. The change in water exchange patterns is a consequence of changes in ice cover, in thermal stratification, and in water level affecting cross-sectional area and the impact of friction at a sill.

In LLC, climate warming leads to reduced ice cover and, at an increase in the air temperature by 4°C, even to ice-free conditions in all years. The model results are consistent with observations from numerous lakes, which have demonstrated a substantial reduction in ice cover with warming over the last century (Magnuson et al., 2000), and with the results from several modeling studies investigating the impact of climate warming on ice cover (Walsh et al., 1998; Fang & Stefan, 2009; Yao et al., 2014; Woolway & Merchant, 2019; Gronchi et al., 2021). In addition to the loss in ice-cover, our simulations indicate that climate warming results in an earlier onset of stratification, a longer duration of the stratified period and the development of a shallower MLD especially in spring and fall. These predicted changes in stratification are consistent with observations (e.g. Livingstone et al., 2003) and results from several modelling studies (Robertson & Ragotzkie, 1990; Coats et al., 2006; Peeters et al., 2007a, ; MacKay et al., 2009; Perroud et al., 2009; Dibike et al., 2011; Wahl & Peeters, 2014).

The effects of climate warming on ice cover and stratification result in higher inter-basin exchange especially during winter, spring and late fall. These changes in water exchange are caused by changes in the exchange velocity v_S , as is indicated by the large contribution of $\Delta v_{S,m} \cdot A_{S,m,r}$ to $\Delta V_{exc,m}$ (Fig. 3.9b) wehreby $A_{S,m,r}$ refers to $A_{S,m}$ in the same month in scenarioT0. The most significant increase in inter-basin exchange occurs during the winter months because the loss of ice cover allows for increased transfer of wind energy to the horizontal currents, i.e. an increased importance of wind driven currents for inter-basin water exchange. The change in stratification apparently also results in larger v_s and thus in larger water exchange, only in spring and late fall, but not during the summer months. During the summer, MLD was already rather small under reference conditions such that climate warming had comparatively small impact on water column stratification and current speed.

In contrast to climate warming an increase in water level (scenario W+) causes the largest increase in water exchange during summer and the smallest in February. The water level increase is associated by an almost proportional increase in the area of the cross-section above the sill, and thus a seasonally homogenous increase in water exchange. However, the contribution due to the increased $A_{S,m,}$ to the changes in water exchange caused by scenario W+, $\Delta V_{exc,m}$ ($\Delta V_{exc,m=} \Delta v_{S,m} \cdot A_{S,m,r} + v_{S,m,r} \cdot \Delta A_{S,m} + \Delta v_{S,m} \cdot \Delta A_{S,m}$), increases seasonally (Fig. 3.9c). Subscript *r* refers to

conditions in the same month in scenario T0. In summer the same change in cross section caused by the water level scenario $\Delta A_{S,m}$ results in a larger contribution $v_{S,m,r} \cdot \Delta A_{S,m}$ than in winter because $v_{S,m}$,r ($v_{S,m}$ in reference scenario T0) is larger in summer is larger than in winter. In scenario W+, $\cdot \Delta v_{S,m}$ contributed as much to $\Delta V_{exc,m}$ as $\cdot \Delta A_{S,m}$, and the increase of $v_{S,m}$ was larger in summer than in winter (Fig. 3.6b). Increased water levels result in larger exchange velocity $v_{S,m}$, because at a higher water level the effects of bottom friction are reduced. Further, at higher water levels the integration in the calculation of $v_{S,m}$ includes velocities at larger distance from the bottom, that typically have a larger magnitude of the component across the transect than currents closer to the sill.

In the scenario with reduced water level (scenario W-) $\Delta v_{S,m} \cdot A_{S,m,r}$ and $v_{S,m,r} \cdot \Delta A_{S,m}$ are both negative because the seasonal changes in $v_{S,m}$ and $A_{S,m}$ are smaller than in the reference scenario T0 (Fig. 3.9d). Similar to W+, the absolute values of $\Delta v_{S,m} \cdot A_{S,m,r}$ and $v_{S,m} \cdot \Delta A_{S,m,r}$ were about the same and largest in summer (Fig. 9d). Since the absolute change of $v_{S,m}$ caused by W+ with respect to T0 is smaller than the one caused by W+, the absolute value of $\Delta v_{S,m} \cdot A_{S,m,r}$ was larger in W-. This supports the hypothesis that the bottom friction decrease with increasing water level. Climate warming, characterized by an increased air temperature of 4°C, and water level change, characterized by a level increase of 0.3 m throughout the year, have both a strong impact on inter-basin water exchange. The results of the scenarios T4 and W+ show a similar maximum change in V_{exc} but the impact on V_{exc} has an opposite seasonal patterns.

Projections for Lake Constance suggest a reduced seasonal amplitude of water levels, i.e. higher water levels in winter and lower water levels in summer than today (Ostendorp et al., 2020) (scenario $W_{m,w+s-}$, Fig. 3.24). Consequently, water exchange in scenario $W_{m,w+s-}$ increased in the winter months and decreased in the summer months. Hence climate warming together with the projected seasonal change in water level will substantially enhance water exchange during the winter months, as increased wind forcing due to reduced ice cover in a warmer climate combines with increased area of the cross-section for water exchange and reduced effects of bottom friction. In summer, in contrast, climate warming has essentially no impact and reduced water levels cause a decrease in V_{exc}. Overall, the seasonal pattern of inter-basin exchange in

LLC is therefore expected to change substantially in the future and will be characterized by much stronger water exchange in winter and lower water exchange in summer than today.

However, the seasonal pattern of the water level change in LLC is strongly influenced by the large alpine catchment of ULC with snow melt in the catchment causing a comparatively late increase of the water level in early summer. Projected seasonal water level changes depend on the assumption of a change in precipitation and snow melt during winter. Hence, other lake systems may experience a change in the seasonal pattern of water level due to climate change that differs from that described here in scenario $W_{m,w+s-}$. Nevertheless, the results from the scenarios with constant shifts in water level W+ and W- provide a good indication of the implications of water level changes and can serve as a guideline for other lakes.

3.4.3 Implications of the changes in connectivity between basins

The seasonal pattern of water exchange in LLC implies a stronger lateral exchange of dissolved substances and organisms between GS and ZS and thus laterally more homogenous conditions in summer than in winter.In a warmer climate, the increase of water exchange in winter together with the increase in light availability resulting from shorter ice cover duration or absence of ice cover, will impact phytoplankton bloom development in ZS and GS that typically occurs between January and March (IGKB 2018). Reduced summer water levels predicted for LLC in a warmer climate are expected to cause reduced water exchange and thus larger horizontal differences of dissolved substances and organisms between the sub-basin of LLC especially during summer months. E.g. cyanobacteria typically develop larger abundances in GS than in ZS and RS (IGKB 2012, IGKB 2016). A reduction of the water exchange across the sill in summer may imply a reduction of the export of cyanobacteria from GS to ZS, which may result in larger cyanobacteria populations in GS than today.

Dissolved phosphorus concentrations are typically lower in ULC than in LLC. Thus an increased connectivity between GS and ULC expected for a warmer climate will affect nutrient concentrations in GS especially in winter/early spring and thus may alter primary production during spring bloom and the consecutive plankton development.

Summarizing, climate warming and water level changes not only alter the amount of water exchanged between basins, but also the seasonal pattern of inter basin exchange. The impact of climate warming and water level change on the inter-connectivity between basins therefore can be expected to have a seasonally differential impact on the lateral distribution of dissolved substances and organisms in lakes.

Acknowledgments

This study was financially supported by the German Research Foundation (DFG) within the framework of the RTG R3 (Research Training Group – Responses to biotic and abiotic changes, Resilience and Reversibility of lake ecosystems), grant number 298726046/GRK2272/A4.

We thank Beatrix Rosenberg and Josef Halder, who helped with the field work. We acknowledge Chris Dallimore from Hydronumerics for his help and support with the model setting.

Supplements

3A. Model of Lake Constance

The hydrodynamic model of LC used to derive the inflow temperature of the Seerhein was previously set up and validated in Caramatti et al. (2020). The model was characterized by a 300 m x 300 m horizontal grid and 70 vertical layers of variable thickness. The vertical resolution was 1 m in the upper 29 layers and 10 m in the lower 10 layers. Between the 30th and 57th layer the vertical resolution varied slowly between 1 and 10 m. The major inflows of LC, according to Stewart (1988), were considered and the water level was kept constant to the mean water level during the simulated period (396 m.a. s. l.), by adjusting the outflow discharge with a water balance.

Water temperature in LC was initialized by means of data from a thermistor chain (RBR-solo, vertical resolution 0.5 to 2 m in the upper 20 m and coarser below) at the station EU, the deepest station in the Überlingen basin of ULC, and data with a coarser resolution (from 5 to 20 m) from the Landesanstalt fuer Umwelt Baden-Wuerttemberg (LUBW) at station FU (the deepest point of ULC), M_{GS}, M_{ZS} and M_{RH}. Horizontally resolved wind fields (COSMO-MeteoSwiss, resolution 2.2 km until August 2016 and then 1.1 km) were linearly interpolated to the computational grid of LC. Except for the wind field, the model was driven with horizontally uniform meteorological data. For the climate warming scenario (T4) the model was run with increased air temperature (+4°C) and increased inflow temperature (95% of the increase in air temperature). The new initial conditions were derived after a pre-run repeating the meteorological and flow conditions of the year 2009 in a warmer scenario.

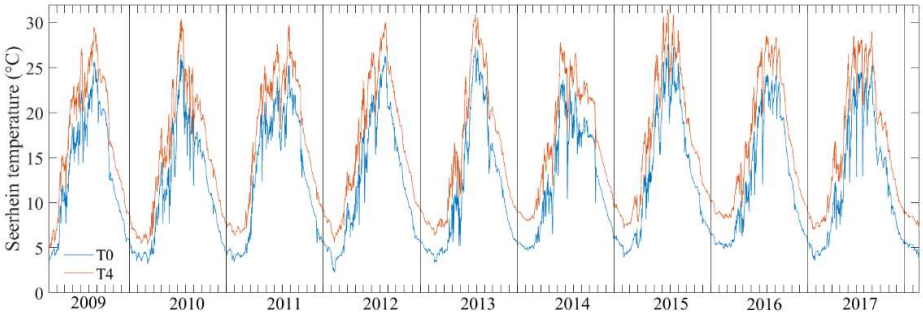

Figure 3.10: Simulated multi-annual course of Seerhein temperature in the scenarios T0 and T4.

3B. Model Validation

Model results and observations of water temperature were compared at the two stations M_{GS} and M_{ZS} for three consecutive years (2010, 2011, and 2012) to validate the model performance in terms of thermal structure throughout the season and among years (Fig. 3.11).

The agreement between simulated thermal structure and monthly temperature profiles was evaluated using the root mean square error (RMSE). A mean RMSE was computed for each of the four periods described above (December-March, April-May, June-September, October-November) and is presented in Tab. 3.1. The model represents the thermal structure most accurately between October and March, with a mean RMSE between 0.37 and 1.08°C in ZS and 0.97 and 1.82°C in GS. During the winter months (from December-March), the mean RMSE was 0.85, 0.37, 0.45°C in ZS for the years 2010, 2011, 2012 and 1.03, 0.98°C in GS for the years 2010, 2012 (no data available in 2011). The simulation was least accurate in the period June-September, with a maximum mean RMSE of 1.49 at MZS and 2.34°C at M_{GS}. In each case, the model reproduced the thermal structure more accurately at station M_{ZS} than at M_{GS}. Text published in Caramatti et al. (2020).

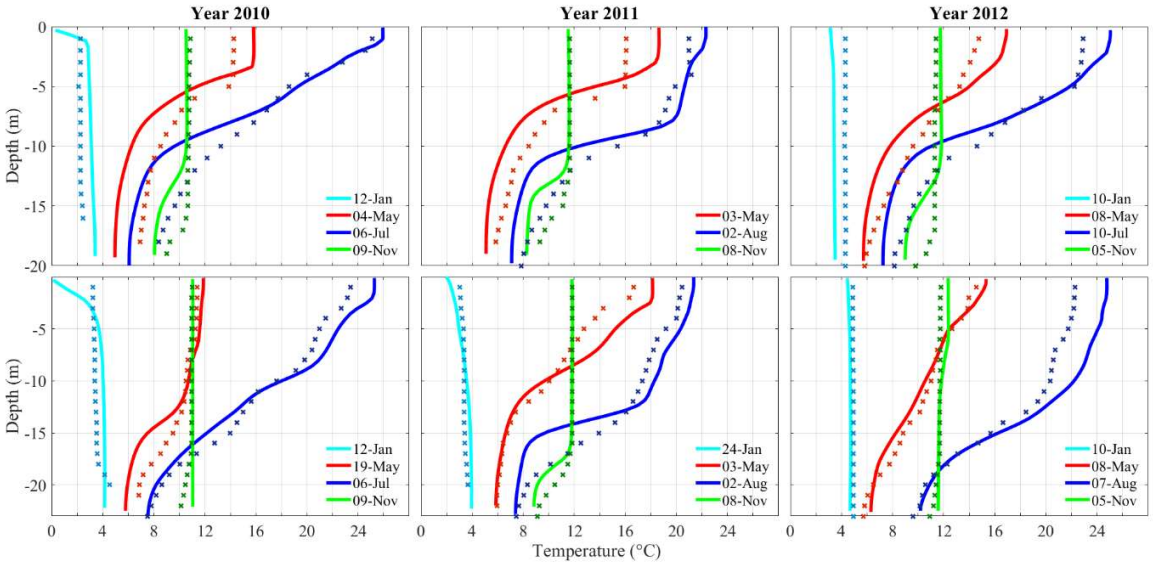

Figure 3.11: Model validation: Seasonal differences in thermal structure between observed (continuous line) and simulated (dotted line) temperature in Gnadensee (GS) and Zeller

See (ZS) for characteristic snapshots of three consecutive years (2010, 2011 and 2012). Figure published in Caramatti et al. (2020).

Table 3.1: Model validation based on temperature. RMSE between measured and simulated temperature profiles of the sub-basins Gnadensee and Zeller See. Table published in Caramatti et al. (2020).

Gnadensee

RMSE (°C)	Dec. - March	April - May	June – Sept.	Oct. – Nov.
2010	1.03	2.16	2.26	1.03
2011	-	2.01	2.06	1.82
2012	0.98	1.59	2.34	0.97

Zeller See

RMSE (°C)	Dec. - March	April - May	June – Sept.	Oct. – Nov.
2010	0.85	1.12	1.32	1.02
2011	0.37	0.97	2.22	1.08
2012	0.45	0.51	1.49	0.35

The simulated current velocities across the sill between Gnadensee (GS) and Zeller See (ZS) were compared with field measurements taken with an Aquadopp HR Profiler (Nortek) at position M_{AQ} (Fig. 3.12). The field instrument was looking upward measuring between 0.7 – 1.7 m above the ground (mean water depth: 2.5 m) with a high vertical resolution of 0.05 m and a sampling rate of 5 s. Field data was collected between 7/7/2018 – 28/11/2018. The model output was extrapolated at the position M_{AQ} and at the depth investigated by the Aquadopp. The simulated components of the current velocity were interpolated to the time of the field measurements (1 hour interval). Both time series were then smoothed weekly and thereafter the RMSE between model and data was calculated.

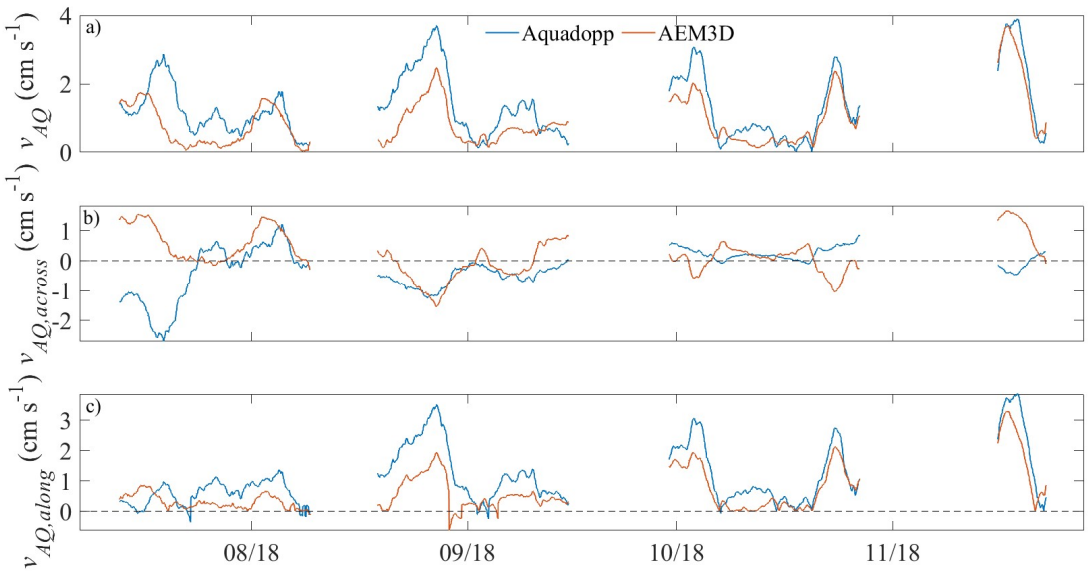

Figure 3.12: Model validation of currents across the sill between GS and ZS. Comparison between observed (blue) and simulated (orange) current speed (v_{AQ}), as well as the along- and across-velocity components ($v_{AQ,along}$ and $v_{AQ,across}$) at station M_{AQ} with respect to $Trans_{M\text{-}R}$.

3C. Lake thermal structure

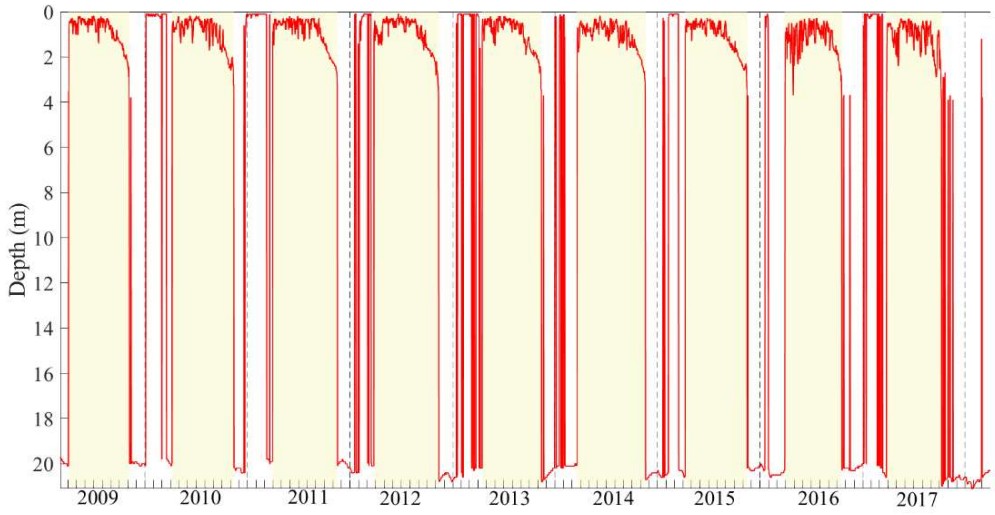

Figure 3.13: Simulated MLD_{GS}. The duration of the stratification period at M_{GS} is shaded in yellow.

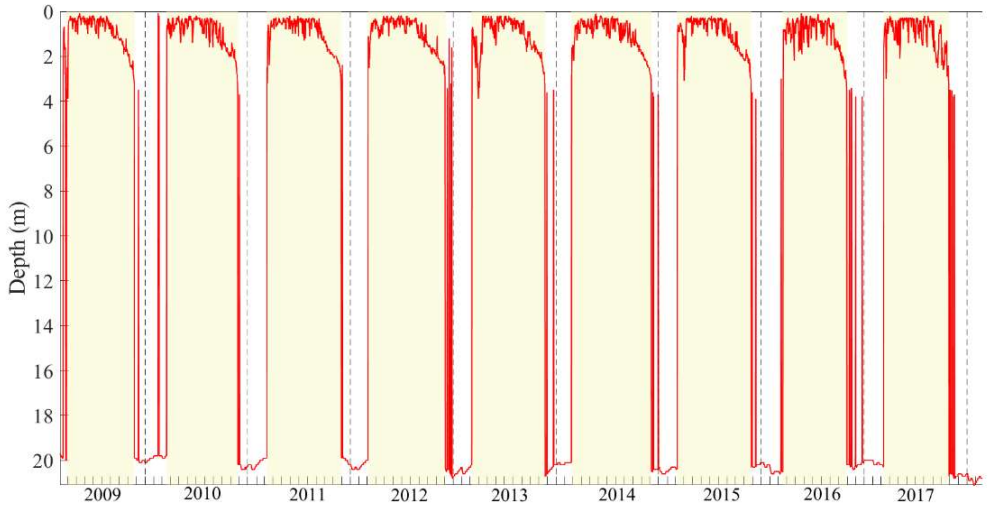

Figure 3.14: Simulated MLD_{GS} in the scenario T4. The duration of the stratification period at M_{GS} is shaded in yellow.

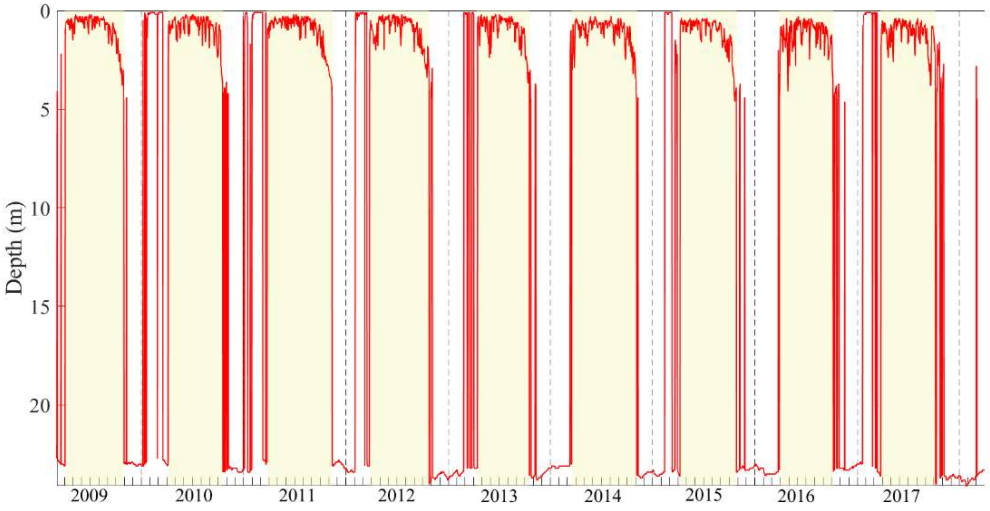

Figure 3.15: Simulated MLD_{ZS}. The duration of the stratification period at M_{ZS} is shaded in yellow.

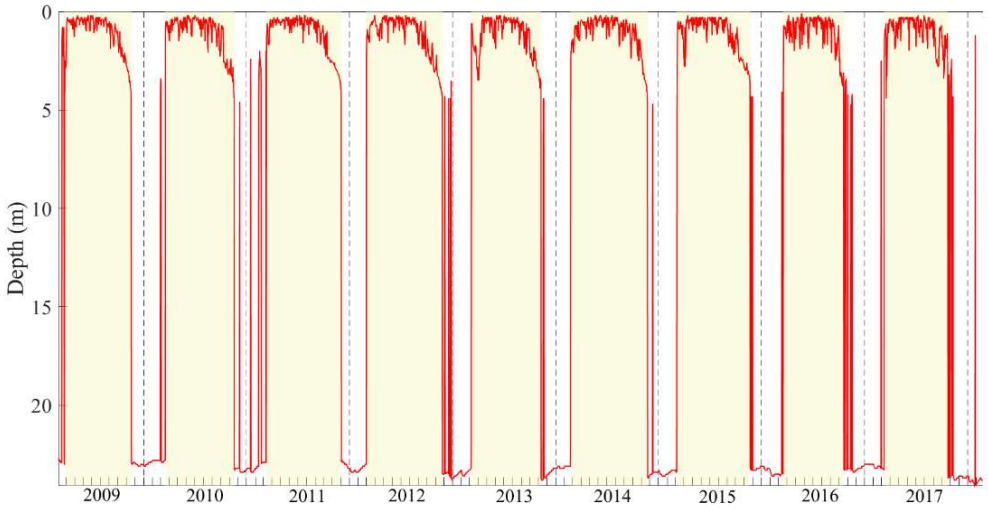

Figure 3.16: Simulated MLD_{ZS} in the scenario T4. The duration of the stratification period at M_{ZS} is shaded in yellow.

Table 3.2: Timing and deviation of the summer stratification period between the reference scenario T0 and the climate change scenario T4 at station M_{GS}.

Year	Beginning of stratification (doy)	Ending of stratification (doy)	Duration stratification (days)	Δ Beginning of stratification (days)	Δ Ending of stratification (days)	Δ Duration of stratification (days)
Scenario T0						
2009	91	308	217	-	-	-
2010	95	315	220	-	-	-
2011	88	319	231	-	-	-
2012	84	315	231	-	-	-
2013	104	315	211	-	-	-
2014	77	321	244	-	-	-
2015	98	318	220	-	-	-
2016	88	291	203	-	-	-
2017	84	280	196	-	-	-
Average	90	309	219	-	-	-
Scenario T4						
2009	85	326	241	- 6	18	24
2010	76	329	253	- 19	14	33
2011	69	333	264	- 19	14	33
2012	61	336	275	- 23	21	44
2013	90	325	235	- 14	10	24
2014	53	339	286	- 24	18	42
2015	65	329	264	- 33	11	44
2016	76	304	228	- 12	13	25
2017	68	300	232	- 16	20	36
Average	71	325	253	- 18	15	34

Table 3.3: Timing and deviation of the summer stratification period between the reference scenario T0 and the climate change scenario T4 at station M_{ZS}.

Year	Beginning of stratification (doy)	Ending of stratification (doy)	Duration stratification (days)	Δ Beginning of stratification (days)	Δ Ending of stratification (days)	Δ Duration of stratification (days)
Scenario T0						
2009	91	301	210	-	-	-
2010	94	289	195	-	-	-
2011	83	315	232	-	-	-
2012	83	296	213	-	-	-
2013	103	288	185	-	-	-
2014	75	307	232	-	-	-
2015	97	298	201	-	-	-
2016	87	279	192	-	-	-
2017	83	278	195	-	-	-
Average	88	295	206	-	-	-
Scenario T4						
2009	83	320	237	- 8	19	27
2010	76	320	244	- 18	31	49
2011	69	335	266	- 14	20	34
2012	59	328	269	- 24	32	56
2013	65	312	247	- 38	24	62
2014	52	325	273	- 23	18	41
2015	64	324	260	- 33	26	59
2016	76	291	215	- 11	12	23
2017	68	294	226	- 15	16	31
Average	68	317	249	- 20	22	42

3D. COSMO wind field

The COSMO wind field (MeteoSwiss) was linearly interpolated to the computational grid of LLC and ULC. The wind field had a spatial resolution of 2.2 km before August 2016 and afterwards 1.1 km. The north- and east-wind components were derived in the closest points to $Trans_{M\text{-}R}$ of both grids (Fig. 3.17) to investigate their correlation with the inter-basin water exchange.

Wind components were computed along and across $Trans_{M\text{-}R}$ ($Across_w$, $Along_w$) and then averaged monthly to observe the existence of a wind seasonal pattern. The wind speed, *WS*, and direction, WD, were computed from the monthly-averaged north- and east-wind components.

The wind flows on average south-westwards (from GS to ZS). However, the average speed of the wind flow across and along the sill did not show a pronounced seasonal pattern (Fig. 3.18).

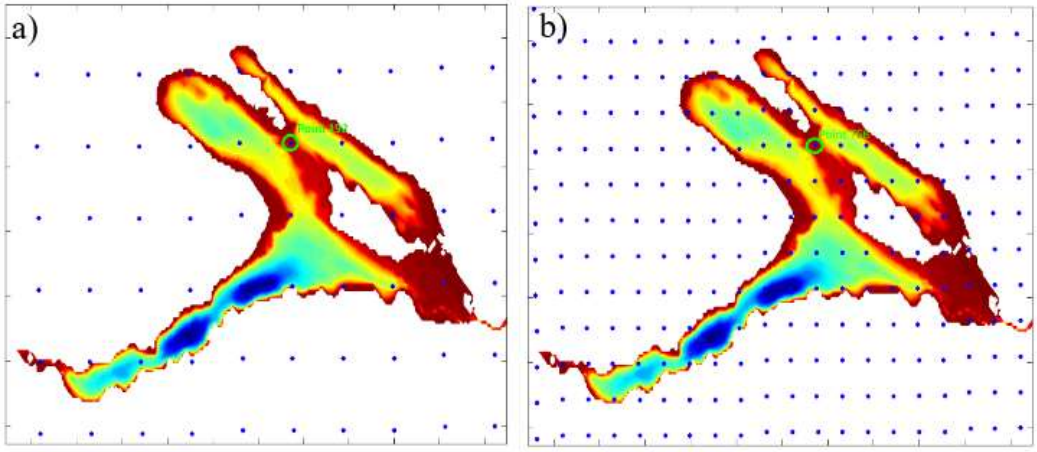

Figure 3.17: Selected points closest to $Trans_{M\text{-}R}$ of the wind field a) with a 2.2 km (station 192) and b) 1.1 km) resolution (station 766).

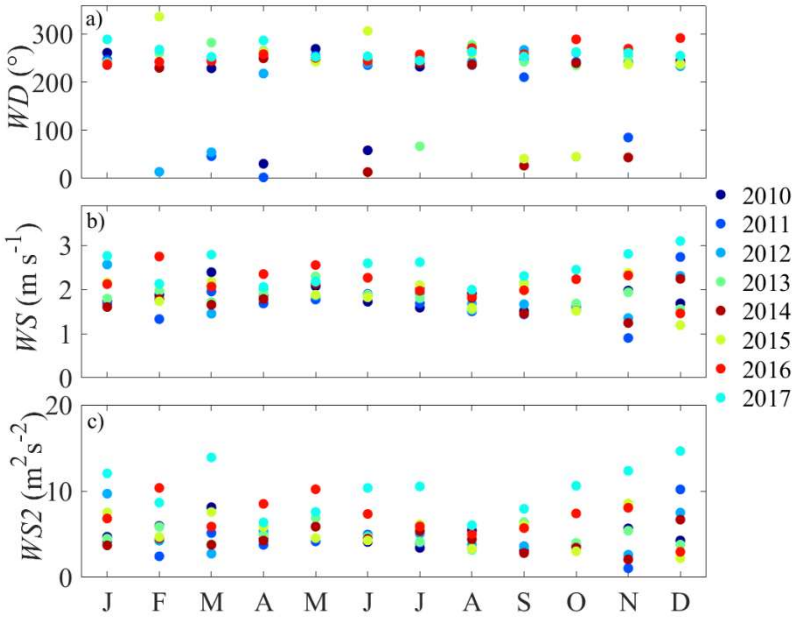

Figure 3.18: Seasonal pattern of monthly-averaged wind at the grid point of the COSMO windfield closest to $Trans_{M\text{-}R}$ (station 192 and 766). Note that the wind direction *WD* is expressed relative to the north direction and WS2 represents the wind speed squared, which is proportional to the wind forcing at the lake surface.

3E. Statistical anlysises

Linear regression analysis was applied to investigate potential links between V_{exc}, WL_S, A_S, v_s, $MLD_{SI,}$ WS (Fig. 3.4). The analysis was performed using multi-annual averages (January 2010 to December 2017) of monthly-mean data from considering two different data sets: a) considering the ice free season April to December and (b) considering all month.

Table 3.4: Results from the regression analyses of the seasonal change in multi-annual averages of monthly mean values considering the ice free season April to December. The variables included in this analysis are the multi-annual averages (years 2010-2017) of monthly-mean properties water exchange $V_{exc,m}$, water level $WL_{S.m}$, area of the cross-section above along $Trans_{M\text{-}R}$ the sill $A_{S,m}$, current speed across $Trans_S$, $v_{s,m}$, mixed layer depth at the station M_{SI} $MLD_{SI,m}$, and wind speed close to the sill WS_m.

		r	R^2	p-value
$WL_{S,m}$	$V_{exc,m}$	0.93	0.86	<0.001
$A_{S,m}$	$V_{exc,m}$	0.93	0.86	<0.001
$v_{S,m}$	$V_{exc,m}$	0.99	0.98	<0.001
$MLD_{SI,m}$	$V_{exc,m}$	-0.83	0.69	0.01
$WL_{S,m}$	$v_{S,m}$	0.87	0.77	<0.001
$MLD_{SI,m}$	$v_{S,m}$	-0.82	0.68	0.01
$WL_{S,m}$	$A_{S,m}$	-0.77	0.60	0.01
$MLD_{SI.m}$	$WL_{S,m}$	-0.77	0.60	0.01
$MLD_{SI,m}$	$A_{S,m}$	1.00	1.00	<0.001
WS_m	$V_{exc,m}$	0.24	0.06	0.54
WS_m	$v_{S,m}$	0.32	0.10	0.40

Table 3.5: Results from the regression analyses of the seasonal change in multi-annual averages of monthly mean values considering all months. The variables included in this analysis are the multi-annual averages (years 2010-2017) of monthly-mean properties water exchange $V_{exc,m}$, water level $WL_{S,m}$, area of the cross-section above along $Trans_{M\text{-}R}$ the sill $A_{S,m}$, current speed across $Trans_S$, $v_{s,m}$, mixed layer depth at the station M_{SI} $MLD_{SI,m}$, and wind speed close to the sill WS_m.

		r	R^2	p-value
$WL_{S,m}$	$V_{exc,m}$	0.95	0.91	<0.001
$A_{S,m}$	$V_{exc,m}$	0.95	0.91	<0.001
$v_{S,m}$	$V_{exc,m}$	0.99	0.98	<0.001
$MLD_{SI,m}$	$V_{exc,m}$	-0.56	0.31	0.06
$WL_{S,m}$	$v_{S,m}$	0.92	0.84	<0.001
$MLD_{SI,m}$	$v_{S,m}$	-0.50	0.25	0.10
$WL_{S,m}$	$A_{S,m}$	-0.52	0.27	0.08
$MLD_{SI.m}$	$WL_{S,m}$	-0.52	0.27	0.08
$MLD_{SI,m}$	$A_{S,m}$	1.00	1.00	<0.001
WS_m	$V_{exc,m}$	0.00	0.00	0.99
WS_m	$v_{S,m}$	0.04	0.00	0.89

Linear regression analysis was applied to investigate potential links between V_{exc} and v_s above and below the MLD_S and other properties relevant for water exchange at the sill (WL_S, A_S, MLD_S, WS). The analysis was performed using multi-annual averages (January 2010 to December 2017) of monthly-mean data considering the ice free season April to December.

Table 3.6: Linear regression analysis of the seasonal change V_{exc} and v_S above and below the mixed layer depth along $Trans_{M\text{-}R}$, MLD_S, as function of water level and mixed layer depth at M_{SI}, MLD_{SI}. Analyses are based on multi-annual average monthly-mean data and consider only the ice-free season from April to December.

		r	R^2	p-value
$WL_{S,m}$	$V_{exc,ML,m}$	0.17	0.03	0.67
$MLD_{SI,m}$	$V_{exc,ML,m}$	0.28	0.08	0.47
$WL_{S,m}$	$V_{exc,B.m}$	0.92	0.85	<0.001
$MLD_{SI,m}$	$V_{exc,B,m}$	-0.92	0.84	<0.001
$WL_{S,m}$	$v_{S,ML,m}$	0.88	0.77	<0.001
$MLD_{SI,m}$	$v_{S,ML,m}$	-0.87	0.76	<0.001
$WL_{S,m}$	$v_{S,B,m}$	0.90	0.81	<0.001
$MLD_{SI,m}$	$v_{S,B,m}$	-0.92	0.84	<0.001

Climate warming induced changes in monthly mean current speed across the sill ($\Delta v_{S,}$ $\Delta v_{S,ML}$, $\Delta v_{S,B}$) and in water exchange (ΔV_{exc}, $\Delta V_{exc,ML}$, $\Delta V_{exc,B}$) were compared to changes in monthly *MLD* at the station M_{SI} (ΔMLD_{SI}) using linear regression analysis (Tab. 3.7). The change of a property indicated by Δ is the monthly mean difference between the value of this property in scenario T4 minus its value in scenario T0. The regression analyses only consider the ice-free season from April to December.

Table 3.7: Results on from a linear regression analysis comparing the impact of climate warming on water exchange and on exchange velocity with the corresponding change in mixed layer depth at the deepest station on the sill (ΔMLD_{SI}) Analyses are based on monthly-mean data. Δ indicates the difference between the monthly mean value in scenario T4 minus its value in scenario T0. The linear regression considered only the ice-free season from April to December

		r	R^2	p-value
ΔMLD_{SI}	$\Delta Vexc$	-0.46	0.21	0.21
ΔMLD_{SI}	$\Delta V_{exc,ML}$	0.59	0.35	0.09
ΔMLD_{SI}	$\Delta Vexc_{,B}$	-0.82	0.67	0.01
ΔMLD_{SI}	Δv_S	-0.51	0.26	0.16
ΔMLD_{SI}	$\Delta v_{S,ML}$	-0.60	0.36	0.09
ΔMLD_{SI}	$\Delta v_{S,B}$	-0.87	0.76	<.0.001

3F. Currents in the open water at M_{GS} and M_{ZS} and at the sill

The vertical and seasonal pattern of the simulated currents at the sill were compared with the simulated currents at the stations M_{GS} and M_{ZS}. The vertical profiles of current speed in M_{GS}, M_{ZS} and M_{SI}, and the across speed component at M_{SI} were averaged monthly and between the years 2010 - 2017. The profiles were then compared in the months July and December, as representative of stratified and fully-mixed water column (Fig. 3.19a-d).

Additionally, we vertically averaged the monthly-mean current speeds at M_{GS}, M_{ZS} and M_{SI}, and the across speed component at M_{SI} to compare the seasonal pattern in the open water of Gnadensee and Zellersee and at the deepest station on the sill. The currents speeds were averaged from the water surface to the maximum water depth at the deepest station of the sill.

The vertical current velocity components at M_{GS} and M_{ZS} were compared in three different periods of the year 2010, as representative of the different thermal conditions in the lake: in April (establishment of stratification), in July (stable stratification) and in November (fully-mixed water column). For each month, 10 days were shown in the figures 3.20 and 3.21.

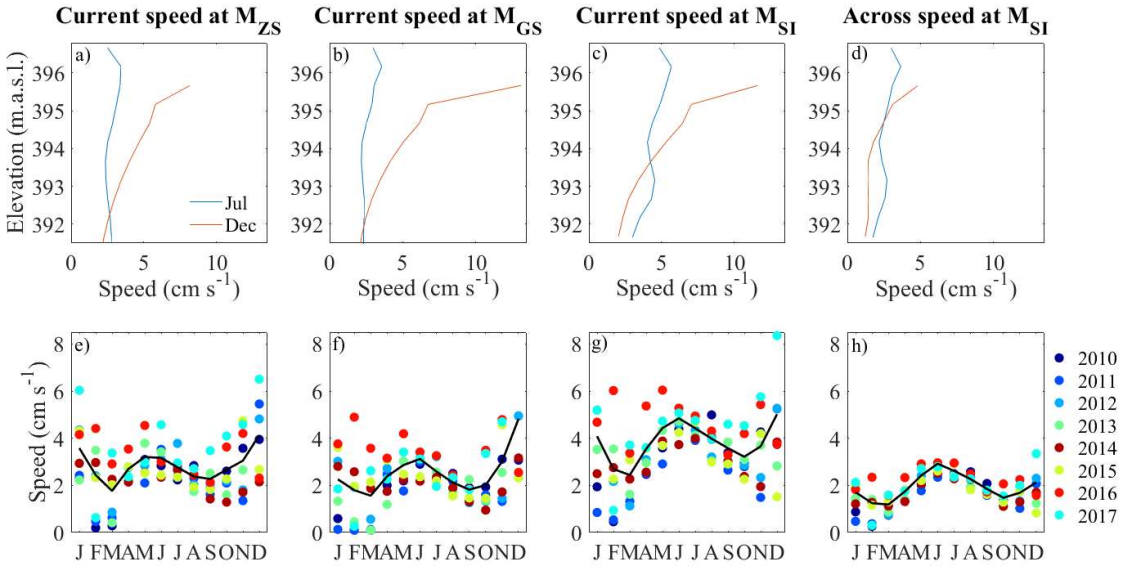

Figure 3.19: Vertical profiles and seasonal changes of mean currents in the open water of Gnadensee and Zellersee and at the deepest station of the sill. Profiles are multi-annual averages (2010-2017) of monthly mean current profiles for July and December at station a) M_{GS}, b) M_{ZS} and c) M_{SI}. In addition, similarly constructed profiles of the speed of the current across the sill at the deepest station of the sill are depict in d). The symbols in e-h show the monthly mean vertically averaged current speed at e) M_{GS}, f) M_{ZS} and g) M_{SI} and h) of the speed across the sill at M_{SI}. The vertical profiles and the vertical averages extend over the elevation range from the deepest point of the sill to the water surface. The multi-annual averages consider only the depth range available in all years, i.e. from the surface down to the multi-annual minimum of the monthly mean Ds. The black line connects the multi-annual average of the monthly values (years 2010 – 2017).

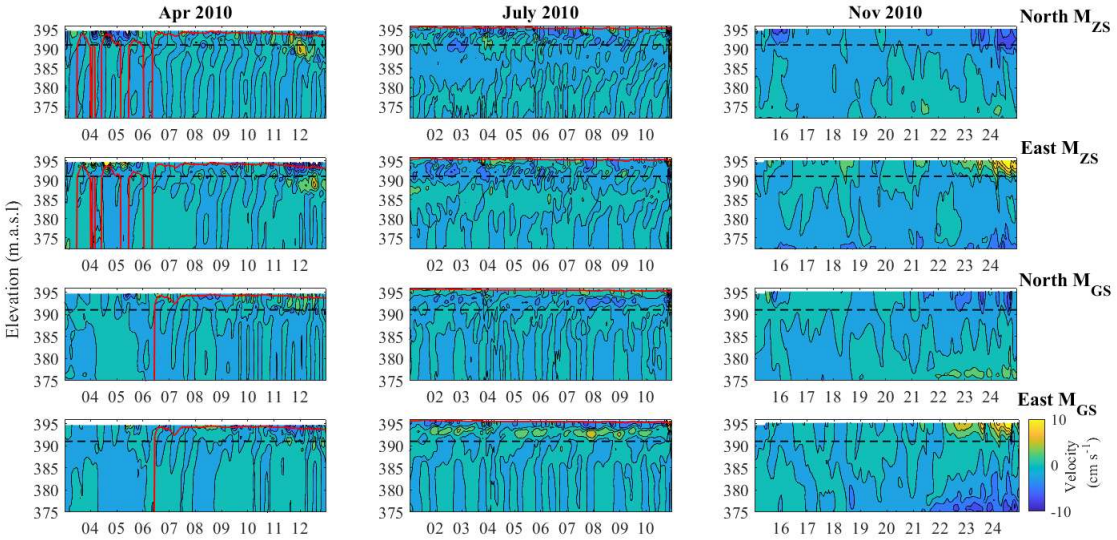

Figure 3.20: Currents in M_{GS} and M_{ZS}. The north and east components of the current velocity at M_{GS} and M_{ZS} were compared for the year 2010 in April (establishment of stratification), in July (stable stratification) and in November (fully-mixed water column). The mixed layer depth at M_{GS} and M_{ZS} is indicated by a red line, whereas the dashed line refers to the minimum elevation of $Trans_{M\text{-}R}$.

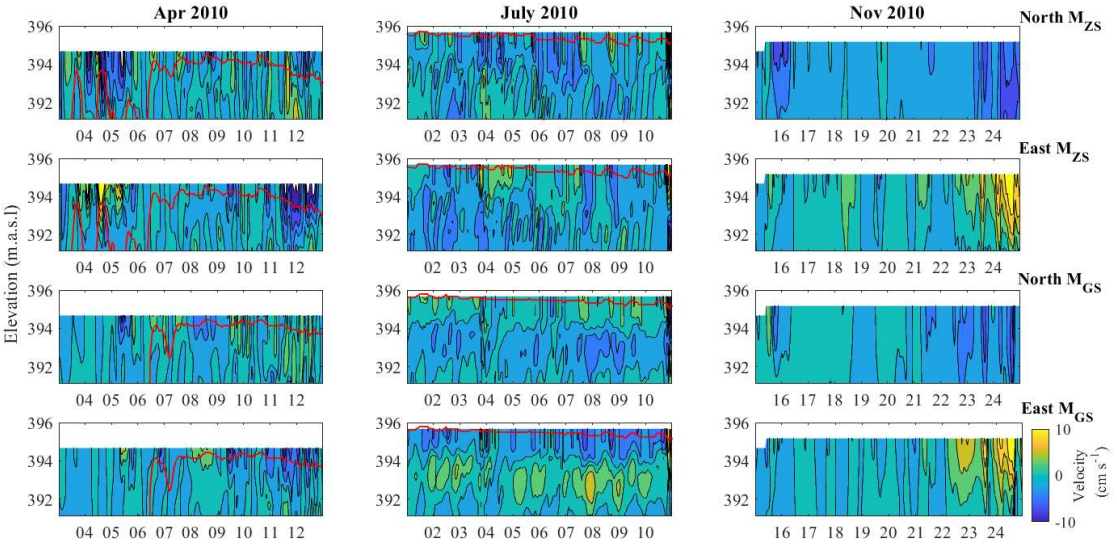

Figure 3.21: Currents at M_{GS} and M_{ZS} from the surface down to the minimum elevation of $Trans_{M\text{-}R}$. The north and east components of the current velocity at M_{GS} and M_{ZS} were compared for the year 2010 in April (establishment of stratification), in July (stable stratification) and in November (fully-mixed water column). The mixed layer depth at M_{GS} and M_{ZS} is indicated by a red line.

3G. Sensitivity analysis

A sensitivity analysis was conducted to investigate the seasonal change of V_{exc} and v_s to relative to the seasonal change in water level by applying a scenario in which the outflow was adjusted to provide a constant water level in LLC with all other conditions being the same as in scenario T0. The year 2010 was used as reference for the analysis. The scenario considered a constant water level from April to December (IO_A).

The response of the system to the scenarios was analyzed at the sill comparing the monthly-mean water exchange (V_{exc}) and mean current speed (v_S) with the reference scenario T0, and at the stations M_{GS} and M_{ZS} comparing the monthly- and vertically-averaged current speed (v_{GZ} and v_{ZS}) of IO_A with T0.

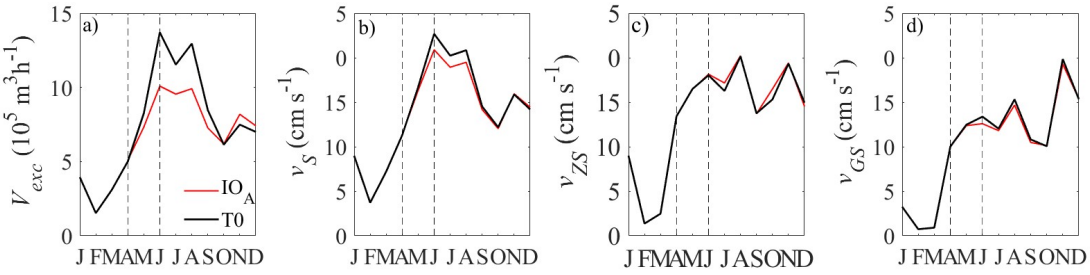

Figure 3.22: Results of the sensitivity analysis for the year 2010 at the sill and at the stations M_{GS} and M_{ZS}. The reference scenario was T0 (black line). The scenario with constant water level starting in April was called IO_A. The response of the system to the scenarios was analyzed at the sill comparing the monthly-mean water exchange (V_{exc}) and mean current speed (v_S) with the reference scenario, and at the stations M_{GS} and M_{ZS} comparing the monthly- and vertically-averaged current speed (v_{GZ} and v_{ZS}) of IO_A with T0.

3H. Ice cover in the water level scenarios

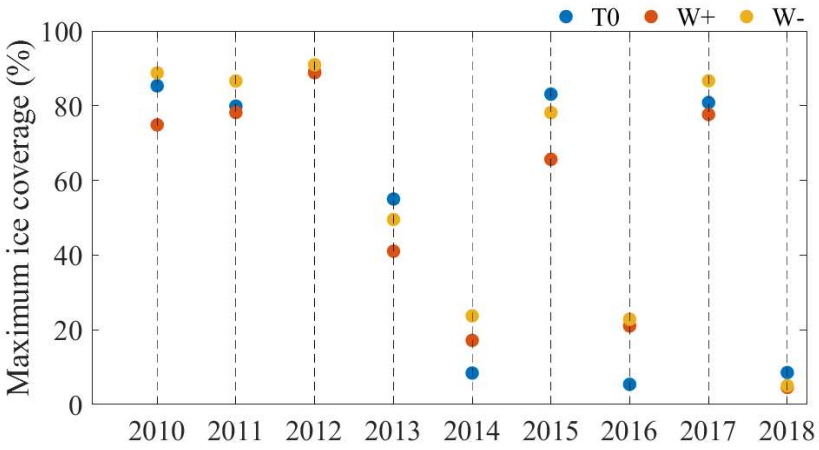

Figure 3.23: Maximum ice coverage of the lake surface during each winter in the scenarios T0, W+ and W- between 2010 and 2018.

3I. Seasonal water level scenarios

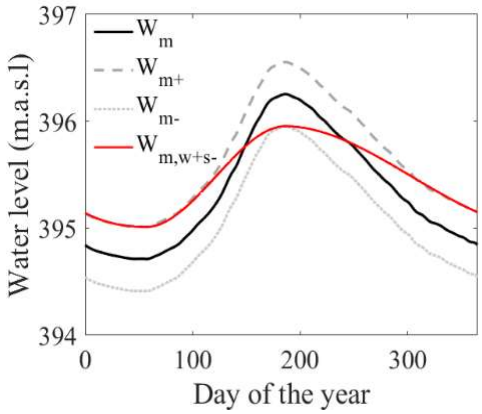

Figure 3.24: Seasonal water level scenarios. W_m represents the mean seasonal course of water level over the last 200 years which was measured in LLC, whereas $W_{m,w+s-}$ represents a 30 cm higher water level during the winter months and a 0.3 m lower water level during summer. The water level scenario W_{m+} considers a constant increase of 0.3 m with respect to W_m over the year, while W_{m-} a decrease of 0.3 m.

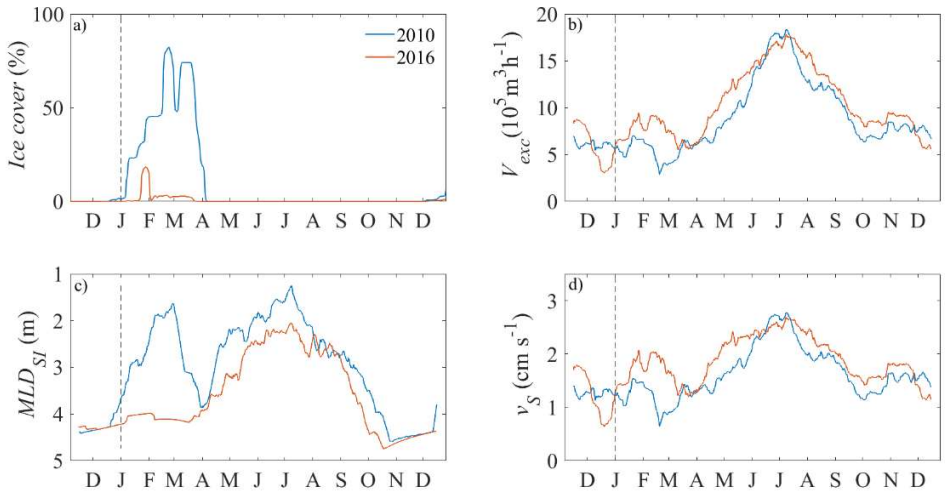

Figure 3.25: Seasonal course of water exchange V_{exc}, exchange velocity v_s and additional parameters for the scenario W_m. Seasonal pattern of a) percentage of lake surface covered by ice cover, b) water exchange V_{exc}, c) mixed layer depth at M_{SI}, MLD_S, and d) exchange velocity across the sill v_s. Simulation results are provided for the year 2010 (blue), which was characterized by abundant ice cover, and for the year 2016 (red) which was characterized by little ice cover.

3J. Tracer experiments

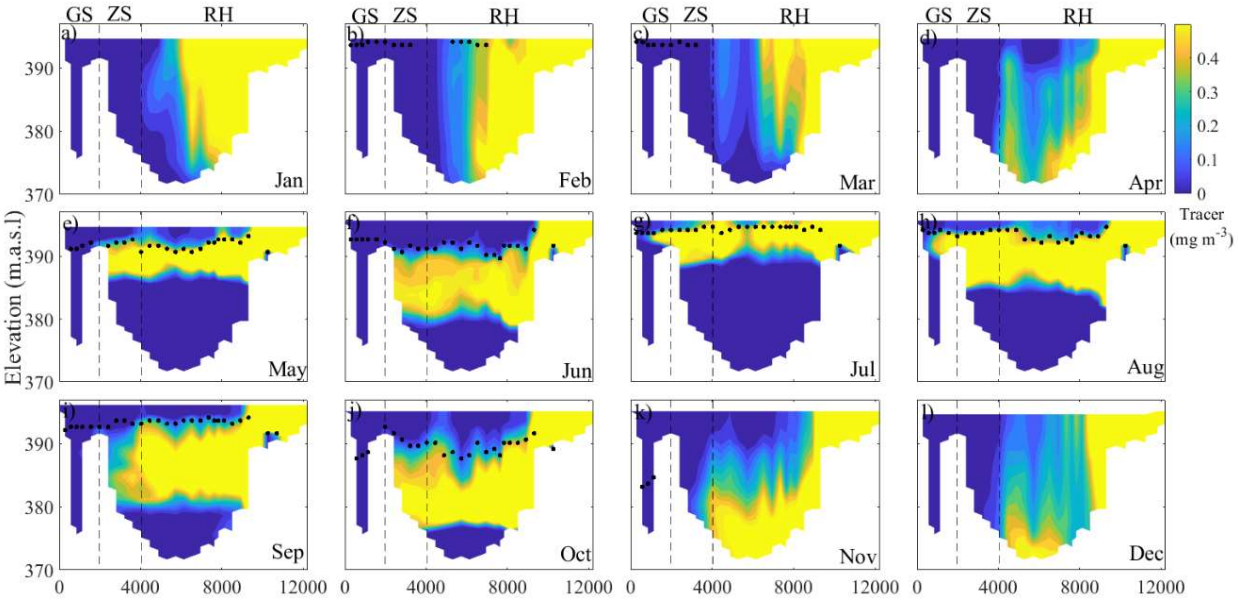

Figure 3.26: Spreading of the tracer along $Trans_{I\text{-}G}$ for the reference scenario in 2010. Panel a) to l) show the distribution of the tracer concentration 2 days after the beginning of the tracer experiments, which was re-started at the 1st day of each month. The black dots indicate the $MLH_{I\text{-}G}$. The dashed lines delimit the three sub-basins.

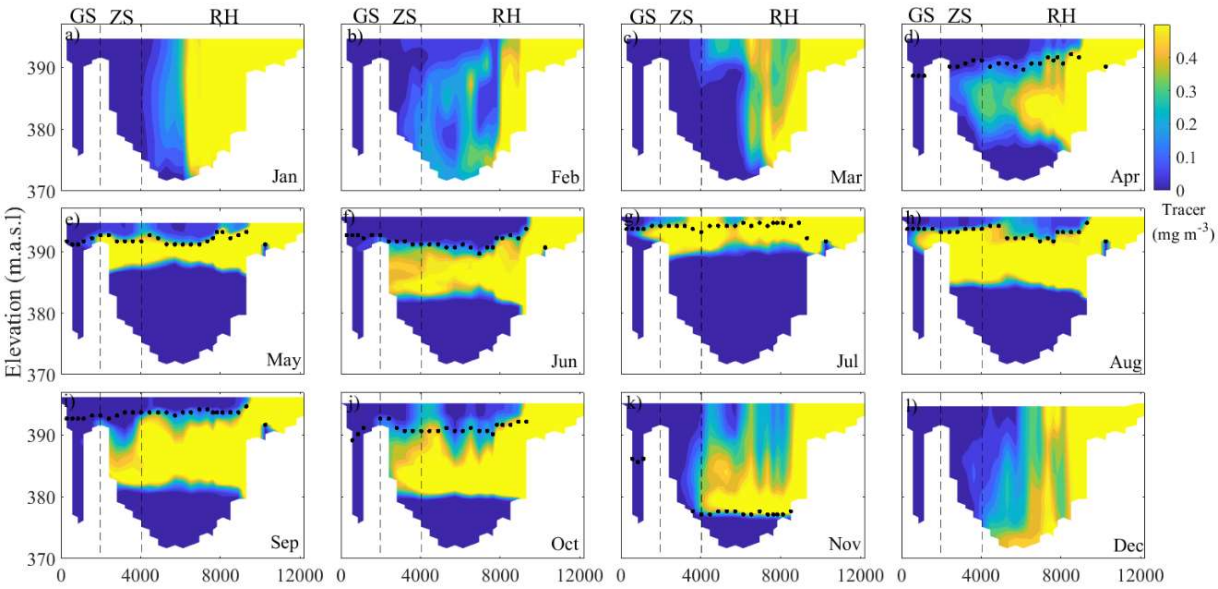

Figure 3.27: Spreading of the tracer along $Trans_{I\text{-}G}$ for the scenario T4 in 2010. Panel a) to l) show the distribution of the tracer concentration 2 days after the beginning of the tracer experiments, which was re-started at the 1st day of each month. The black dots indicate the $MLH_{I\text{-}G}$. The dashed lines delimit the three sub-basins.

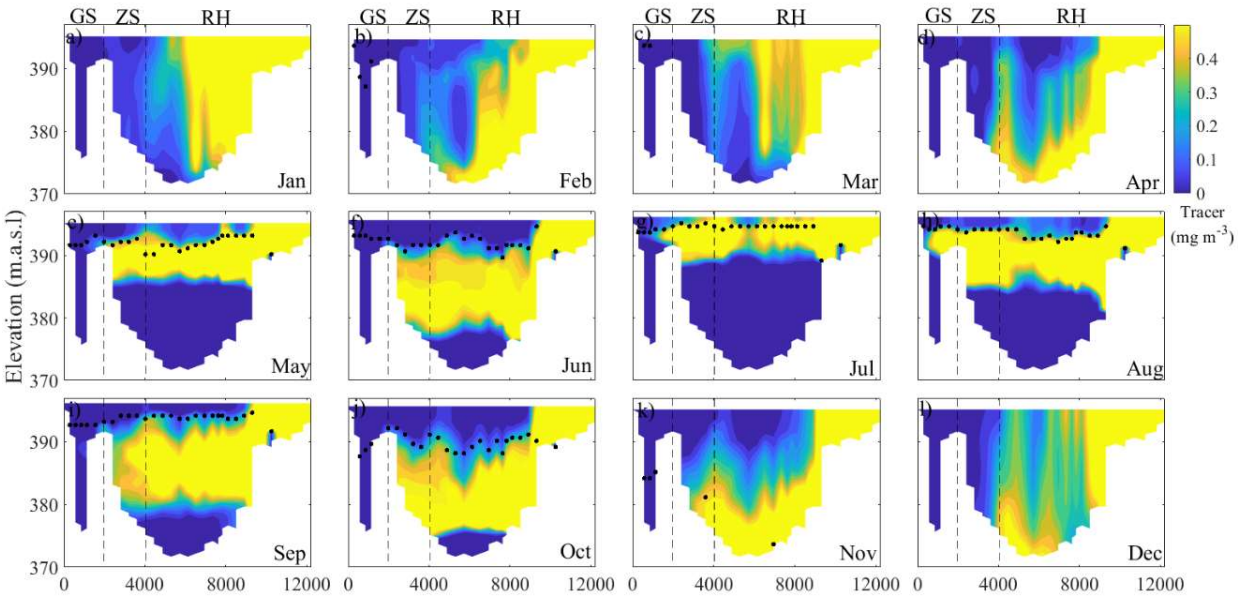

Figure 3.28: Spreading of the tracer along $Trans_{I\text{-}G}$ for the scenario W+ in 2010. Panel a) to l) show the distribution of the tracer concentration 2 days after the beginning of the tracer experiments, which was re-started at the 1st day of each month. The black dots indicate the $MLH_{I\text{-}G}$. The dashed lines delimit the three sub-basins.

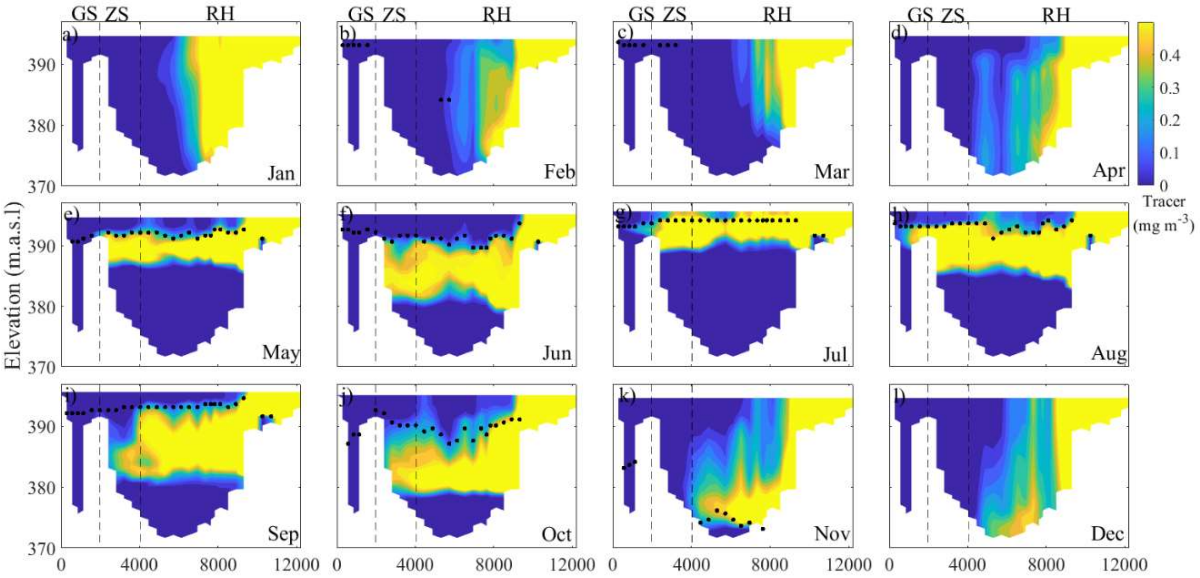

Figure 3.29: Spreading of the tracer along $Trans_{I\text{-}G}$ for the scenario W- in 2010. Panel a) to l) show the distribution of the tracer concentration 2 days after the beginning of the tracer experiments, which was re-started at the 1st day of each month. The black dots indicate the $MLH_{I\text{-}G}$. The dashed lines delimit the three sub-basins.

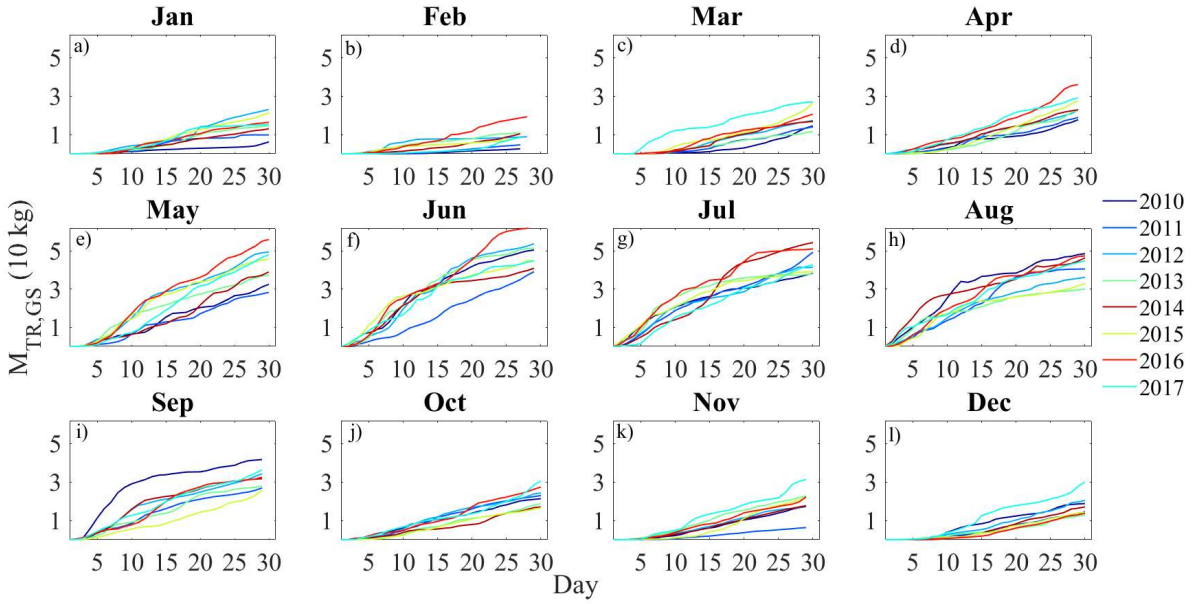

Figure 3.30: Time series of the tracer mass in GS ($M_{TR,GS}$) for each month and for all years.

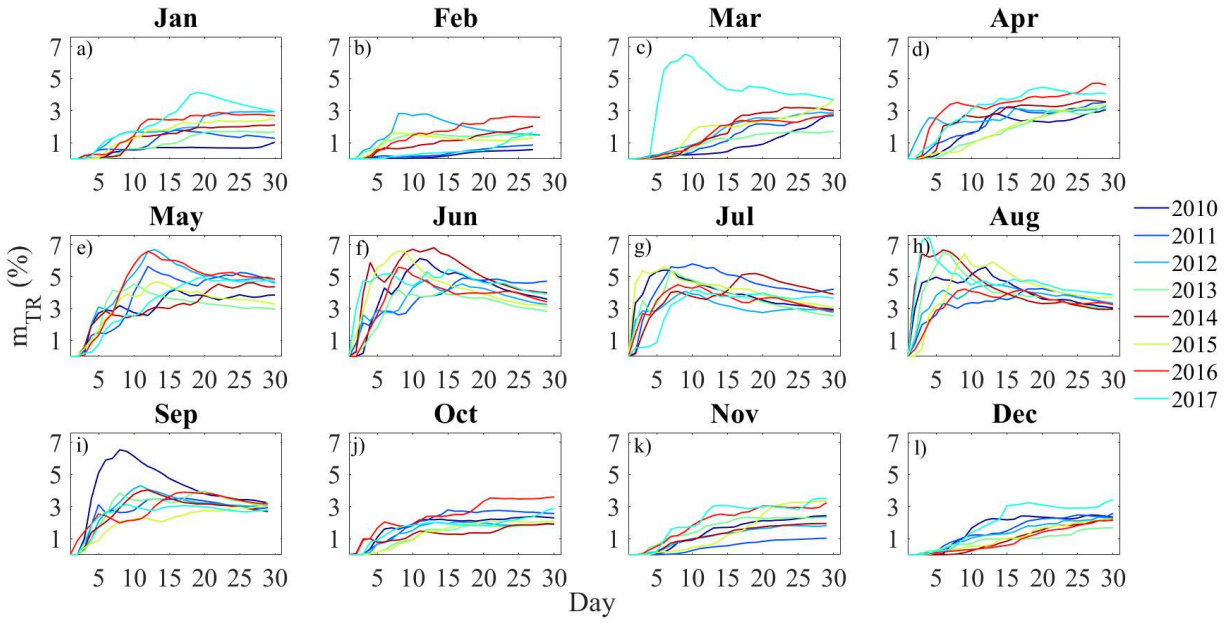

Figure 3.31: Time series of the fraction of the tracer mass in GS ($M_{TR,GS}$) divided by the mass of tracer introduced in the lake (M_{TR}), i.e. m_{TR} for each month and for all years.

4

Modelling phytoplankton spatiotemporal variability in a morphologically complex lake

I. Caramatti & F. Peeters

(in prep.)

Abstract

Lakes with substantial horizontal variability in hydrodynamic and water quality require a three-dimensional analysis to accurate simulate their spatiotemporal heterogeneous conditions. Here, we applied the three-dimensional hydrodynamic and ecological model AEM3D to simulate water quality and phytoplankton community in the morphologically complex lake Lower Lake Constance (LLC, Germany). LLC is subdivided into three basins (Gnadensee, Zeller See and Rheinsee) which differ in depth, hydrodynamic conditions, and winter ice cover. Measured data reflect moreover a system with large spatiotemporal biogeochemical variability. The goal of the study was to demonstrate that this temporal and spatial heterogeneity can be adequately simulated with a 3-D numerical model. Results indicated that model successfully captured the heterogeneity of the system, simulating well the nutrient and phytoplankton dynamics in the three sub-basins. The simulated dissolved oxygen dynamics compared well with the monthly field measurements in all the three basins. Consistent with observations, the model simulates more severe anoxic conditions in the deep water of Gnadensee than in the other basins although Gnadensee is the shallowest of the three basins. The model simulated well also the nutrient dynamics at the lake surface, whereas the nutrient exchange with sediment during summer stratification was not fully described by the model, especially in the basin of Gnadensee. In agreement with field data the simulated chlorophyll-a concentration was larger in Gnadensee and Zeller See than in Rheinsee. The typical phytoplankton seasonal succession in the lake was well reproduced, even when including time periods with ice cover. Lastly, the model succeeded in simulating the presence of a deep chlorophyll maximum (DCM) caused by Cyanobacteria in Gnadensee. In agreement with data, the simulated DCM

occurred only in Gnadensee but not in the other basins of LLC. These results indicate that 3D hydrodynamic water quality models can be successfully applied to describe the temporal and spatial heterogeneity of nutrient and phytoplankton dynamics in complex lake systems consisting of several sub-basins separated by shallow sills as e.g. between Gnadensee and Zellersee.

4.1 Introduction

Lake ecology is the result of complex interactions between lake hydrodynamic, lake hydrology, stream intrusion, nutrient loads, meteorology, sediment processes and lake morphology (Missaghi & Hondzo, 2010). The substantial heterogeneity of these factors within individual lakes, e.g. between littoral and pelagic zones, between surface and deep water, and between sub-basins of lakes with complex morphometry, favors the establishment of spatial gradient also within the phytoplankton community. Ability to describe the distribution and dynamics of phytoplankton communities and identification of its drivers can benefit the understanding of lakes ecosystem and its response to environmental stressors, e.g. climate and trophic changes.

Lake ecological models can be useful tools to simulate heterogeneous phytoplankton distribution in lakes and to compensate for the difficulties to extensively and intensively measure spatial conditions in the field (Fragoso Jr et al., 2008). Ecological models based on one-dimensional (1D) hydrodynamic processes provide a realistic representation of stratification and mixing processes in lakes (Hamilton et al., 1997; Imberger & Patterson, 1989; Imberger, 1998) and they are suitable to investigate vertical heterogeneous conditions. The dynamic and vertical heterogeneity of phytoplankton have been well captured by 1D models, such as DYRESM-CAEDYM (Imberger et al., 1978; Rinke et al., 2009; Trolle et al., 2008), PROTECH (Elliott et al., 2001; Elliott et al., 2020; Lewis et al., 2002) or other models (Kerimoglu et al., 2013, 2014; Walsby, 2005; Walsby et al., 2006)

However, in lakes characterized by significant differences between pelagic and shore zones or by complex morphometry the assumption of horizontally homogenous conditions underlying vertical 1D models may be too restrictive as it does not allow to consider impact of lake morphometry and associated lateral heterogeneous hydrodynamic conditions on ecological processes (Fragoso Jr et al., 2008; Kalff, 2002; Missaghi & Hondzo, 2010; Wetzel, 2001). Hence,

horizontal two-dimensional (2D) models or three-dimensional (3D) models can then offer more insight in the factors determining local water quality (Fragoso Jr et al., 2008). Whereas 2D models may be suitable in shallow lakes or in lakes during unstratified conditions, 3D models are required in stratified deep or medium-deep lakes allowing for a comprehensive representation of heterogeneous conditions both vertically and horizontally.

The rapidly advancing computing power and improvements in 3D models in the past two decades have provided more opportunities to use them for annual and multi-annual simulations of water quality in lakes and reservoirs. 3D-models are fundamental tools to describe the individual morphological features of morphologically complex lakes, e.g. bays and sills, and to capture their significant hydrodynamic gradients and water quality heterogeneity. Fragoso Jr. et al. (2008) used a phytoplankton model coupled with a horizontal 2D hydrodynamic model to simulate the spatial heterogeneity of phytoplankton in the large subtropical shallow Lake Mangueira (South Brazil), whereas a 3D approach was used for example in the western basin of Lake Erie (Ontario, Jiang et al., 2015), in Lake Pusiano (Italy, Carraro et al., 2012), in the reservoir Alqueva (Portugal, Lindim et al., 2011) and in Lake Constance (Germany, Rinke et al., 2009). However, only few studies exist that attempt to provide a characterization of the spatiotemporal variability of hydrodynamic and ecology in morphologically complex lakes (Leon et al., 2011; Missaghi & Hondzo, 2010) and they are limited to the example of Great Lakes (Lake Minnetonka and Lake Erie).

In this study, we applied the three-dimensional hydrodynamic and ecological model AEM3D to simulate water quality and phytoplankton community in the three sub-basins of the morphologically complex lake Lower Lake Constance (LLC, Germany). Whereas the phytoplankton community in the upper basin of Lake Constance, Upper Lake Constance (ULC), has been already many times simulated, both with a 1D (Frassl et al., 2014; Kerimoglu et al., 2013, 2014; Peeters et al., 2007; Rinke et al., 2009; Rinke et al., 2010; Tilzer & Goldman, 1978) and 3D approach (Lang et al., 2010; Rinke et al., 2009), this study is the first investigation that provides a characterization of the phytoplankton community and nutrient distribution in Lower Lake Constance. The complex morphometry of the lake causes difference in hydrodynamic conditions and thermal structure among its three sub-basins leading also to large spatial gradients in water quality and phytoplankton community. Here, we assess if the simulation of the spatiotemporal dynamics of water quality and phytoplankton community can compare well with the field data in all the three sub-basins in two years with different meteorological forcing, flow dynamics and ice cover formation.

4.2 Methods

4.2.1 Study site

Lake Constance (9°18'E, 47°39'N) is a large Alpine lake of glacial origin that consists of two main parts, Upper Lake Constance (ULC) and downstream Lower Lake Constance (LLC), which is connected to ULC via river Seerhein (Fig. 4.1).

LLC can be nowadays considered as a mesotrophic system after being recovered from a severe eutrophication phase. Indeed, the total phosphorous concentration during winter mixing declined from more than 100 μg total phosphorous (TP) L^{-1} in the 70's to 14 μg TP L^{-1} in 2016 (Vonlanthen et al., 2012), resulting now in a more pronounced phosphorous depletion in the epilimnion during summer (IGKB, 2018). The lake's trophic history was similar also for ULC and for many other lakes in Central Europe (Vonlanthen et al., 2012).

LLC is subdivided into three sub-basins that differ in maximum water depth, thermal structure, ice formation and coverage (Caramatti et al. 2020), phytoplankton community and nutrient distributions (IGKB, 2018). Rheinsee (RS) is the deepest sub-basin (46 m) and it is directly under the influence the main inflow, the river Seerhein, entering in the eastern part. Its water quality results thus to be closely linked to the one of Upper Lake Constance (IGKB, 2018). The northern part of RH is connected to Zeller See (ZS), which has a maximum depth of 24 m. In the most western part of ZS enters river Radolfzeller Aach, which is the second largest inflow of LLC and it is richer in nutrients with respect to the river Seerhein (Suppl. 4A; IGKB, 2018). The third sub-basin, Gnadensee (GS), has a maximum water depth of 20 m, no significant inflows and it is connected to ZS via a narrow sill of about 2.5 km length, 6.4 m mean and 13.8 m maximum depth (with respect to the reference water level 395 m.a.s.l). The horizontal exchange between GS and ZS of water, as well as of nutrients and organisms, is limited and characterized by a seasonal pattern: high exchange in summer, when water level and currents speeds are highest, and low in winter. When ice cover develops in the lake or in the basin of GS, the exchange is further limited (Chapter 3).

Temperature data and previous studies about LLC (Caramatti et al. 2020, Chapter 3) showed that stable stratification of the water column is established in the lake during summer and complete mixing occurs during autumn overturn. Full ice cover develops during winter (January – March) almost each year in Gnadensee, but only rarely in Zeller See and Rheinsee. During ice-covered periods, inverse stratification typically develops in the uppermost 1-2 m of the water column (Caramatti et al., 2020). In the years herby considered, thin ice cover developed only in Gnadensee

between January and February 2016, whereas in year 2017 the model simulated up to 87% of the lake surface covered by ice (Caramatti et al. 2020). Additionally, in summer 2016 the lake water level was extraordinarily high with a maximum annual water level of 397.03 m.a.s.l, while in the year 2017 more than one meter smaller (395.93 m.a.s.l).

Together with the seasonal and inter-annual variability of the abiotic factors, the water quality and the phytoplankton community show significant spatiotemporal variability among the three lake sub-basins (IGKB, 2018).

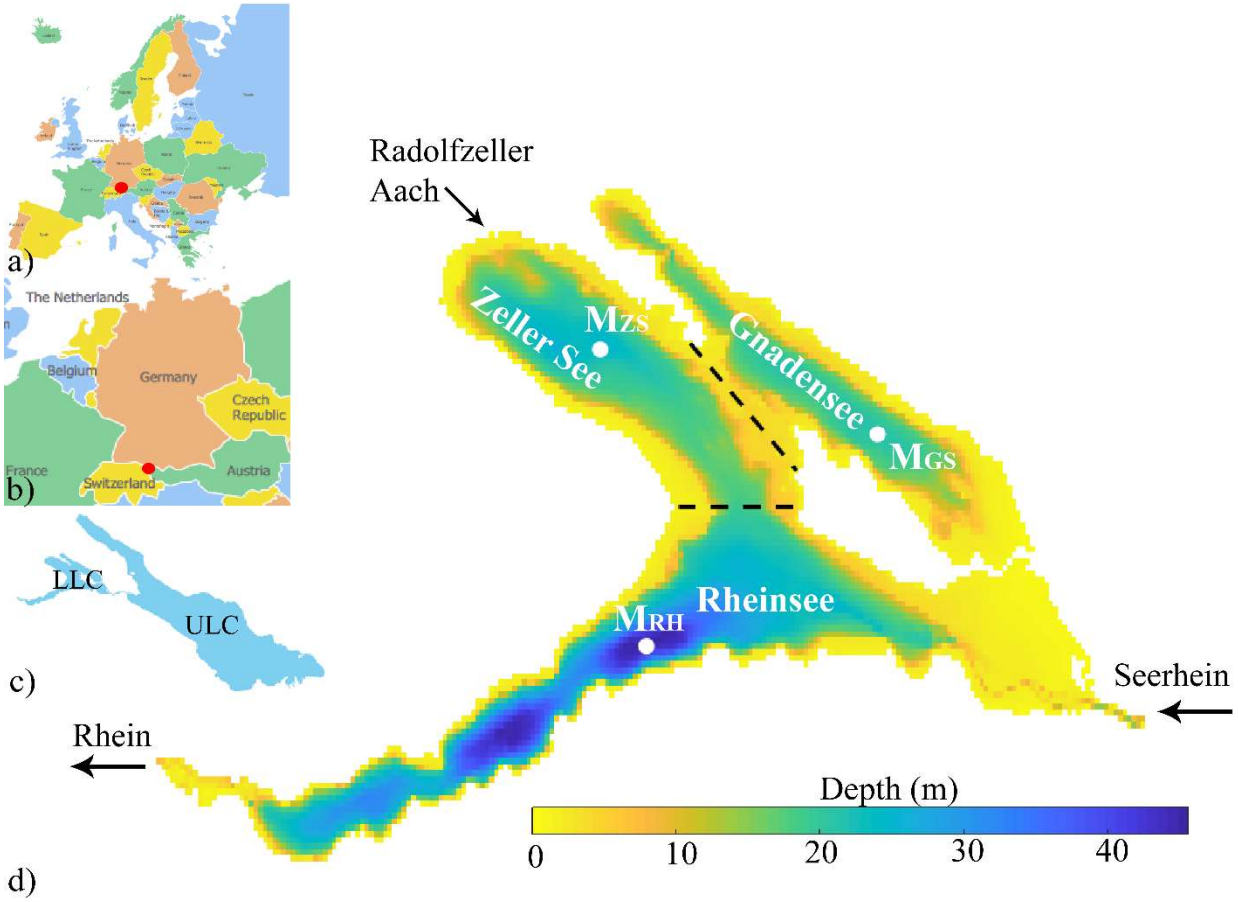

Figure 4.1: Schematic sketch of the study site. a) and b) Location of Lake Constance in Europe. c) Lake Constance subdivided in Upper Lake Constance (ULC) and Lower Lake Constance (LLC). d) Bathymetry of Lower Lake Constance indicating the sub-basins Gnadensee, Zeller See and Rheinsee and the main inflows (Seerhein and Radolfzeller Aach) and the outflow (Rhein). The subdivision of the lake in sub-basins is represented by a black dashed line. Monitoring stations M_{GS} (Gnadensee), M_{ZS} (Zeller See) and M_{RH} (Rheinsee) are indicated by white circles. The depth is measured relative to a water level of 395 m.a.s.l..

4.2.2 Model description

We used the three dimensional model Hydrodynamic-Aquatic Ecosystem Model (AEM3D, Hodges & Dallimore, 2018) to simulate the inter-basin spatial variability of the phytoplankton community in LLC.

The model consists in a hydrodynamic module with the possibility to dynamically couple it with an ice module and an ecological one. Whereas the hydrodynamic and ice modules have been already set up and successfully employed to simulate the thermal structure, ice cover formation in LLC and inter-basin water exchange (Caramatti et al., 2020; Chapter 3), the water quality in LLC has been never simulated before.

The ecological module of AEM3D reworded the old CAEDYM code (Hodges & Dallimore, 2016). While the science is essentially the same and was amply described in previous studies (Gal et al. 2009; Hipsey et al. 2006; Robson and Hamilton 2004; Romero 2004; Spillman et al. 2008; Hodges and Dallimore 2018), the new module has been designed to allow the user more flexibility when configuring a simulation.

The ecological module of AEM3D allows to simulate up to 112 state variables describing nutrients and biogeochemistry in surface waters. For this application the model was used to simulate the nitrogen (N), phosphorous (P), carbon (C) and dissolved oxygen (DO) cycles in the lake, along with the phytoplankton dynamics. Each simulated variable is subject to advection, mixing and boundary forces by the hydrodynamic module.

The DO dynamics include atmospheric exchange, sediment oxygen demand, organic matter mineralization and nitrification demand, photosynthetic oxygen production and respiratory oxygen consumption. The sediment oxygen demand, f_{O_2}, is represented by a fixed oxygen flux across the sediment-water interface, S_{SOD}, limited by a function of the water temperature, f_{SOD}^{T}, and one of dissolved oxygen levels in the overlying water, f_{SOD}^{DO}:

$$f_{O_2}(T, DO, O) = S_{SOD} \cdot f_{SOD}^{T} \cdot f_{SOD}^{DO}$$

$$f_{SOD}^{T} = \theta_{SOD}^{T-20} \quad \text{and} \quad f_{SOD}^{DO} = \frac{DO}{DO + K_{SOD}^{DO}}$$

where θ_{SOD} is the temperature multiplier and K_{SOD}^{DO} is a half saturation constant for the sediment oxygen demand.

The nutrient cycle encompasses both the inorganic and organic, and dissolved and particulate forms of C, N and P along the degradation pathway of particulate organic matter (POM)

to dissolved organic matter (DOM) and then to inorganic matter (DIM). The nitrogen cycle additionally includes the processes of denitrification, nitrification and nitrogen gas fixation. The model maintains mass balance of C, N and P between the water column and a single sediment layer. The sediment fluxes of dissolved inorganic and organic nutrients are function of temperature and oxygen concentration of the overlying water, as in the formula above.

Phytoplankton description

Phytoplankton dynamics account for variations in growth rates, losses to respiration, excretion and mortality, settling and resuspension. For each phytoplankton group *a*, the growth rate, ${\mu_g}_a$, is determined by a maximum potential growth rate at 20 °C (${\mu_{g,max}}_a$), modified by a temperature response function, ${f_a}^T$, and the minimum value of limitation by light, P and N:

$$ {\mu_g}_a = {\mu_{g,max}}_a {f_a}^T \min[f(P)_a, f(N)_a, f(I)_a] $$

The temperature response function is defined so that the maximum productivity occurs at a temperature $T_{OPT,a}$, so that $\frac{d{f_a}^T}{dT}\left(T_{OPT,a}\right) = 0$ and:

$$ {f_a}^T = \begin{cases} 0 & T > T_{MAX,a} \\ {\theta_a}^{T-20} & T < T_{STD,a} \\ {\theta_a}^{T-20} + {\theta_a}^{k(T-z)} + y & T_{STD,a} < T < T_{MAX,a} \end{cases} $$

where $T_{MAX,a}$ and $T_{STD,a}$ are respectively the maximum and standard temperature for phytoplankton growth, θ_a is the temperature multiplier for phytoplankton growth. *k*, *z*, and *y* are unknown variables whose value is determined by solving the equation numerically. The temperature dependence function refers by default to the reference temperature of 20°C, but it can be modified defining the parameter $T_{REF,a}$ (for more details see Hipsey et al., 2006).

The light limitation of phytoplankton, $f(I)_a$ was described by the model of Webb et al. (1974):

$$ f(I)_a = 1 - exp\left(\frac{-I}{I_k}\right) $$

where I is the incoming irradiance and I_k is the light half saturation constant.

The nutrient limitation for phytoplankton growth is based on the Droop model (Droop 1974), allowing for the phytoplankton to have variable internal nutrient concentrations. Under this model, the limitation function takes the form in the case of nitrogen:

$$f(N)_a = \frac{AIN_{max_a}}{AIN_{max_a} - AIN_{min_a}}\left[1 - \frac{AIN_{min_a}}{AIN_a}\right]$$

whereAIN_a is the internal nitrogen concentration, AIN_{max_a} and AIN_{min_a} are user-defined bounds for the internal nitrogen concentrations. Using this method, the internal nitrogen store for each phytoplankton group is specified as a unique state variable and is subjected to advection and settling with the phytoplankton.

Losses to respiration, natural mortality and excretion scale with temperature according to the Arrhenius law. Losses to sedimentation were represented by a constant settling rate (w_s) specific to each phytoplankton group. Note that the phytoplankton biomass is represented in terms of chlorophyll-a (μg Chl-a L^{-1}) and the conversion between Carbon and Chlorophyll units is indicated as Ycc.

4.2.3 Model set-up

The set-up of the hydrodynamic and ice module has been extensively described in Caramatti et al. 2020 and Chapter 3 In this study, the simulation time covered a shorter time period with respect to the previous studies (7 September 2015 to 31 December 2017) due to the computational limitation introduced by the coupling of the ecological module.

We chose to use three phytoplankton groups to simulate the major groups known to be important in the lake. The Diatoms group represents early-blooming diatom taxa (e.g. *Stephanodiscus neoastraea, Stephanodiscus alpinus, Asterionella Formosa, Fragilaria crotonensis*), while the Cryptophyceae group represent taxa growing later in the season (e.g. *Rhodomonas lacustris, Rhodomonas lens*). The Cyanobacteria group was instead defined to represent mainly the larger taxa that are associated with warm and stable waters, mainly *Planktothrix Rubescens* in the years considered *(*IGKB 2018). The parameter regulating phytoplankton dynamics are presented in Tab. 4.1.

Initial conditions of phytoplankton concentration and nutrients were prescribed at a depth 0, 5, 10, 15, 20, 22 in M_{ZS}, 0, 5, 10, 15, 19 in M_{GS} and 0, 5, 10, 15, 20, 30, 40, 45 in M_{RH}. The external load of nutrients and phytoplankton was prescribed monthly in correspondence of the two main inflows (Seerhein and Radolfzeller Aach) (Figs. 4.1 and 4.9). The DO concentration of the tributaries was instead supposed to be 100% of the oxygen concentration at saturation, derived as a function of the inflowing water temperature (Weiss 1970). Due to the absence of field measurements at the inflows, the input load of each phytoplankton group was equal to 0.05 μg Chla L^{-1}.

4.2.4 Water quality data

The field data to set-up and calibrate the ecological module in LLC were provided by the Landesanstalt für Umwelt Baden-Württemberg (Germany, LUBW). Monthly data of nutrients and DO concentration, as well as of water temperature, were collected in the three monitoring stations at a depth 0, 5, 10, 15, 20, 22 in M_{ZS}, 0, 5, 10, 15, 19 in M_{GS} and 0, 5, 10, 15, 20, 30, 40, 45 in M_{RH}. Additionally, monthly vertically-integrated samples of chlorophyll-a concentration and phytoplankton biomass were collected along the entire water column in M_{GS} and in the uppermost 20 m in the other stations M_{ZS} and M_{RH}.

The concentration of each phytoplankton group expressed in μg Chla L^{-1} was computed as a fraction of the total measured Chlorophyll-a concentration, where the fraction was defined as ratio between the biovolume of the specific group and the sum of the biovolumes of all the phytoplankton groups.

Vertical profiles of phytoplankton concentrations were measured in M_{GS} and M_{ZS} using a spectrofluorometric probe (BBE FluoroProbe, Moldaenke). The FluoroProbe (FP) differentiates up to four ‘spectral groups’ of phytoplankton. The device is indeed provided with spectral fingerprints for Diatoms, Cyanobacteria, Cryptophyceae and Chlorophyceae. For a detailed description of FP, see Beutler et al. (2002).

The nutrient loads associated with the inflows Seerhein and Radolfzeller Aach were provided by the LUBW (Fig. 4.9).

4.2.5 Model calibration

The model was calibrated over the entire simulated period based on visual comparisons between model output and field measurements. The parameter regulating DO and nutrient dynamics were tuned, especially to better simulate the progressive oxygen depletion and the nutrient release from sediment during summer stratification. The files containing the variables describing DO and nutrients dynamics can be found in the Suppl. 4B. Phytoplankton parameters were instead assigned to the three groups according to values reported in the literature or to other modelling studies (Tab 4.1). Some parameters were tuned to improve the fit model-data (bold values in Tab. 4.1).

The C:Chl-a ratio (Ycc) for the phytoplankton groups was made similar to values suggested in the literature (Cloern et al., 1995; Lorenzen, 1968) and used in other modelling studies (Copetti et al., 2006; Griffin et al., 2001; Rinke et al., 2010, Carraro et al., 2010) (Tab. 4.1). The value of Ycc was set equal to 40 mgC mgChl-a^{-1} for all three phytoplankton groups.

Phytoplankton growth rate is referenced against a water temperature of 20°C under full light conditions. We used a growth rate of 1.1 d^{-1} for Diatoms, 0.5 d^{-1} for Cryptophyceae and 1.3 d^{-1} for Cyanobacteria. The growth rate varies indeed from as low as 0.25 d^{-1} in the case of very large Dinoflagellates such as Ceratium (Eppley et al., 1984), to above 2 d^{-1} in the case of very small green algae and Diatoms (Bruggeman, 2011). Diatoms such as Trichomes (filaments) or Aulacoseira have growth rates 1.2 to 1.4 d^{-1}, whereas smaller species (e.g. Asterionella formosa) may have still faster growth rates (e.g. Asterionella Formosa 1.7 d^{-1}; Bernard & Rémond, 2012). The growth rate of the simulated phytoplankton groups was tuned in the literature range to limit the growth of Diatoms, the most abundant group in the lake, and allows the growth of the other groups. The values used are also similar to the ones used in other modelling studies (Carraro et al., 2010; Leon et al., 2011).

The cardinal temperatures defining the temperature responses of the groups were derived from studies about phytoplankton traits. The temperature multiplier for growth mainly determines the steepness of response below T_{STD} and above T_{OPT} and typical values are between 1.05 and 1.09. Cyanobacteria tends to have higher T_{OPT} values compared with other phytoplankton. Paerl (2014) reported indeed the optimum temperature for Cyanobacteria to be higher than 25°C, whereas for Diatoms 17–22°C. We defined a T_{OPT} for Cyanobacteria of 28°C, for Diatoms of 16°C and for Cryptophyceae of 21°C. Also T_{MAX} is usually higher for Cyanobacteria with respect to the other phytoplankton groups (Reynolds, 1997; Joehnk et al., 2008; Paerl, 2014) and it was then set to

35°C. The maximum temperature for Diatoms was instead defined equal to 30°C according to the study of Zhang et al. (2018) and the modelling study of Rinke et al. (2010) in ULC, whereas the maximum temperature for Cryptophyceae was set up lower than for the other groups (27°C), according to the study of Wirth et al. (2019).

We neglected light limitation at the lake surface under high incoming irradiance and choose to model the light limitation of phytoplankton growth with the model of Webb et al. (1974). The light half saturation parameter governing the phytoplankton light limitation function can be as low as 5 μmol m^{-2} s^{-1} for the case of some Diatoms that are adapted to very low light levels to higher values (150 – 200 μmol m^{-2} s^{-1}) for the case of Cyanobacteria which are commonly buoyant and well adapted to high irradiance. We used 10 μmol m^{-2} s^{-1} for Diatoms and 150 μmol m^{-2} s^{-1} for Cyanobacteria, while for Cryptophyceae intermediate values similar to other modelling studies (Griffin et al., 2001).

Frassl et al. (2014) underlined the importance of including a flexible cell stoichiometry of phytoplankton into a complex lake model for predicting spatial nutrient gradients within the lake. We used therefore the Droop model to describe the nutrient limitation for the three simulated phytoplankton groups.

K_P values are generally in the range 0.0005 to 0.010 mg L^{-1}. Low values refer to some of the larger phytoplankton species that are remarkably good competitors for scarce resources or are able to use physiological adaptations such as buoyancy or motility to overcome problems of spatial accessibility to nutrients. These species include genera such as Peridinium, Ceratium and several cyanobacteria. By contrast other fast-growing, single-celled genera (e.g. Chlorella) or filamentous genera (e.g. Aulacoseira) do not have the same capacity for efficiently utilizing low levels of available nutrients and are quickly superseded by the slower-growing species. This capacity for less efficient resource utilization is reflected in higher levels of K_P. The values of K_P were therefore prescribed equal to 0.009 mg L^{-1} for Cryptophyceae, 0.005 mg L^{-1} for Diatoms, 0.003 mg L^{-1} for Cyanobacteria

K_N is about 0.015 mg L^{-1}, with the exception of the N-fixing Cyanobacteria for those K_N can be fixed closed to zero. Since P-Rubescens is well known for not being capable of fixing atmospheric nitrogen dissolved in the water column, all phytoplankton groups have similar values of K_N in the range 0.02 – 0.03 mg L^{-1} (0.03 mg L^{-1} Cryptophyceae, 0.02 mg L^{-1} Diatoms, 0.015 mg L^{-1} Cyanobacteria).

Approximations for internal nutrient concentrations can be based on Redfield ratios (106C:16N:1P) and if it is assumed that Ycc is 40, then:

$$1 \text{ mg Chl}a \equiv 40 \text{ mg C} \equiv \frac{40 \circ 1 \circ 32}{106 \circ 12} \text{ mg P} = 1.00 \text{ mg P}$$

Then a mid-range value for internal nitrogen (IN) is 1.0 mg P (mgChl*a*)$^{-1}$ and the minimum (IPmin) and maximum (IPmax) should be side of this value. Similarly, internal nitrogen (IN) has a mid-range value of 7.0 mgN (mgChl*a*)$^{-1}$ and INmin and INmax should be side of this value. IPmin and INmin values are often around 0.4 mgP (mg Chl*a*)$^{-1}$ and 3 mgN (mg Chl*a*)$^{-1}$, respectively. IPmin and INmin were set respectively equal to 0.4 mgP (mgChl*a*)$^{-1}$ and 4 mgN (mgChl*a*)$^{-1}$ for Diatoms, 0.4 mgP (mgChl*a*)$^{-1}$ and 3.1 mgN (mgChl*a*)$^{-1}$ for Cryptophyceae, and 0.8 mgP (mgChl*a*)$^{-1}$ and 5 mgN (mgChl*a*)$^{-1}$ for Cyanobacteria, while IPmax and INmax were set respectively equal to 0.8 mgP (mgChl*a*)$^{-1}$ and 9 mgN (mgChl*a*)$^{-1}$ for Diatoms, 1.5 mgP (mgChl*a*)$^{-1}$ and 11.5 mgN (mgChl*a*)$^{-1}$ for Cryptophyceae, and 1.2 mgP (mgChl*a*)$^{-1}$ and 9 mgN (mgChl*a*)$^{-1}$ for Cyanobacteria.

Values of UPmax and UNmax, adjusting for Redfield ratios, should always exceed the growth rate. A growth rate of 1 day^{-1} gives an equivalent phosphorus uptake rate of 0.025 mgP (mgC)$^{-1}$ day^{-1} and nitrogen uptake rate of 0.176 mgN (mgC)$^{-1}$ day^{-1} equivalent to 1.3 mgP (mgChl *a*)$^{-1}$ day^{-1} and 8.8 mgN (mgChl *a*)$^{-1}$ day^{-1}, respectively. UPmax and UNmax were set respectively equal to 1.8 mgP (mgChl*a*)$^{-1}$ day^{-1} and 9.5 mgN (mgChl*a*)$^{-1}$ day^{-1} for Diatoms, 1.4 mgP (mgChl*a*)$^{-1}$ day^{-1} and 9 mgN (mgChl*a*)$^{-1}$ day^{-1} for Cryptophyceae, and 2.2 mgP (mgChl*a*)$^{-1}$ day^{-1} and 10 mgN (mgChl*a*)$^{-1}$ day^{-1} for Cyanobacteria.

Settling rates specified for each group are in comparable range to several previous modeling studies (Robson & Hamilton, 2004; Romero et al., 2004, Burger et al., 2006). For Cyanobacteria that may buoyancy to ascend in the water column, a slightly positive sedimentation rate is required in the absence of using the vertical migration model. Diatoms have instead a higher sedimentation rate because of their silica shell (Rinke et al., 2010). From Reynolds (1997) can be derived that the respiration rate is circa 10% of the maximum growth rate. The chosen values are in this order of magnitude and they were tuned to improve the fit model-data (Tab. 4.1).

Table 4.1: List of parameters in AEM3D describing the phytoplankton dynamics. For each parameter its symbol, unit and assigned value for each group are shown. The values in "bold" were adjusted to improve the fit model-observations. Values derived from literature are indicated with the capital superscript: [A]Cloern et al., 1995; [B]Lorenzen, 1968, [C]Paerl (2014), [D]Reynolds (1997), [E]Joehnk et al. (2018), [F]Zhang et al. (2018), [G]Wirth et al.

(2019). Values used in other modelling studies are indicate with the lowercase superscript: [a]Copetti et al., 2006; [b]Griffin et al., 2001; [c]Rinke et al., 2010, [d]Carraro et al., 2010, [e]Robson and Hamilton (2004), [f]Romero et al. (2004), [g]Leon et al. (2011), [h]Burger et al. (2006).

Phytoplankton	**Symbol**	**Unit**	**Diatoms**	**Cryptophyceae**	**Cyanobacteria**
Average ratio of C to Chlorophyll a	Ycc	mgC mgChl-a^{-1}	40 [A, B, c, d, e, f]	40 [A, B, b, d]	40 [A, B, f]
Maximum potential growth rate of phytoplankton	$\mu_{g,max}$	d^{-1}	**1.2**	**0.5**	**1.3**
Temperature multiplier function for phytoplankton growth	θ_T	-	1.05	1.07	1.09
Standard growth temperature	T_{STD}	°C	12	16	20 [e, h]
Optimum growth temperature	T_{OPT}	°C	16	21	28 [C, e, h]
Maximum growth temperature	T_{MAX}	°C	30 [F, d]	27 [G]	35 [D, E, e, h]
Reference growth temperature	T_{REF}	°C	20 [d]	17	20 [h]
Light half saturation constant for algal limitation	I_K	μmol m^{-2} s^{-1}	10	20	150
Half saturation constant for phosphorous uptake	K_P	mgP L^{-1}	0.005	0.009	0.003
Half saturation constant for nitrogen uptake	K_N	mgN L^{-1}	0.02	0.03	0.015
Minimum internal phosphorous concentration	IPmin	mgP mgChl-a^{-1}	0.4	0.4	0.8
Maximum internal phosphorous concentration	IPmax	mgP mgChl-a^{-1}	0.8	1.5	1.2
Maximum rate of phosphorous uptake	UPmax	mgP mgChl-a^{-1} d^{-1}	1.8	1.4	2.2
Minimum internal nitrogen concentration	INmin	mgN mgChl-a^{-1}	4	3.1	5
Maximum internal nitrogen concentration	INmax	mgN mgChl-a^{-1}	9	11.5	9
Maximum rate of nitrogen uptake	UNmax	mgN mgChl-a^{-1} d^{-1}	9.5	9	10
Respiration coefficient	k_r	d^{-1}	**0.15**	**0.15**	**0.08**
Temperature multiplier for respiration	θ_r	-	1.06	1.08	1.09
Constant settling velocity	w_s	m s^{-1}	-0.35E-5	-0.2E-5	0.5E-05 [f, h]

4.2.6 Analysis of the simulation results

The accuracy of the simulation in terms of water quality and phytoplankton concentration with respect to the field measurements was evaluated in the stations M_{GS}, M_{ZS} and M_{RH} using the Normalized Root Mean Square Error (NRMSE). For dissolved oxygen (DO), phosphate (PO4), ammonium (NH4) and nitrate (NO3) we computed the NRMSE at each depth (d_j) of the available field records:

$$NRMSE(d_j) = \frac{\left[\frac{1}{N}\sum_{i=1}^{N}(x_j(t_i) - y_j(t_i))^2\right]^{1/2}}{M_{x,j} - m_{x,j}}$$

where x_j and y_j are the measured and simulated quantity at the date t_i and depth d_j, respectively. N represents the number of records, and $M_{x,j}$ and $m_{x,j}$ respectively the maximum and minimum value of the data measured at depth d_j.

For each phytoplankton group, we computed the vertically-mean average concentration along the entire water column in M_{GS} and in the uppermost 20 m in the stations M_{ZS} and M_{RH} and compared them with the respective integrated samples. The formula of the NRMSE was then:

$$NRMSE = \frac{\left[\frac{1}{N}\sum_{i=1}^{N}(x(t_i) - y(t_i))^2\right]^{1/2}}{M_x - m_x}$$

where x and j are respectively the measured and simulated vertical mean concentration at the date t_i in M_{GS}, M_{ZS} or M_{RH}. N represents the number of records and M_x m_x respectively the maximum and minimum value of the N measured data. Suppl. I provided more statistics describing the fit model-data for phytoplankton and Chlorophyll-a to facilitate the comparison with other modelling studies.

4.3 Results

4.3.1 Dissolved oxygen (DO)

Field measurements in LLC show that the water column is well oxygenated during complete mixing periods, but it undergoes a progressive oxygen depletion during summer, more significant in the deep water where anoxic conditions are established, than in the epilimnion where the oxygenation is supported by primary production (Fig. 4.2).

The model simulated well the progressive oxygen depletion at the lake bottom in all the three basins, with a NRMSE of 0.10, 0.06 and 0.04 respectively at the bottom of the stations M_{ZS}, M_{GS} and M_{RH} (Fig. 4.2a-c). The model was indeed able to simulate, in agreement with data, the establishment of anoxic conditions (DO<0.5 mg L^{-1}) in all the three stations and less severe anoxic conditions in M_{RH} than in the other stations. Indeed, whereas the concentration at the bottom of the water column in M_{ZS} and M_{GS} reached zero in both years, the minimum simulated DO concentration in M_{RH} at 45 m depth was 0.26 mg L^{-1} in the year 2016 and 1.39 mg L^{-1} in the year 2017. The model distinguished also between more severe anoxic conditions in the year 2016 than 2017. Indeed, the simulated oxygen concentration at 18 m depth and 22 m depth respectively in M_{GS} and M_{ZS} was below 0.5 mg L^{-1} for 48 and 38 consecutive days, whereas in the year 2017 for 39 and 12 consecutive days.

The model output showed that the most severe anoxic conditions occurred at the bottom of the deepest part of the lake sub-basins, whereas the coastal and shallow water zones, like the sill between Gnadensee and Zeller See, remained more oxygenated (Fig. 4.2d). However, though the basin of Gnadensee is the shallowest basin, it experienced more severe anoxic conditions than the other basins (Fig. 4.2e). Cells at the same height above the bottom were characterized by a lower minimum DO concentration in the basin of Gnadensee than in Zeller See or Rheinsee.

The greatest discrepancies between simulated and observed DO concentration were simulated in correspondence of the lake surface. In all the three stations, whereas during complete mixing periods the model-data agreement was good, during stratification the oxygenation of the mixed-layer region was instead underestimated by the model. The NRMSE at the lake surface over the simulated period were therefore above 0.4 respectively in all the three stations.

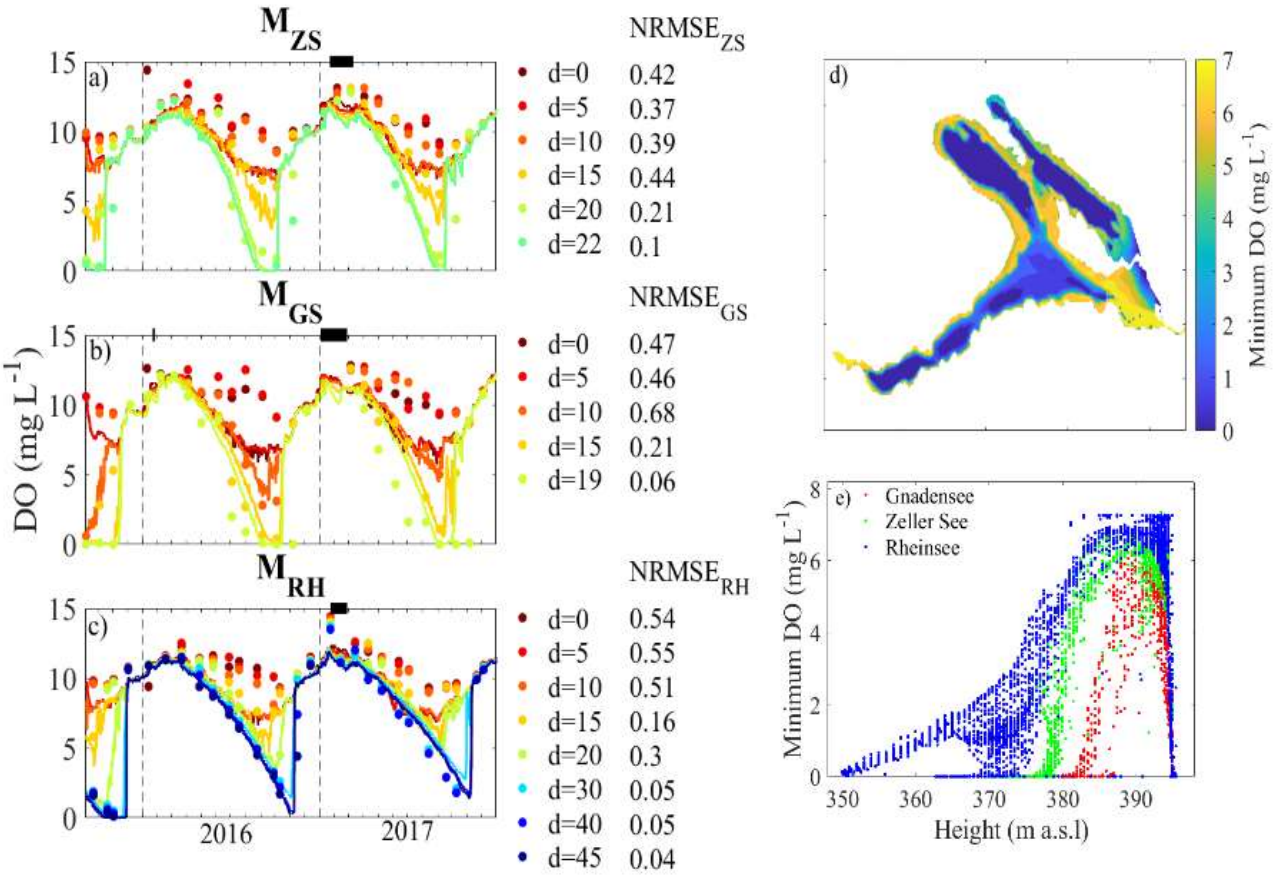

Figure 4.2: Simulated and measured dissolved oxygen concentration (DO) in Lower lake Constance. Simulated (lines) and measured (dots) DO concentration in a) M_{ZS}, b) M_{GS} and c) M_{RH} during the simulated period. The simulated concentration was compared against field measurements at different depths by means of the Normalized Root Mean Square Error (NRMSE). Simulated ice cover presence in the three stations was indicated by a black bar at the panel top. d) Simulated minimum DO at the lake bottom during the year 2016. e) Height of each grid cell at lake bottom against the corresponding simulated minimum DO concentration during the year 2016. The color-coding allows the distinction between the three lake sub-basins.

4.3.3 Nutrients

Phosphate (PO4)

Model simulated phosphate concentrations were generally in good agreements with the measured data (Fig. 4.3). Measured phosphate values show that the three sampling locations have distinct localized phosphate concentrations indicating phosphorous heterogeneity with M_{ZS}

having the largest values. Moreover, the model showed that in the upper most water in M_{ZS} the PO4 concentration seasonal variability is greater than in the other sub-basins.

Simulated eplimnic and hypolimnetic PO4 values had a moderate fit at all three sampling sites (NRMSE ≤ 0.9). However, the model underestimated the phosphorous concentration in the deep water of M_{GS}, M_{ZS} and M_{RH} during stratified conditions, resulting in a NRMSE of 0.35, 0.35 and 0.6 respectively. The model consequently did not distinguish between the greater phosphate release from sediments in the year 2016 than 2017. Field data show indeed that, in 2016, the PO4 concentration at the deep of M_{GS}, M_{ZS} and M_{RH} reached respectively 36.6 µg L^{-1}, 38.8 µg L^{-1} and 15.7 µg L^{-1}. During the year 2017, instead, the PO4 concentration was below 22.0 µg L^{-1} in all the three sub-basins.

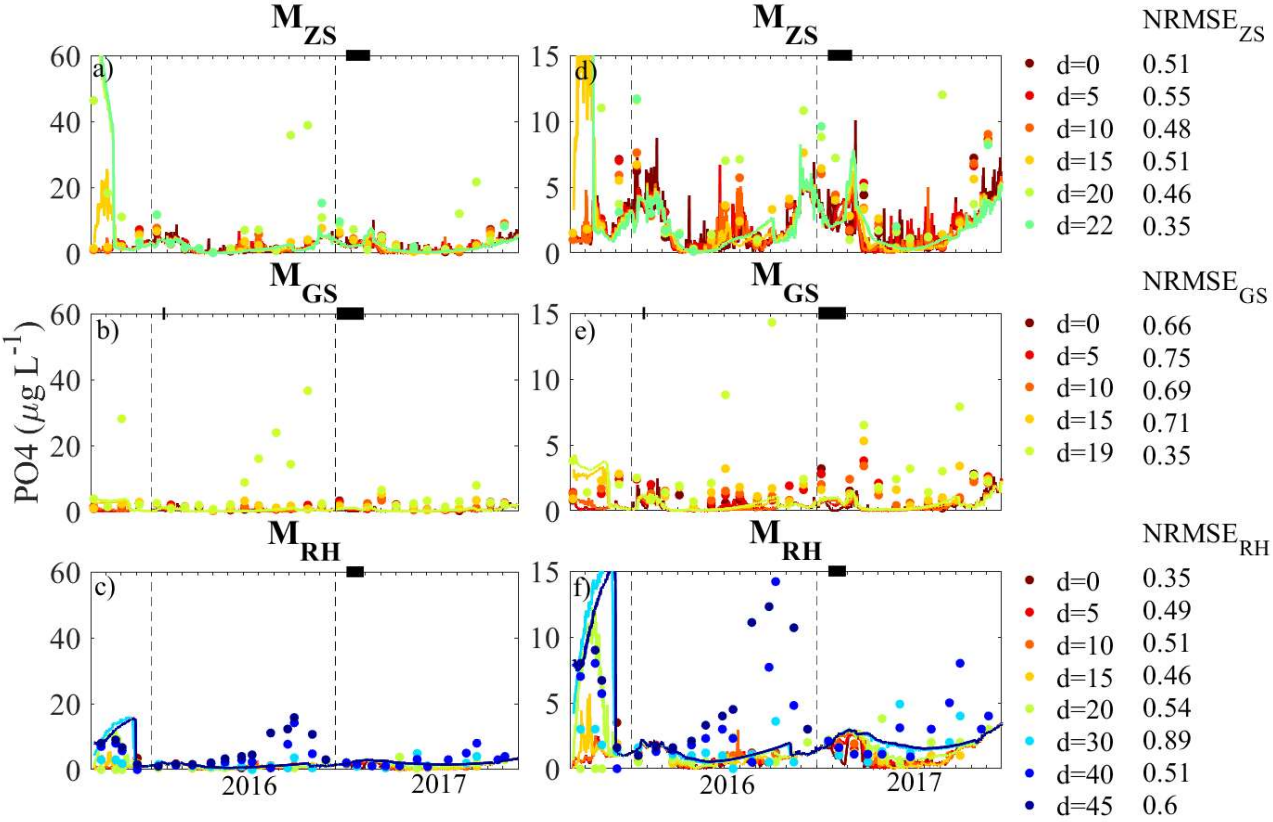

Figure 4.3: Simulated and measured phosphate concentration (PO4) in Lower lake Constance. Simulated (lines) and measured (dots) PO4 concentration in a,d) M_{ZS}, b,e) M_{GS} and c,f) M_{RH} during the simulated period. The simulated concentration was compared against field measurements at different depths by means of the Normalized Root Mean Square Error (NRMSE). Ice cover presence in the three stations was indicated by a black bar at the panel top. The right panels (d, e, f) showed the same results but with a reduced amplitude of the y-axis to better distinguish between results at different depths.

Nitrate (NO3) and ammonium (NH4)

In agreement with field records, the model showed that nitrate is the major form of inorganic nitrogen in the lake and its concentration is highest in M_{ZS} (Fig. 4.4). The typical seasonal pattern of nitrate in the lake was well simulated. The simulated NO3 concentration was indeed highest at the beginning of the year and decreased during summer to reach the minimum during autumn overturn (Fig. 4.4a-c). The model, in agreement with data, reproduced a greater inter-seasonal variability in M_{ZS} than M_{RH}, whereas in M_{GS} the simulated magnitude of the inter-seasonal variability was much smaller than the one observed in the field.

However, the model accuracy to simulate nitrate in the three monitoring stations was quite low, especially in M_{RH}, where the NRMSE was above 1 along the entire water column.

Regarding ammonium, field records show that its concentration at the bottom of the stations M_{GS} and M_{ZS} usually increase during summer stratification (Fig. 4.4d-f). The model well reproduced the increase of NH4 at the bottom of M_{ZS}, but it underestimated it in M_{GS} and overestimate it in M_{RH}. Overall, the agreement model-data was better than for nitrate. Indeed, in all the three stations the NRMSE was below 1 along the entire water column.

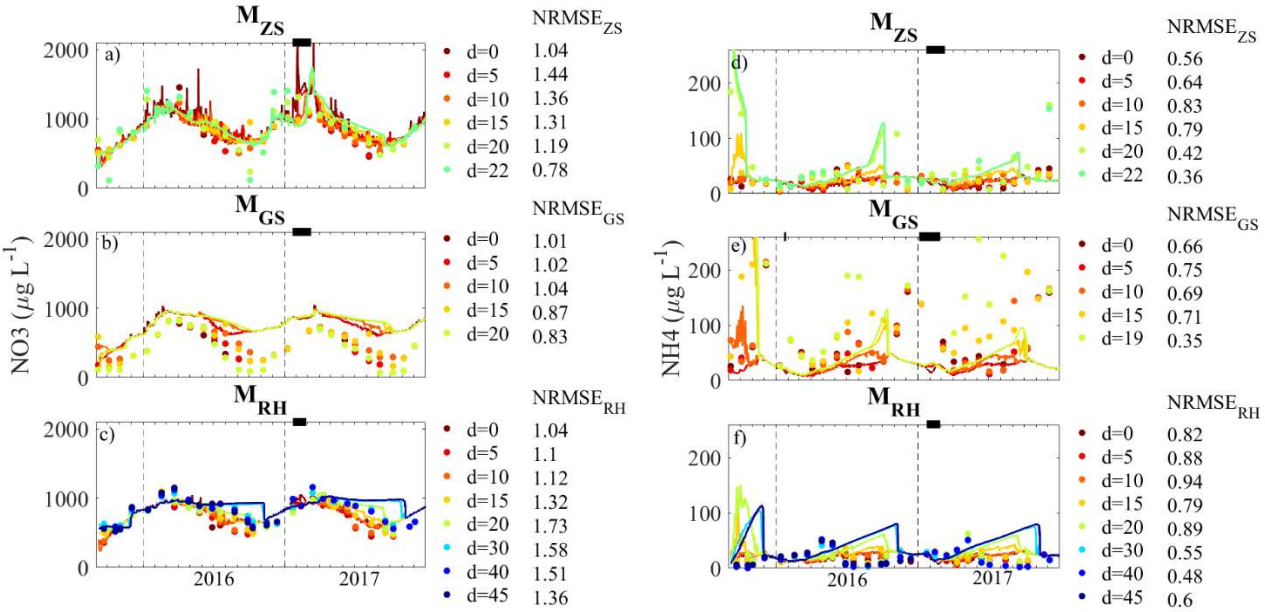

Figure 4.4: Simulated and measured nitrate (NO3) and ammonium (NH4) concentration in Lower lake Constance. Simulated (lines) and measured (dots) NO3 (left panels: a, b, c) and NH4 (right panels: d, e, f) in M_{ZS}, M_{GS} and M_{RH} during the simulated period. The simulated concentration was compared against field measurements at different depths by means of the Normalized Root Mean Square Error (NRMSE). Ice cover presence in the three stations was indicated by a black bar at the panel top.

4.3.4 Chlorophyll-a and phytoplankton community

Field data show that in all the three monitoring stations in LLC the concentration of Chlorophyll-a and phytoplankton are usually low and lowest in M_{RH} (Fig. 4.5). Accordingly, the model simulated more abundant Chlorophyll-a concentration in M_{GS} and M_{ZS} than in M_{RH} (Fig. 4.5). The mean and maximum simulated concentration over the considered period were indeed respectively 3.2 µg L^{-1} and 10.4 µg L^{-1} in M_{ZS}, 3.7 µg L^{-1} and 10.9 µg L^{-1} in M_{GS}, and 2.0 µg L^{-1} and 6.8 µg L^{-1} in M_{RH}.

The most abundant Chlorophyll-a concentration was simulated in all the three stations at the beginning of the year (both 2016 and 2017), whereas lower concentration during summer and fall, in accordance with the typical seasonal phytoplankton development in the lake. The agreement with field data was highest in the monitoring stations of M_{ZS} ($NRMSE_{ZS}$=0.21) than in the other two, where the NRMSE exceeded 0.5.

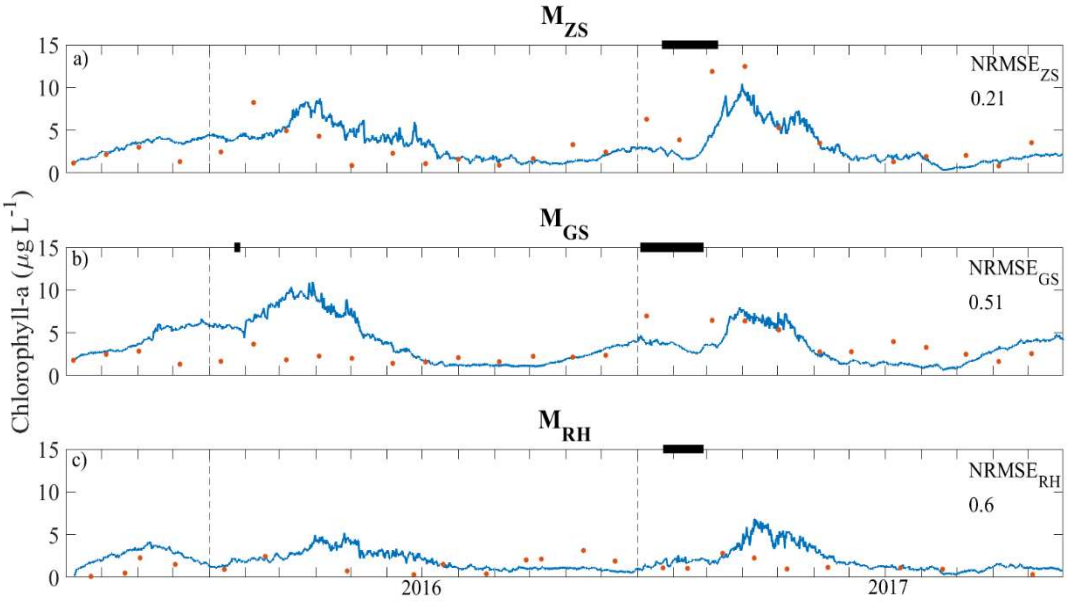

Figure 4.5: Simulated and measured Chlorophyll-a concentration in Lower lake Constance. Simulated (lines) and measured (dots) Chlorophyll-a concentration in M_{ZS}, M_{GS} and M_{RH} during the simulated period. The simulated Chlorophyll-a concentration was vertically averaged along the entire water column in M_{GS} and along the uppermost 20 m in M_{ZS} and M_{RH}. The simulated concentration was compared against field measurements by means of the Normalized Root Mean Square Error (NRMSE). Ice cover presence in the three stations was indicated by a black bar at the panel top.

Indeed, the model overestimated the Diatoms growth in late fall 2015 and winter 2016 in the basin of Gnadensee and Rheinsee (Fig. 4.6). However, the simulated Diatoms seasonal succession in M_{ZS} was in good agreement with the field data over the entire simulated period ($NRMSE_{ZS}$=0.21) and in M_{GS} and M_{RH} from summer 2016 onwards (from September 2016 $NRMSE_{GS}$=0.24 and $NRMS_{RH}$=0.56, against respectively 0.48 and 0.73 over the entire simulated period). Consistent with the typical seasonal development of phytoplankton in LLC, the model simulated the dominance of Diatoms during winter and spring.

The model succeeded in simulating the coexistence of Cryptophyceae and Diatoms during the late fall 2015 and winter 2016 and the simulation agreed well with data. The NRMSE computed until 1st July 2016 was indeed below 0.4 in all the three monitoring stations. However, Cryptophyceae disappeared in the lake during summer and did not grow again later in the season, resulting in a NRMSE over the entire simulated period only below 0.55 in all the three monitoring stations.

Consistent with observations, Cyanobacteria were simulated later in the year and their peak occurred in fall. Whereas field data show that the Cyanobacteria peak is usually greater in M_{GS} than in the other two stations, the model simulated a highest Cyanobacteria peak in M_{ZS} than in the other stations. For instance, in the year 2016, the model simulated a peak of 1.5 $\mu g\ L^{-1}$ in M_{ZS}, 0.8 $\mu g\ L^{-1}$ in M_{GS} and 0.8 $\mu g\ L^{-1}$ in M_{RH}. The timing of the simulated Cyanobacteria peak was overall earlier than the measured one in all the three stations. While the timing discrepancy between observed and simulated peak in M_{GS} was less than 1 month for the year 2016, in the other stations the peak occurred synchronous with M_{GS} leading to an anticipation of the Cyanobacteria peak of ca. 2 months in M_{RH} and more than 3 months in M_{ZS}. In the year 2017, the timing of the Cyanobacteria peak in M_{GS} was in agreement with field records, whereas no peak was observed but simulated in the other stations.

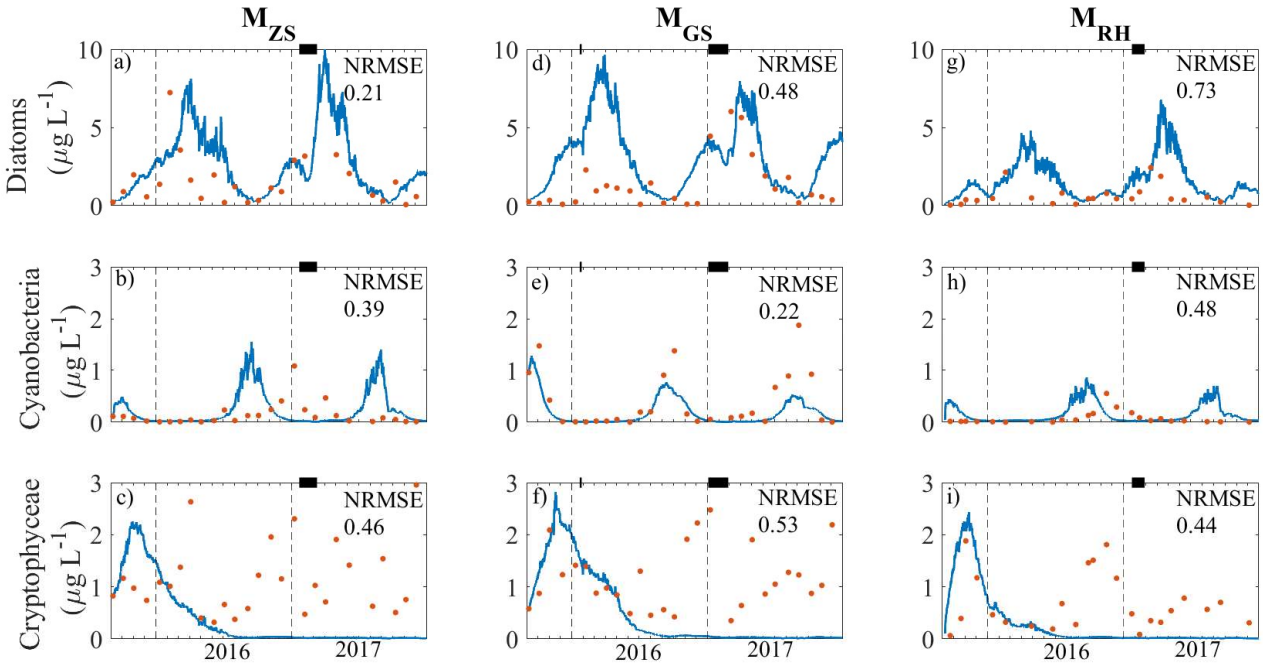

Figure 4.6: Simulated and measured phytoplankton concentration in Lower lake Constance. Simulated (lines) and measured (dots) Diatoms, Cyanobacteria and Cryptophyceae in M_{ZS}, M_{GS} and M_{RH} during the simulated period. The simulated Chlorophyll-a concentration was vertically averaged along the entire water column in M_{GS} and along the uppermost 20 m in M_{ZS} and M_{RH}. The simulated concentration was compared against field measurements by means of the Normalized Root Mean Square Error (NRMSE). Ice cover presence in the three stations was indicated by a black bar at the panel top.

The comparison of the vertical distribution of Cyanobacteria in the stations M_{GS} and M_{ZS} during their peak reveal that, whereas Cyanobacteria in M_{ZS} developed in the surface-mixed layer, in M_{GS} they formed a deep chlorophyll maximum between 380-385 m a.s.l. (Fig. 4.7). Field data obtained with the FluoroProbe (BBE FluoroProbe, Moldaenke) showed a deep maximum in the Diatoms and Cryptophyceae channels on 10th October 2017, but closer to the lake bottom (height = 375-380 m a.s.l.) than the simulated one.

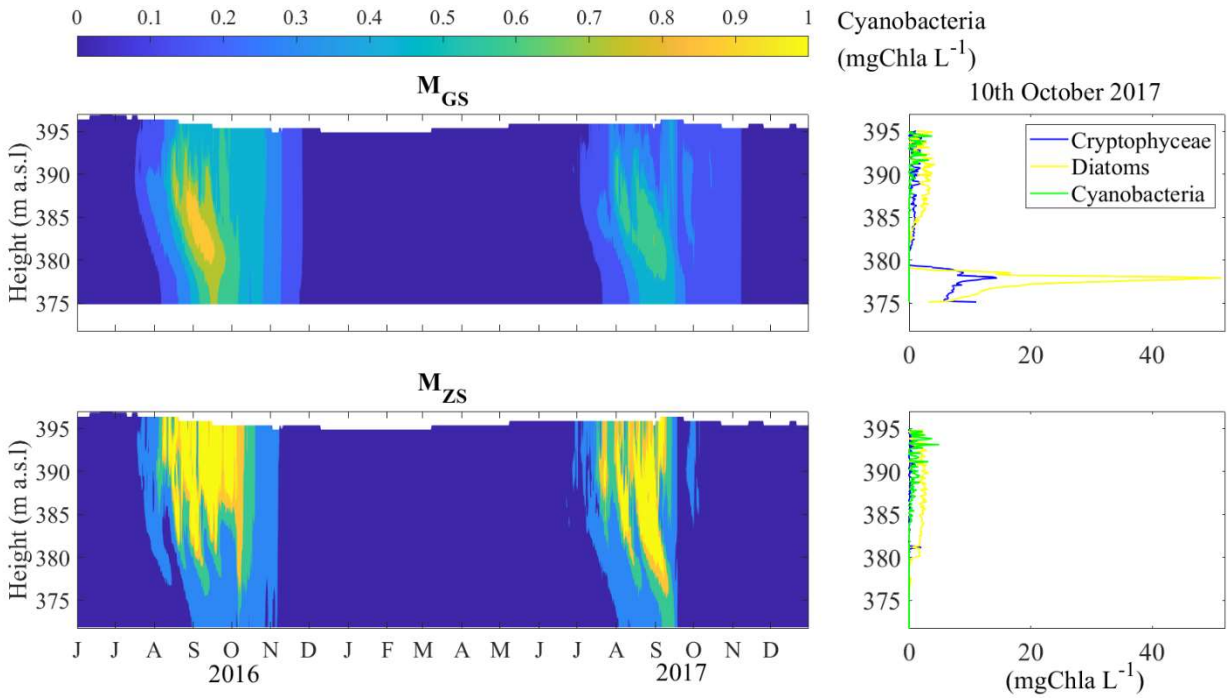

Figure 4.7: Vertically-resolved simulated Cyanobacteria concentration in the lake against field data. The vertical profile of simulated Cyanobacteria concentration in the stations M_{GS} and MZS was compared against a field data. The sample was taken with the FluoroProbe (BBE FluoroProbe, Moldaenke) during the typical period for Cyanobacteria blooms (10th October 2017).

The vertically-averaged concentration of Cyanobacteria showed that, during the peak in the year 2016, they developed abundant around the shores of Zeller See (Fig. 4.8a) and in the pelagic water of Gnadensee (Fig. 4.8b). Diatoms after ice-off (1st April 2017) were instead mainly distributed along the shores of Zellersee and Gnadensee and most abundant in the south-eastern part of Gnadensee. The concentration of Diatoms in the basin of Rheinsee was lower than in the other basins (Fig. 4.8c,d).

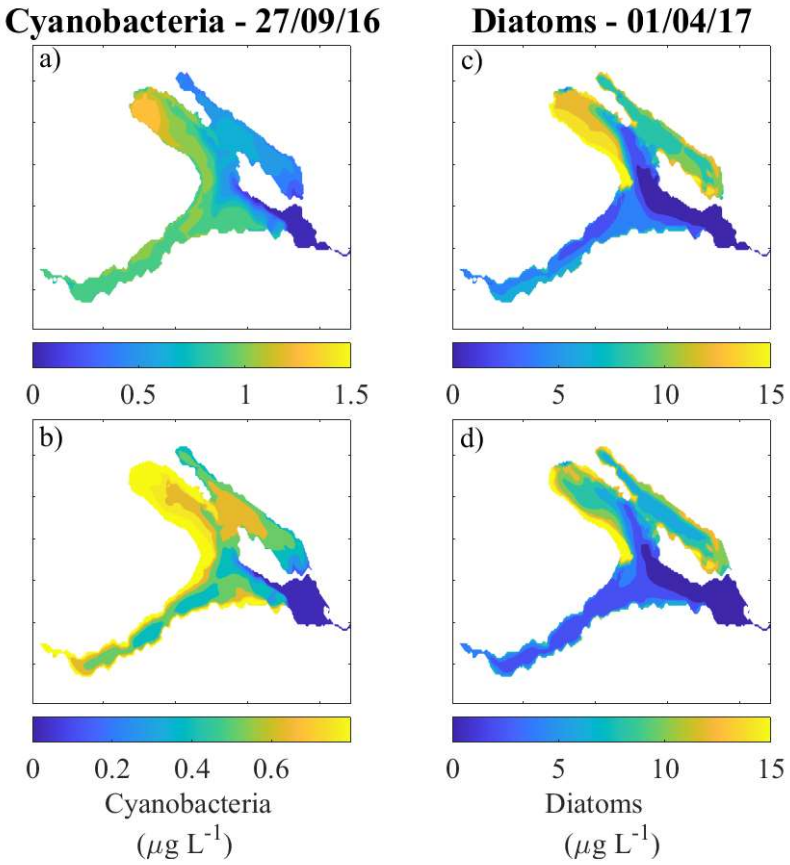

Figure 4.8: Distribution of Cyanobacteria and Diatoms in the lake during their blooms. Snapshot of the vertically-averaged concentration of Cyanobacteria and Diatoms in the top 10 m (a, c) and along the entire water column (b, d) during their blooms (27th September 2016 for Cyanobacteria and 1st April 2017 for Diatoms).

4.4 Discussion

Model performance in simulating dissolved oxygen

The model accurately simulated the seasonal patterns of dissolved oxygen observed in the deep water of LLC (Fig. 4.2). The fit between simulated and observed DO concentration at the lake bottom as measured by RMSE and NRMSE was indeed within the ranges reported in previous modelling studies simulating lakes anoxia (Snortheim et al., 2017; Bocaniov et al., 2020). The simulations overestimated instead epilimnetic DO, as a result of the underestimation of the primary production rather than the effect of a too high sediment oxygen demand. In Suppl. 4F, we showed

indeed that halving the parameter regulating the sediment oxygen demand, the NRMSE at the lake surface remained however above 0.25 in all the three sub-basins.

Model results demonstrate that the inter-annual variation of anoxia in LLC during the years considered was mainly influenced by changes in water temperature rather than changes in the hypolimnion thickness (Lake Erie in Lam & Schertzer, 1987). Indeed, the thermocline depth did not significantly differ between the years considered (Suppl. 4E), whereas the bottom water in M_{ZS} was in the year 2016 2°C warmer than in the year 2017, resulting in stronger DO depletion, stronger inter-annual variation in late summer DO concentrations, and a heavier dependence on the sediment oxygen demand (Fig. 4.2 and Suppl. 4E).

The inter-basin differences of anoxia are nevertheless not originated by the same driver. Indeed, despite the basin of Gnadensee is usually characterized by lower water temperature at the basin bottom than Zeller See, Fig. 4.2e-f showed that it is more subjected to anoxic conditions than this latter basin. Indeed, the well-oxygenated water from the Seerhein intruding during summer under the thermocline sustained the oxygenation of the deep water of Zeller See, whereas the shallow sill between Gnadensee and Zeller See obstacles the entrance of well-oxygenated water in the most enclosed basin (Chapter 3).

Model performance in simulating nutrients

The model simulated more abundant nutrients concentration in Zeller See and Gnadensee than in Rheinsee. Indeed, this latter basin is more under the influence of the water of river Seerhein and thus of the poor-in-nutrients ULC, whereas the high nutrient concentration in Zeller See is caused by the high nutrient load coming from the inflow Radolfzeller Aach (Suppl. 4A).

However, the model had difficulties to simulate the release of PO4 and NH4, as well as the depletion of NO3, during stratified periods, in particular in the basin of Gnadensee. That can be explained by the different sediment composition among the three sub-basins that is not taken into account in the static sediment model of AEM3D. The basin of GS probably has sediments with more oxygen-consuming organic matter compared with the deeper sub-basins. Similar difficulties in accounting for different sediment composition were observed in other studies simulating the nutrient dynamics in morphologically complex lakes (Von Westernhagen, 2010).

Model performance in simulating phytoplankton

The adequate simulation of phytoplankton is one of the main issues in freshwater ecological modelling (Rigosi et al., 2010). As it has been showed in many studies (Arhonditsis & Brett, 2004; Carraro et al., 2012; Rinke et al., 2010; Trolle et al., 2008), the model performances in simulating nutrient and biological variables are in general lower than for water temperature and dissolved oxygen, attributable to the complexity governing these higher ecological levels (Missaghi & Hondzo, 2010; Robson & Hamilton, 2004; Vilhena et al., 2010). Moreover, phytoplankton has a key function in lake ecosystems as it is the trophic cornerstone of the pelagic food web since it provides biomass towards higher trophic levels like zooplankton and fish. Moreover, modelling algae is inherently difficult because of their lateral patchiness, vertical distributions, temporal variations (blooming), zooplankton grazing and the still evolving understanding of algae biological dynamics (Hipsey et al., 2006; Reynolds, 2006).

Numerous studies have shown that the inclusion of zooplankton and its grazing on phytoplankton is necessary to accurately simulate phytoplankton (Kerimoglu et al., 2013; Peeters et al., 2007). Although ELCOM-CAEDYM has been largely employed to simulate phytoplankton and occasionally also zooplankton (Jones, 2011), the zooplankton module of AEM3D is still at an early stage. Indeed, several bugs were founded and stated in Suppl 4D. Moreover, modelling zooplankton not only requires parameterization of grazing and growth from resources, but also simulation of losses to limit zooplankton population growth. Fish predation is an important factor in controlling zooplankton growth, but requires simulation of another trophic level. We therefore decided to close the plankton model by driving phytoplankton loss from zooplankton data in the three sub-basins (Suppl. 4C). However, the inclusion of zooplankton grazing prevented phytoplankton to growth again after summer. Therefore, the approximation of zooplankton as vertically and horizontally homogenous within each basin could have led to a too high grazing pressure during summer. We decided then to simulate phytoplankton dynamics disregarding zooplankton grazing.

The aim to predict the spatial variations of Chlorophyll-a concentration in LLC through the representation of three phytoplankton groups was achieved with higher accuracy ($RMSE_{ZS}$=2.54 μg L^{-1}; $RMSE_{GS}$=4.35 μg L^{-1}; $RMSE_{RH}$= 1.88 μg L^{-1}; Suppl. 4I) than previous modelling studies in other morphologically complex lakes. For example, Missaghi and Hondzo (2010) modelled one phytoplankton group in Lake Minnetonka using ELCOM–CAEDYM. Their results point to a high

degree of error at all stations (R^2<0.5) and reported the failure of the model to capture the seasonal phytoplankton peaks in the lake. The modelling study of two phytoplankton groups in the morphologically complex Lake Rotoiti was characterized by a RMSE of 5.03 μg L^{-1} (Von Westernhagen, 2010). Our accuracy was even above many 1D modelling studies (Burger et al., 2008: RMSE=13.1 μg L^{-1}; Trolle et al., 2008: RMSE=10.40 μg L^{-1}).

Our model succeeded in simulating the main dynamics of the three phytoplankton groups in the three lake sub-basins. Typical seasonal algae dominant succession in LLC begins with Diatoms bloom during the winter-spring followed by Cryptophyceae in early summer and then fully dominated by Cyanobacteria for the rest of the season. Cryptophyceae concentration decreased in spring and did not recover because of temperature and phosphorous limitations (Suppl. 4G), as well as increasing mortality. Restarting the simulation after summer months allowed this phytoplankton group to growth again (Suppl. 4G).

The overestimation of Diatoms dynamic during fall 2015 – spring 2016 may be due to the fact that the model was used to simulate phytoplankton groups and may fail in reproducing the dynamic of specific taxa, which may have characteristic properties and life-traits. Field data from IGKB (2018) show indeed in winter 2016 an abundant presence of Stephanodiscus Neoastraea, whereas in winter 2017 the most abundant Diatoms taxa was Asterionella Formosa. Moreover, Suppl. 4H showed that the growth of Diatoms during winter was strongly influenced by the presence of ice cover. The inverse temperature stratification that develops under ice allows phytoplankton to be contained in the upper part of the water column, just below the ice sheet, where light may be still sufficient for balanced or positive phytoplankton growth. The simulation of thin ice cover in M_{GS} that would have not been developed in the field due to the breaking effect of waves and wind could have created favorable conditions for the bloom of Diatoms in M_{GS} that did not occur in reality. In winter 2017, when abundant ice cover was simulated and observed in the lake the fit model-data with respect to Diatoms concentration was so good in all the three sub-basins that this study can be enumerate among the few studies that successfully simulated under-ice phytoplankton dynamics (Semovski et al., 2000; Bouffard et al. 2019; Oveisy et al., 2014).

Moreover, the model showed that the winter Diatoms blooms develop abundant along the lake shores, especially in Gnadnesee, where usually more abundant ice cover develops. The summer blooms caused by Cyanobacteria instead develop along the shore of Zeller See and in the pelagic zone of Gnadensee, where they form a metalimnetic peak. Deep chlorophyll maxima (DCM) are generally an indication of high water clarity that allows the chlorophyll layer to persist below the surface mixed layer (Hamilton et al., 2010; Pérez et al., 2002). Some species of Cyanobacteria indeed can form dense metalimnetic populations as other species compete less effectively at

reduced irradiance levels and they are strongly nutrient-limited in the surface mixed layer (Dokulil & Teubner, 2000). The model results agreed with the vertical resolved data obtained with the FluoroProbe that showed a DCM in the Diatoms/Cryptophyceae channel in the basin of Gnadensee. Indeed, P-Rubescens has a higher phycoerythrin content and its fluorescence signal (dominated by red emission) is closer to the factory-calibrated Cryptophyceae signal than the Cyanobacteria one (rich in phycocyanin) (Carraro et al., 2012).

Overall, the model captured the heterogeneity of the system in term of phytoplankton and water quality and showed that a 3D analysis was needed to adequately gain insight into the spatial and temporal biogeochemistry distribution of Lower Lake Constance. The long run time and the complex morphometry of LLC, with three distinct basins of different depth, hydrodynamic and ice cover formation, contribute to a level of modelling complexity that has rarely been applied in 3D modelling approaches before.

Conclusion

This study has evaluated the use of a three-dimensional hydrodynamic-ecological model to reproduce the spatiotemporal variability of nutrient distribution and phytoplankton in the three sub-basins of the morphologically complex LLC. Measured data in LLC reflect indeed a system with large spatial and temporal water quality which necessitates the use of a 3D model to capture its biogeochemical changes. The model AEM3D was selected and configured for this analysis through an intensive calibration and validation process against monthly field measurements in the three lake's sub-basins. The model was able to capture the main spatial and temporal biogeochemistry variations, among which the progressive summer oxygen depletion at lake's bottom, as well as the typical seasonal algae dominant succession in LLC. Results demonstrated that numerical models with an adequate representation of hydrodynamic and bio-chemical processes can be of great importance in providing more detailed understanding of the drivers of spatiotemporal variability in the lake and in compensating for the absence of continuous and spatially-extended field measurements.

Acknowledgments

We thank David Hamilton and Hiroshi Yajima for their help and support with the model setting and parametrization. We acknowledge Chris Dallimore from Hydronumerics for his help in developing the model. The water quality data was provided by the Landesanstalt fuer Umwelt Baden-Wuerttemberg (LUBW). This study was financially supported by the German Research Foundation (DFG) within the framework of the RTG R3 (Research Training Group – Responses to biotic and abiotic changes, Resilience and Reversibility of lake ecosystems), grant number 298726046/GRK2272/A4.

Supplement

4A. Model boundary conditions

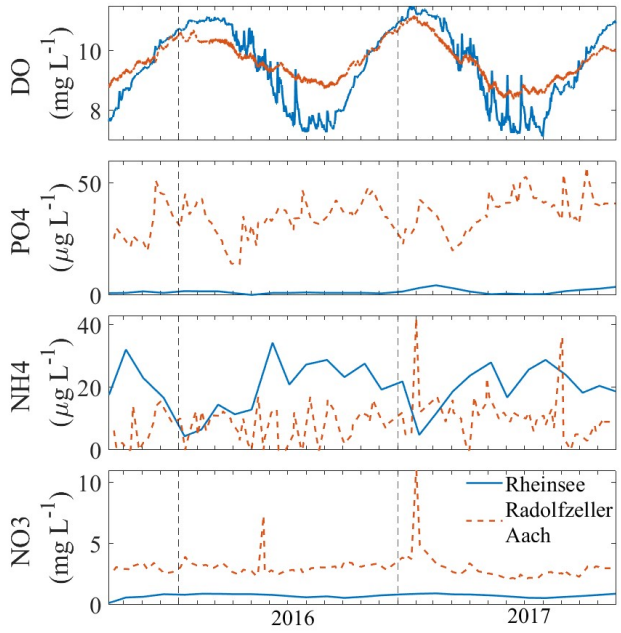

Figure 4.9: Time series of the measured or derived boundary conditions used for the model set-up. Time series of the concentration of a) dissolved oxygen (DO), b) phosphate (PO4), c) nitrate (NO3) and d) ammonium (NH4) of the river Seerhein and Radolfzeller Aach during the simulated period.

4B. Model Set-up

Carbon

```
.false. simulate_dic_pH
1.04    DOCL_sedflux_T_multiplier
0.00    DOCL_sedflux_max_rate
0.10000 DOCL_sedflux_Ox_half_sat
0.01    DOCL_light_attenuation
0.003   mineralisation_coefficient
1.5     O2_mineralisation_half_saturation
0.8     O2_mineralisation_anaerobic_factor
1.08    temperature_mineralisation_multiplier
```

Nitrogen

```
1.1     NH4_sedflux_T_multiplier
0.0200  NH4_sedflux_max_rate
0.02    NH4_sedflux_Ox_half_sat
1.1     NO3_sedflux_T_multiplier
-0.10   NO3_sedflux_max_rate
0.020000   NO3_sedflux_Ox_half_sat
1.05     DONL_sedflux_T_multiplier
0.00001  DONL_sedflux_max_rate
0.50000  DONL_sedflux_Ox_half_sat
0.05000    nitrification_coefficient
1.08000    temperature_nitrification_multiplier
2.00000    O2_nitrification_half_saturation
3.42857    nitrification_O_to_N
0.1     denitrification_coefficient
1.09    temperature_denitrification_multiplier
0.3     O2_denitrification_half_saturation
1.25    denitrification_C_to_N
0.16    refractory_ratio
0.005   mineralisation_coefficient
1.5     O2_mineralisation_half_saturation
0.8     O2_mineralisation_anaerobic_factor
1.08    temperature_mineralisation_multiplier
.false. simulate_pin
.1      nh4_sorption_c1
.1      nh4_sorption_c2
.1      PIN_resuspension_rate_k
.1      PIN_resuspension_kt
.1      PIN_critical_shear
```

Oxygen

```
.true.    simulate_oxygen
.false.   sbp_model
1.1       sedflux_T_multiplier
1.35      sedflux_max_rate
0.05      sedflux_Ox_half_sat
```

Phosphorous

```
1.09    PO4_sedflux_T_multiplier
0.3     PO4_sedflux_max_rate
0.0005  PO4_sedflux_Ox_half_sat
1.09     DOPL_sedflux_T_multiplier
0.001    DOPL_sedflux_max_rate
0.30000  DOPL_sedflux_Ox_half_sat
0.5      refractory_ratio
0.02   mineralisation_coefficient
1.5    O2_mineralisation_half_saturation
1.6    O2_mineralisation_anaerobic_factor
1.08   temperature_mineralisation_multiplier
```

4C. Zooplankton modelling in LLC

Initially, we attempted to include in our simulations zooplankton grazing by driving phytoplankton loss from zooplankton data in the three sub-basins. Monthly vertically-integrated samples of zooplankton concentration were obtained by the LUBW (Fig. 4.10).

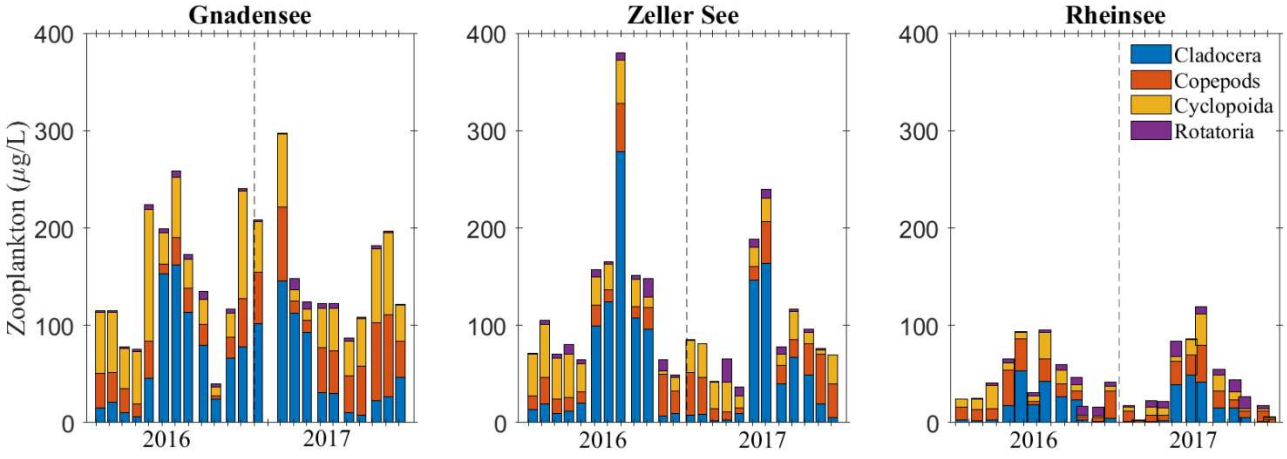

Figure 4.10: Zooplankton concentration in each basin of LLC in the years 2016 and 2017. Monthly data provided by LUBW about the concentration of Cladocera, Copopods, Cyclopodia and Rototaria in the sub-basins of LLC. Only data about Cladocera and Copopods were used in this study.

We decided to simulate the grazing pressure of the two most abundant zooplankton species (Copopods and Cladocera) to limit the computational time that increases with the number of simulated variables. The zooplankton concentration measured at the stations M_{GS}, M_{ZS} and M_{RH} (Fig. 4.10) was assumed as horizontally and vertically homogeneous in the corresponding basin. The zooplankton concentration was kept constant over time and updated every two weeks with the values obtained from the linear interpolation of the field measurements.

The parameter governing the zooplankton grazing are the grazing rate (G_Z), the parameters describing the grazing temperature dependence ($T_{OPT,Z}$, $T_{MAX,Z}$, $T_{STD,Z}$, θ_z) and the zooplankton preference for each phytoplankton group (P_{ZA}) (Tab. 4.2). Indeed, the rate of removal of phytoplankton from the water due to grazing by zooplankton is determined as fraction of the total grazing rate ($P_{ZA} \cdot G_Z$), where G_Z is the grazing rate of the zooplankton group Z and P_{za} is a dimensionless number between 0 and 1 accounting for the grazing preference of Z for the phytoplankton group A. We assumed that Zooplankton grazes only on Diatoms, the most abundant phytoplankton group in LLC, and therefore it had a total grazing preference for this group of 1. The description of its temperature dependence was derived by the study of Jones (2011), while the grazing rate was assumed as for Upper Lake Constance in the study of Kerimoglu et al. (2013).

Table 4.2: List of parameters in AEM3D describing the zooplankton dynamics. For each parameter its symbol, unit and assigned value for each group are shown. Literature sources: [a]Jones (2011), [b]Kerimoglu et al. (2013).

Zooplankton	**Symbol**	**Unit**	**Cladocera**	**Copopods**
Grazing rate	G_z	mg Chl-a g CZoo^{-1} d^{-1}	0.8 [b]	0.5 [b]
Preference for Diatoms	$P_{Z,Diatoms}$	-	1	1
Preference for Cryptophyceae	$P_{Z,Crypto}$	-	-	-
Preference for Cyanobacteria	$P_{Z,Cyano}$	-	-	-
Temperature multiplier for grazing	θ_g	-	1.08 [a]	1.08 [a]
Standard grazing temperature	T_{STD}	°C	18 [a]	13 [a]
Optimum grazing temperature	T_{OPT}	°C	21 [a]	15 [a]
Maximum grazing temperature	T_{MAX}	°C	36 [a]	33 [a]

We compared the output of the simulations with and without zooplankton in terms of Diatoms concentration. As model results showed (Fig. 4.11), the inclusion of zooplankton prevented phytoplankton from growing again in late fall, also halving the grazing rate of both zooplankton groups.

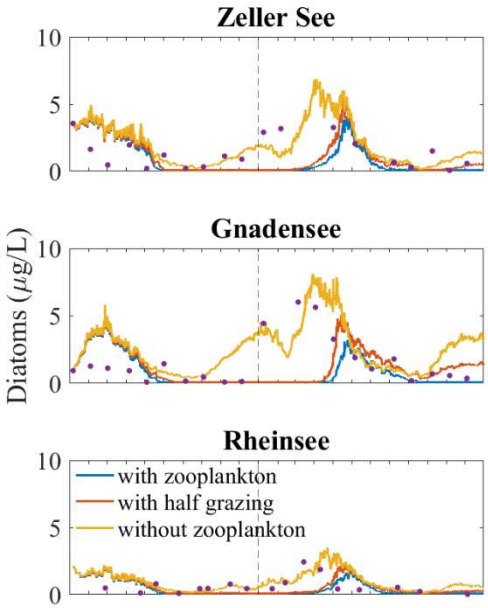

Figure 4.11: Simulated and measured Chlorophyll-a concentration in Lower lake Constance with and without zooplankton grazing. Simulated (lines) and measured (dots) Chlorophyll-a concentration in M_{ZS}, M_{GS} and M_{RH} during the simulated period. Three different simulations were run: blue) including zooplankton grazing pressure as in Tab. 4.2 (blue), including the zooplankton grazing pressure, but halving the grazing rate in Tab. 4.3 (red), and without zooplankton grazing (yellow).

4D. Bugs of the zooplankton module

During the model set-up different bugs of the zooplankton module of AEM3D were found:

Bug 1 (AEM3D v. 344)
Developer contacted: 5.5.2020;
Bug solved: 8.5.2020
Bug: despite the zooplankton grazing was set to zero, the introduction of zooplankton caused the disappearance of phytoplankton.

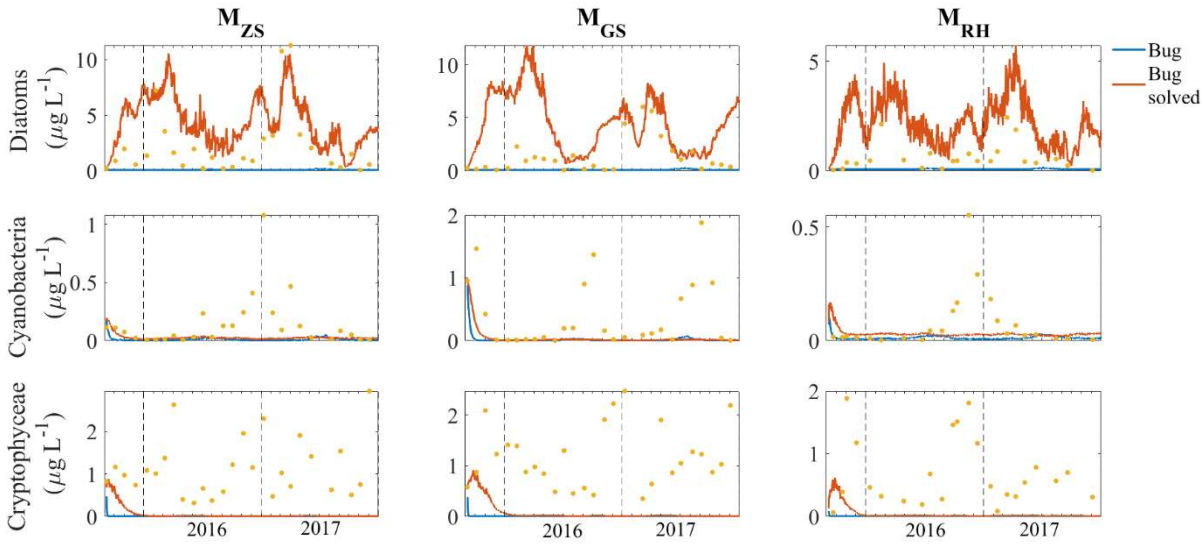

Figure 4.12: Bug number 1 of the zooplankton module. Comparison between the model results before (blue) and after (red) the fixing of the bug. Simulated (lines) and measured (dots) Diatoms concentration in M_{ZS}, M_{GS} and M_{RH} during the simulated period.

Bug 2 (AEM3D v. 347)

Developer contacted 23.6.2020;

Bug solved: 13.7.2020

Bug: Anomalous growth of the phytoplankton groups for which a grazing preference above zero was prescribed.

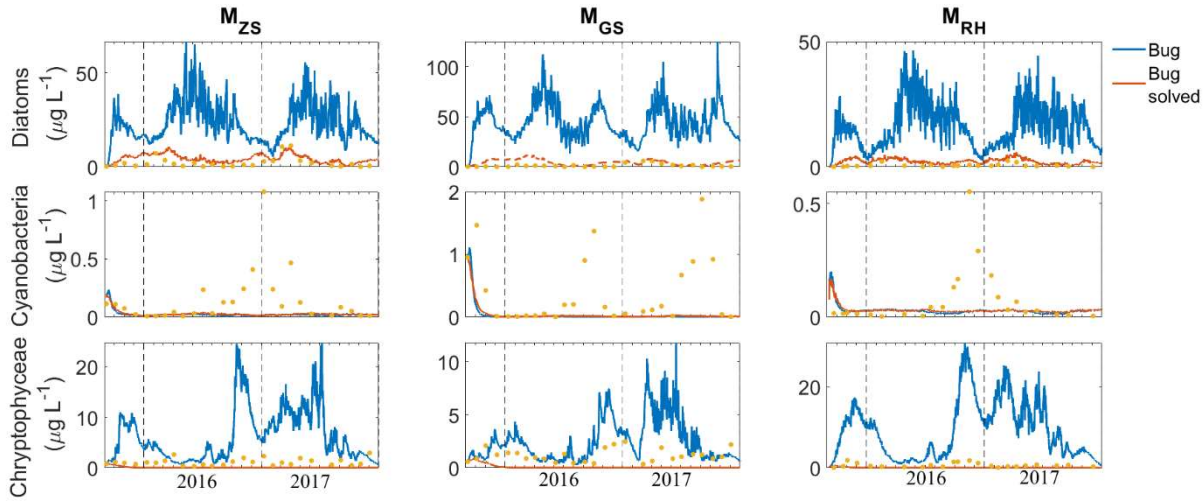

Figure 4.13: Bug number 2 of the zooplankton module. Comparison between the model results before (blue) and after (red) the fixing of the bug. Simulated (lines) and measured (dots) Diatoms concentration in M_{ZS}, M_{GS} and M_{RH} during the simulated period.

4E. Simulated thermal structure

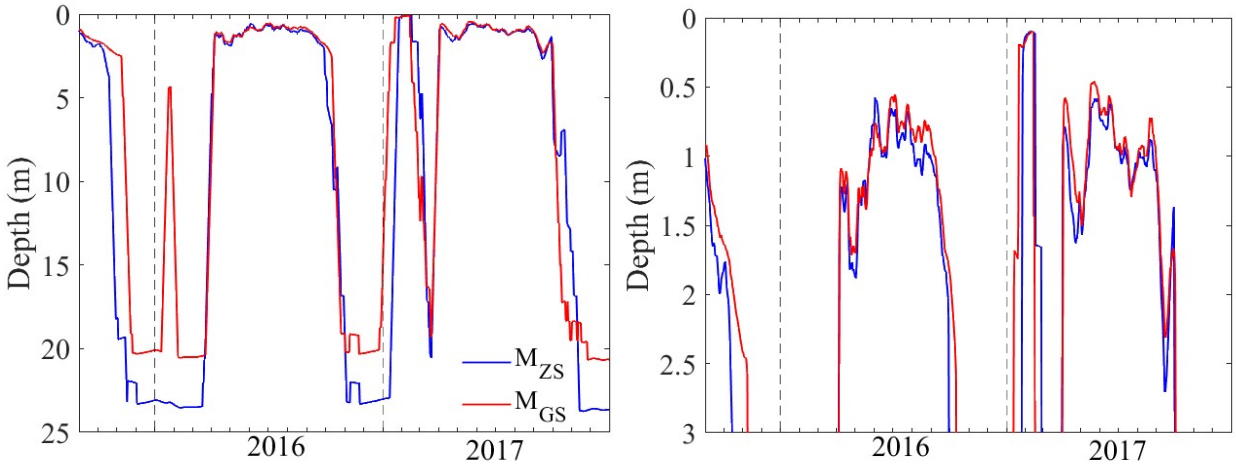

Figure 4.14: Simulated Mixed Layer Depth (MLD) in M_{GS} and M_{ZS}. The right panel shows the MLD in the uppermost 3 m of the water column.

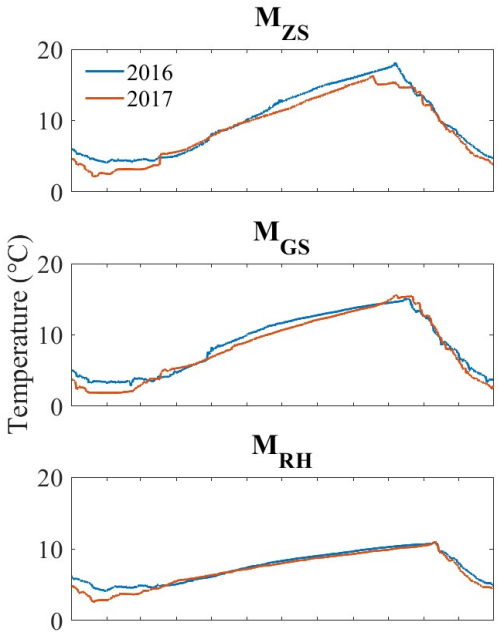

Figure 4.15: Inter-annual comparison of simulated water temperature at the lake bottom. Comparison of the simulated water temperature during the year 2016 (blue) and 2017 (red) in the station M_{ZS}, M_{GS} and M_{RH}.

4F. Dissolved oxygen

We run a simulation with half value of sedflux_max_rate to understand if the error of the simulated DO concentration in the mixed-layer was driven by the high sediment oxygen demand. Fig. 4.16 showed that halving the parameter regulating the SOD, the NRMSE at the lake surface remained above 0.25 in all the three sub-basins.

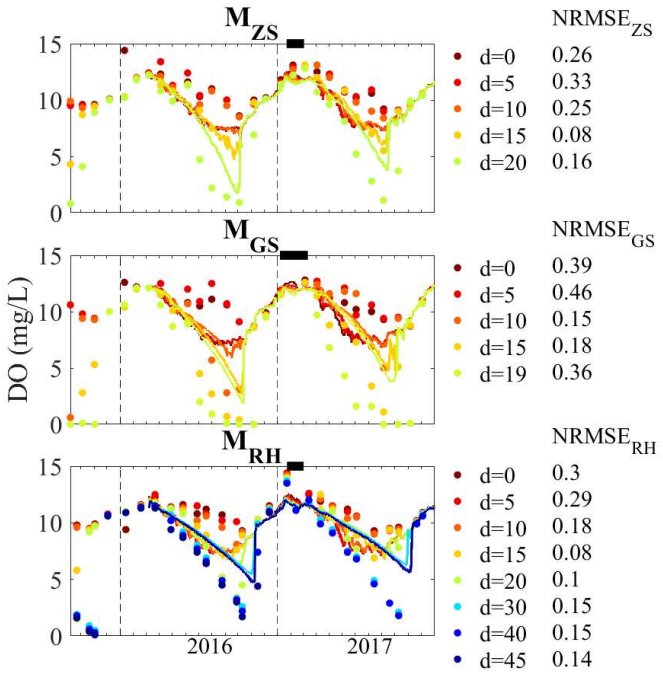

Figure 4.16: Simulated dissolved oxygen concentration (DO) in Lower lake Constance with half sedflux_max_rate. Simulated DO in a) M_{ZS}, b) M_{GS} and c) M_{RH} during the simulated period. The simulated concentration was compared and the corresponding Normalized Root Mean Square Error (NRMSE) was computed against the available field data (dots) at different depths. Ice cover periods in the three stations were indicated by a black bar at the panel top.

4G. Cryptophyceae

The model was set up to run from September 2016 until December 2017 to check if, with a new initialization of Cryptophyceae, this group could recover in fall 2016.

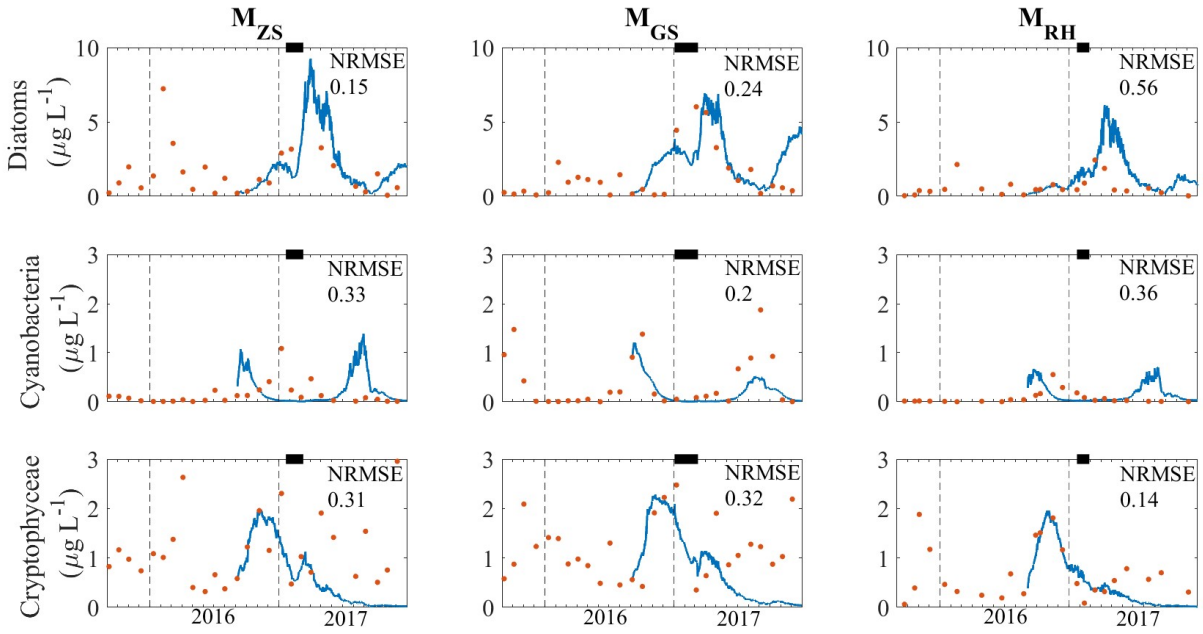

Figure 4.17: Simulated and measured phytoplankton concentration in Lower lake Constance. Simulated (lines) and measured (dots) Diatoms, Cyanobacteria and Cryptophyceae in M_{ZS}, M_{GS} and M_{RH} during the simulated period (starting in September 2016). The simulated concentration was compared against field measurements by means of the Normalized Root Mean Square Error (NRMSE). Ice cover presence in the three stations was indicated by a black bar at the panel top.

The model was set-up to provide information about the time series of the growth limitation functions $(f(P), f(N), f(I), f^T)$ at 1 m depth in M_{ZS} for Cryptophyceae to investigate the causes of their disappearance in summer 2016. Each individual growth limitation functions spans from 0 to 1: phytoplankton production is maximal when the value of limitation is close to 1. The hourly limitation terms were smoothed with a 2-days running mean.

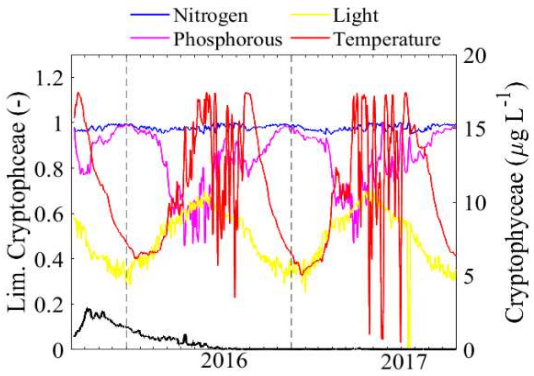

Figure 4.18: Cryptophyceae growth limitation factors in M_{ZS}. The limitations referred to 1 m depth in M_{ZS}. The black solid line is instead the concentration of Cryptophyceae in M_{ZS}.

4H. Phytoplankton under ice cover

We compared the Diatoms distribution in M_{GS} and M_{ZS} during winter 2016 and 2017 (Fig. 4.19). In the year 2016, thin ice cover developed only in Gnadensee at the end of February. Indeed, less than 1 cm thick ice was simulated in M_{GS}. Instead, in year 2017, the model simulated up to 87% of the lake surface covered by ice (Caramatti et al. 2020) and up to 8 cm and 4.5 cm thick ice respectively at the station M_{GS} and M_{ZS}. Fig. 4.18 showed that Diatoms grew abundantly in the uppermost 1-2 m of the water column when ice cover developed.

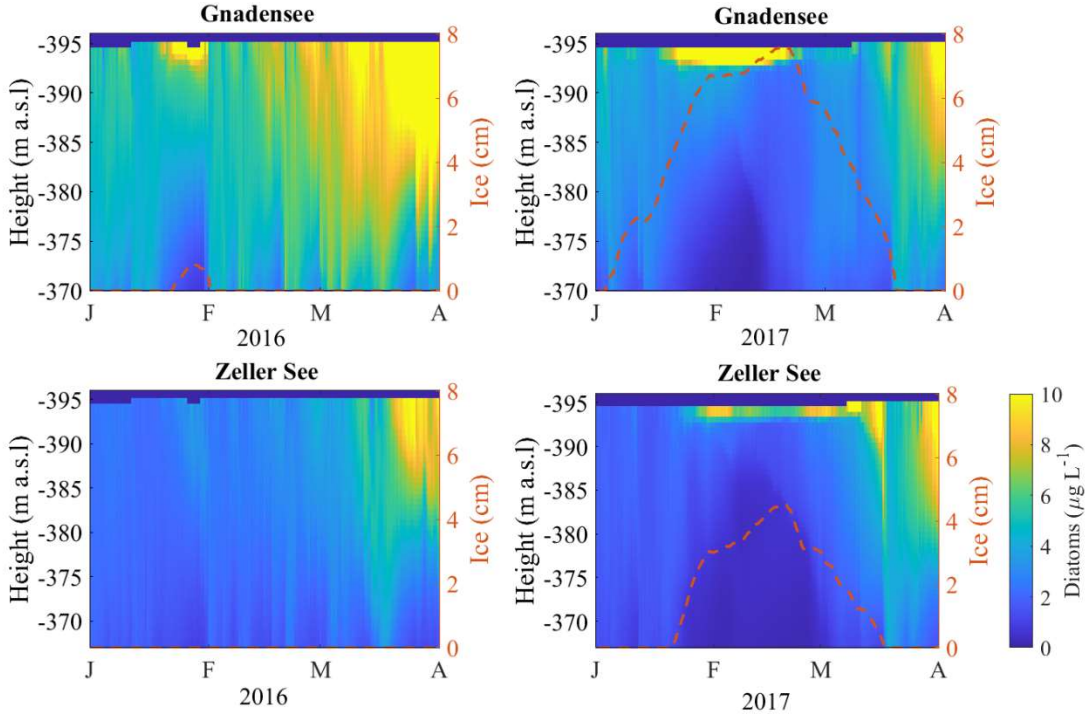

Figure 4.19: Simulated Diatoms concentration in M_{GS} and M_{ZS} in winter 2016 and winter 2017. The ice cover thickness in the two stations was indicated by the red dashed line.

4I. Evaluation of the model fit against field data

The accuracy of the simulation in terms of phytoplankton and chlorophyll-a concentration with respect to the field measurements was evaluated in the stations M_{GS}, M_{ZS} and M_{RH} using additional statistical error, such as the Root Mean Square Error (RMSE) and Mean Absolute Error (MAE) to facilitate the comparison with other modelling studies. Their formulas are:

$$RMSE = \left[\frac{1}{N}\sum_{i=1}^{N}(x(t_i) - y(t_i))^2\right]^{1/2} \qquad \text{and} \qquad MAE = \left[\frac{1}{N}\sum_{i=1}^{N}(|x(t_i) - y(t_i)|)\right]$$

where *x* and *j* are respectively the measured and simulated vertical mean concentration at the date t_i in M_{GS}, M_{ZS} or M_{RH} and N represents the number of records.

Table 4.3: The simulated phytoplankton and Chlorophyll-a concentration were compared against field measurements by means of the Normalized Root Mean Square Error (NRMSE), Root Mean Square Error (RMSE) and Mean Absolute Error (MAE).

	NRMSE (-)	**RMSE (µg L^{-1})**	**MAE (µg L^{-1})**
Diatoms M_{ZS}	0.43	2.91	2.31
Cyanobacteria M_{ZS}	0.91	0.09	0.05
Cryptophyceae M_{ZS}	0.39	0.89	0.64
Diatoms M_{GS}	1.9	4.17	3.58
Cyanobacteria M_{GS}	0.16	0.23	0.11
Cryptophyceae M_{GS}	0.25	0.4	0.3
Diatoms M_{RH}	0.73	1.52	1.08
Cyanobacteria M_{RH}	0.36	0.15	0.1
Cryptophyceae M_{RH}	0.37	0.67	0.43
Chlorophyll-a M_{ZS}	0.34	2.54	2.06
Chlorophyll-a M_{GS}	1.85	4.35	3.68
Chlorophyll-a M_{RH}	0.80	1.88	1.56

5

General discussion and perspectives

The characterization of lake hydrodynamic and water quality with WQMs is of particular importance for a good understanding of the lake's processes and its responses to changes. In particular, in a morphologically complex lake, like Lower Lake Constance, a 3D analysis is needed in capturing the significant water quality heterogeneities and the ecological hot spots. Our results addressed some of the factors governing the spatiotemporal heterogeneity of the phytoplankton community between the sub-basins of Lower lake Constance, such as the spatiotemporal variability in ice cover formation and inter-basin exchange in the lake.

Our findings demonstrated that during winter inter-basins differences are strongly enhanced. Indeed, as a result of the complex interaction between lake morphometry, stream intrusion and stratification frequent and abundant ice cover developed in Gnadensee, whereas less frequent and abundant in the other two sub-basins (Chapter 2). This leads to very different conditions in terms of light availability, temperature and turbulence for the phytoplankton growth within LLC. Chapter 4 showed indeed that the inverse temperature stratification that develops under ice allows phytoplankton to be contained in the upper part of the water column, just below the ice sheet, where light may be still sufficient for balanced or positive phytoplankton growth. These conditions favor the abundant growth of Diatoms in Gnadensee (Chapter 4).

Moreover, during winter periods the water exchange between Gnadensee and Zeller See is lower than in summer (Chapter 3) and then in that period more different conditions between these two basins are expected in terms of nutrients and organisms. Similarly, the water exchange between the river Seerhein and Gnadensee is also more limited than is summer. Therefore, Gnadensee results to be less under the influence of the water from the river Seerhein and hence also under the conditions of the upstream Upper Lake Constance (Chapter 3). Consequently, the dilution effect of dissolved substances in Gnadensee caused by the poor-in-nutrients water from the river Seerhein is expected to be less important than in summer.

The high vulnerability of winter conditions to climate warming could in the future lead to reduced inter-basin spatial variability. Indeed, Chapter 3 showed that climate warming results in reduced ice cover and an earlier onset and longer duration of stratification, leading to enhanced inter-basin exchange especially during winter and spring. That, together with the changing in light availability resulting from shorter ice cover duration or absence of ice cover, could have a strong impact on the diatoms bloom that usually occurs early in the year and take advantage from the presence of ice cover (Chapter 4). Furthermore, the fraction of water from Upper Lake Constance reaching the rather secluded basin Gnadensee in winter increases with climate warming and could imply a larger dilution of dissolved substances in Gnadensee (Chapter 3).

In summer, the higher current speeds in the lake and the bigger area of the cross-section above the sill resulting from water level changes favors higher water exchange in the lake and therefore more homogenous conditions are expected. However, inter-basins differences in terms of dissolved oxygen, nutrients and phytoplankton persist also during that period. Indeed, despite the entrance of well-oxygenated water from the river Seerhein in Gnadensee is enhanced, Chapter 4 provided evidences that it is not enough to prevent the establishment of severe anoxic conditions in that basin. In Zeller See, instead, the Seerhein water intruding below the lake mixed layer depth favors the oxygenation of the basin deep water. Furthermore, a deep chlorophyll maximum of Cyanobacteria usually develops only in Gnadensee and not in Zeller See (Chapter 4).

The future reduced inter-seasonal pattern of water level in LLC may implying larger horizontal differences of dissolved substances and organisms between lake sub-basin during summer months (Chapter 3). This could sharpen the differences in oxygen level at the bottom of the lake sub-basins leading to more severe anoxic conditions in Gnadensee. Moreover, it could reduce the export of cyanobacteria from Gnadensee to Zeller See, which may result in a larger deep chlorophyll maximum in Gnadensee than today.

The findings reported in these chapters have advanced the understanding of the spatiotemporal variability of physical and biochemical processes in a complex waterbody with heterogeneous morphology, also under consideration of a changing climate.

Future perspectives

A correct simulation of the ice cover formation process in the lake can integrate field measurements. These indeed often suffer from the lack of both temporal and spatial coverage, especially for study sites of relatively large domains or characterized by highly spatially variable conditions (Brown & Dugay, 2010). Moreover, numerical simulations of ice cover can compensate for the limited performances of remote sensing in distinguishing between blue ice and water and in obtaining quality images due to the obscuring effect of cloud cover. For LLC, for instance, no continuous and systematic records on ice cover exist and a remote sensing approach is limited by cloud cover and fog during wintertime. Our dataset in Chapter 2 has been indeed gathered from a citizen science approach from multiple sources (e.g. social media, newspaper, Water Police).

The calibrated and validated model of Chapter 2 could be now used to generate a long-term dataset about spatiotemporal information of ice cover in LLC. Future research projects assessing the effect of climate warming on the lake could indeed benefit from it. According with the availability of the input forcing, the model's set-up could be indeed extended up to cover the period 1990 - 2021. However, the windfield from COSMO does not exist before 2009. Consequently, the sensitivity of results to a constant versus a spatially variable wind should be assessed.

Together with limitations in collecting systematic and extended records of ice cover, also under-ice sampling is limited, mainly due to logistical difficulties and safety concerns associated with conditions of winter sampling (Wright, 1964; Twiss et al., 2012). This thus hinders the fully understand of the effects of ice-cover on the biogeochemical processes in lakes (Oveisy et al., 2014). Numerical models with an adequate representation of ice cover, hydrodynamics and biochemical processes can be of great importance in providing researchers with more detailed understanding of the role of ice cover on water quality and plankton dynamics. Hence, the coupled hydrodynamic and ecosystem model of Chapter 4 could be used to investigate the processes governing under-ice water quality and phytoplankton dynamics in the three sub-basins of LLC and extend our conclusion of Chapter 4. Moreover, the formation of partial ice cover in the lake allows to compare the physical and ecological dynamics between under-ice and open water.

Lastly, the model setup of Chapter 4 could be also employed to assess the effect of enhanced/reduced inter basin exchange caused by the scenarios of Chapter 3 on the inter-basin variability of phytoplankton and nutrient distribution. However, the model limitation in dynamically simulating zooplankton obstacles the possibility to perform scenarios that would also affect the

zooplankton abundance, e.g. climate warming. Water level scenarios might be simulated, assuming their effect on zooplankton growth negligible.

References

Aeschbach-Hertig, W., Kipfer, R., Hofer, M., Imboden, D. M., & Baur, H. (1996). Density-driven exchange between the basins of Lake Lucerne (Switzerland) traced with the 3H-3He method. *Limnology and Oceanography*, *41*(4), 707–721.

Alavian, V., Jirka, G. H., Denton, R. A., Johnson, M. C., & Stefan, H. G. (1992). Density currents entering lakes and reservoirs. *Journal of Hydraulic Engineering*, *118*(11), 1464–1489.

Andersen, M. R., Sand-Jensen, K., Woolway, R. I., & Jones, I. D. (2017). Profound daily vertical stratification and mixing in a small, shallow, wind-exposed lake with submerged macrophytes. *Aquatic Sciences*, *79*(2), 395–406.

Appt, J., Imberger, J., & Kobus, H. (2004). Basin-scale motion in stratified Upper Lake Constance. *Limnology and Oceanography*, *49*(4), 919–933.

Arhonditsis, G. B., & Brett, M. T. (2004). Evaluation of the current state of mechanistic aquatic biogeochemical modeling. *Marine Ecology Progress Series*, *271*, 13–26.

Arrigo, K. R., Perovich, D. K., Pickart, R. S., Brown, Z. W., Van Dijken, G. L., Lowry, K. E., … Bahr, F. (2012). Massive phytoplankton blooms under Arctic sea ice. *Science*, *336*(6087), 1408.

Austin, J., & Colman, S. (2008). A century of temperature variability in Lake Superior. *Limnology and Oceanography*, *53*(6), 2724–2730.

Bartish, T. (1987). A review of exchange processes among the three basins of Lake Erie. *Journal of Great Lakes Research*, *13*(4), 607–618.

Beletsky, D., & Schwab, D. J. (2001). Modeling circulation and thermal structure in Lake Michigan: Annual cycle and interannual variability. *Journal of Geophysical Research: Oceans*, *106*(C9), 19745–19771.

Bennett, J. R. (1974). On the dynamics of wind-driven lake currents. *Journal of Physical Oceanography*, *4*(3), 400–414.

Bernard, O., & Rémond, B. (2012). Validation of a simple model accounting for light and temperature effect on microalgal growth. *Bioresource Technology*, *123*, 520–527.

Bocaniov, S. A., Lamb, K. G., Liu, W., Rao, Y. R., & Smith, R. E. H. (2020). High sensitivity of lake hypoxia to air temperatures, winds, and nutrient loading: Insights from a 3-D lake model. *Water Resources Research*, *56*(12), e2019WR027040.

Bouffard, D., Zdorovennova, G., Bogdanov, S., Efremova, T., Lavanchy, S., Palshin, N., … Wüest, A. (2019). Under-ice convection dynamics in a boreal lake. *Inland Waters*, *9*(2), 142–161.

Bruggeman, J. (2011). A phylogenetic approach to the estimation of phytoplankton Traits 1. *Journal of Phycology*, *47*(1), 52–65.

Burger, D. F., Hamilton, D. P., & Pilditch, C. A. (2008). Modelling the relative importance of internal and external nutrient loads on water column nutrient concentrations and phytoplankton biomass in a shallow polymictic lake. *Ecological Modelling*, *211*(3–4), 411–423.

Caramatti, I., Peeters, F., Hamilton, D., & Hofmann, H. (2020). Modelling inter-annual and spatial variability of ice cover in a temperate lake with complex morphology. *Hydrological Processes*.

Carraro, E., Guyennon, N., Hamilton, D., Valsecchi, L., Manfredi, E. C., Viviano, G., … Copetti, D. (2012). Coupling high-resolution measurements to a three-dimensional lake model to assess the spatial and temporal dynamics of the cyanobacterium Planktothrix rubescens in a medium-sized lake. In *Phytoplankton responses to human impacts at different scales* (pp. 77–95). Springer.

Chen, C. A., & Millero, F. J. (1986). Thermodynamic properties for natural waters covering only the limnological range 1. *Limnology and Oceanography*, *31*(3), 657–662.

Cloern, J. E., Grenz, C., & Vidergar-Lucas, L. (1995). An empirical model of the phytoplankton chlorophyll: carbon ratio-the conversion factor between productivity and growth rate. *Limnology and Oceanography*, *40*(7), 1313–1321.

Coats, R., Perez-Losada, J., Schladow, G., Richards, R., & Goldman, C. (2006). The warming of lake Tahoe. *Climatic Change*, *76*(1–2), 121–148.

Coppetti, D., Tartari, G., Morabito, G., Oggioni, A., Legnani, E., & Imberger, J. (2006). A biogeochemical model of Lake Pusiano (North Italy) and its use in the predictability of phytoplankton blooms: first preliminary results. *Journal of Limnology*, *65*(1), 59.

Cortés, A., Fleenor, W. E., Wells, M. G., de Vicente, I., & Rueda, F. J. (2014). Pathways of river water to the surface layers of stratified reservoirs. *Limnology and Oceanography*, *59*(1), 233–250.

CRREL-US Army Corps of Engineers. Web site: http://www.integralhse.co.uk/ice-safety/

De Cesare, G., Boillat, J.-L., & Schleiss, A. J. (2006). Circulation in stratified lakes due to flood-induced turbidity currents. *Journal of Environmental Engineering*, *132*(11), 1508–1517.

Dessai, S., Hulme, M., Lempert, R., & Pielke Jr, R. (2009). Climate prediction: a limit to adaptation. *Adapting to Climate Change: Thresholds, Values, Governance*, 64–78.

Dibike, Y., Prowse, T., Bonsal, B., de Rham, L., & Saloranta, T. (2012). Simulation of North American lake-ice cover characteristics under contemporary and future climate conditions. *International Journal of Climatology*, *32*(5), 695–709.

Dissanayake, P., Hofmann, H., & Peeters, F. (2019). Comparison of results from two 3D hydrodynamic models with field data: Internal seiches and horizontal currents. *Inland Waters*, *9*(2), 239–260.

Dokulil, M. T., & Teubner, K. (2000). Cyanobacterial dominance in lakes. *Hydrobiologia*, *438*(1), 1–12.

Doms, G., Baldauf, M., & Baldauf, M. (2018). Consortium for Small-Scale Modelling A Description of the Nonhydrostatic Regional COSMO-Model Part I : Dynamics and Numerics.

Duguay, C. R., Flato, G. M., Jeffries, M. O., Ménard, P., Morris, K., & Rouse, W. R. (2003). Ice-cover variability on shallow lakes at high latitudes: model simulations and observations. *Hydrological Processes*, *17*(17), 3465–3483.

Eder, M., Rinke, K., Kempke, S., Huber, A., & Wolf, T. (2008). Seeweite Bodensee-Messkampagne 2007 als Test für BodenseeOnline. *WasserWirtschaft*, *98*(10), 34–38.

Effler, S. W., Prestigiacomo, A. R., Effler, A. J. P., & Driscoll, C. (2010). Water quality patterns in a river-lake system from multiple drivers (Three Rivers, New York State). *River Systems*, *19*(1), 75–94.

Elçi, Ş. (2008). Effects of thermal stratification and mixing on reservoir water quality. *Limnology*, *9*(2), 135–142.

Elliott, J A, Reynolds, C. S., & Irish, A. E. (2001). An investigation of dominance in phytoplankton using the PROTECH model. *Freshwater Biology*, *46*(1), 99–108.

Elliott, J Alex. (2020). Modelling lake phytoplankton communities: recent applications of the PROTECH model. *Hydrobiologia*, 1–9.

Eppley, R. W., Reid, F. M. H., Cullen, J. J., Winant, C. D., & Stewart, E. (1984). Subsurface patch of a dinoflagellate (Ceratium tripos) off Southern California: patch length, growth rate, associated vertically migrating species. *Marine Biology*, *80*(2), 207–214.

Fang, X., & Stefan, H. G. (1996). Long-term lake water temperature and ice cover simulations/measurements. *Cold Regions Science and Technology*, *24*(3), 289–304.

Fang, X., & Stefan, H. G. (2009). Simulations of climate effects on water temperature, dissolved oxygen, and ice and snow covers in lakes of the contiguous US under past and future climate scenarios. *Limnology and Oceanography*, *54*(6part2), 2359–2370.

Fragoso Jr, C. R., Marques, D. M. L. M., Collischonn, W., Tucci, C. E. M., & van Nes, E. H. (2008). Modelling spatial heterogeneity of phytoplankton in Lake Mangueira, a large shallow subtropical lake in South Brazil. *Ecological Modelling*, *219*(1–2), 125–137.

Franssen, H. J. H., & Scherrer. (2008). Freezing of lakes on the Swiss plateau in the period 1901-2006. *International Journal for Climatology*, *28*(December 2008). https://doi.org/10.1002/joc.

Frassl, M. A., Rothhaupt, K.-O., & Rinke, K. (2014). Algal internal nutrient stores feedback on vertical phosphorus distribution in large lakes. *Journal of Great Lakes Research*, *40*, 162–172.

Freeman, A. M., Jose, F., Roberts, H. H., & Stone, G. W. (2015). Storm induced hydrodynamics and sediment transport in a coastal Louisiana lake. *Estuarine, Coastal and Shelf Science*, *161*, 65–75.

Fujisaki, A., Wang, J., Hu, H., Schwab, D. J., Hawley, N., & Rao, Y. R. (2012). A modeling study of ice–water processes for Lake Erie applying coupled ice-circulation models. *Journal of Great Lakes Research*, *38*(4), 585–599.

Fujisaki, A., Wang, J., Bai, X., Leshkevich, G., & Lofgren, B. (2013). Model-simulated interannual variability of Lake Erie ice cover, circulation, and thermal structure in response to atmospheric forcing, 2003–2012. *Journal of Geophysical Research: Oceans*, *118*(9), 4286–4304.

Gal, G., Hipsey, M. R., Parparov, A., Wagner, U., Makler, V., & Zohary, T. (2009). Implementation of ecological modeling as an effective management and investigation tool: Lake Kinneret as a case study. *Ecological Modelling*, *220*(13–14), 1697–1718.

Gerbush, M. R., Kristovich, D. A. R., & Laird, N. F. (2008). Mesoscale boundary layer and heat flux variations over pack ice–covered Lake Erie. *Journal of Applied Meteorology and Climatology*, *47*(2), 668–682.

Giling, D. P., Staehr, P. A., Grossart, H. P., Andersen, M. R., Boehrer, B., Escot, C., … Obrador, B. (2017). Delving deeper: Metabolic processes in the metalimnion of stratified lakes. *Limnology and Oceanography*, *62*(3), 1288–1306. https://doi.org/10.1002/lno.10504.

Gregg, M. C. (2004). Small-scale processes in straits. *Deep Sea Research Part II: Topical Studies in Oceanography*, *51*(4–5), 489–503.

Griffin, S. L., Herzfeld, M., & Hamilton, D. P. (2001). Modelling the impact of zooplankton grazing on phytoplankton biomass during a dinoflagellate bloom in the Swan River Estuary, Western Australia. *Ecological Engineering*, *16*(3), 373–394.

Goudsmit, G., Peeters, F., Gloor, M., & Wüest, A. (1997). Boundary versus internal diapycnal mixing in stratified natural waters. *Journal of Geophysical Research: Oceans*, *102*(C13), 27903–27914.

Goudsmit, G., Burchard, H., Peeters, F., & Wüest, A. (2002). Application of k-ϵ turbulence models to enclosed basins: The role of internal seiches. *Journal of Geophysical Research: Oceans*, *107*(C12).

Haghighi, A. T., & Kløve, B. (2015). A sensitivity analysis of lake water level response to changes in climate and river regimes. *Limnologica*, *51*, 118–130.

Hamilton, D. P., Hocking, G. C., & Patterson, J. C. (1997). Criteria for selection of spatial dimension in the application of one-and two-dimensional water quality models. *Mathematics and Computers in Simulation*, *43*(3–6), 387–393.

Hamilton, D. P, O'Brien, K. R., Burford, M. A., Brookes, J. D., & McBride, C. G. (2010). Vertical distributions of chlorophyll in deep, warm monomictic lakes. *Aquatic Sciences*, *72*(3), 295–307.

Hamilton, D. P., Magee, M. R., Wu, C. H., & Kratz, T. K. (2018). Ice cover and thermal regime in a dimictic seepage lake under climate change. *Inland Waters*, *8*(3), 381–398.

Hampton, S. E., Galloway, A. W. E., Powers, S. M., Ozersky, T., Woo, K. H., Batt, R. D., … Lottig, N. R. (2017). Ecology under lake ice. *Ecology Letters*, *20*(1), 98–111.

Hebbert, B., Patterson, J., Loh, I., & Imberger, J. (1979). Collie river underflow into the Wellington reservoir. *Journal of Hydraulic Engineering*, *105*(5), 533–545.

Heiskanen, J. J., Mammarella, I., Ojala, A., Stepanenko, V., Erkkilä, K., Miettinen, H., … Järvinen, H. (2015). Effects of water clarity on lake stratification and lake-atmosphere heat exchange. *Journal of Geophysical Research: Atmospheres*, *120*(15), 7412–7428.

Higgins, S. N., & Zanden, M. J. Vander. (2010). What a difference a species makes: a meta–analysis of dreissenid mussel impacts on freshwater ecosystems. *Ecological Monographs*, *80*(2), 179–196.

Hibler, W. D. (1979). A dynamic thermodynamic sea ice model. *Journal of Physical Oceanography*, *9*(4), 815–846.

Hipsey, M. R., Romero, J. R., Antenucci, J. P., & Hamilton, D. (2006). Computational aquatic ecosystem dynamics model: CAEDYM v2. *Contract Research Group, Centre for Water Research, University of Western Australia*, *90*.

Hodges, B. R. (2000). Numerical Techniques in CWR-ELCOM (code release v. 1). *CWR Manuscript WP*, *1422*.

Hodges, B. R., Imberger, J., Saggio, A., & Winters, K. B. (2000). Modeling basin-scale internal waves in a stratified lake. *Limnology and Oceanography*, *45*(7), 1603–1620.

Hodges, B. (1998). Heat budget and thermodynamics at a free surface: Some theory and numerical implementation. *Centre for Water Research, University of Western Australia, Crawley, WA, Australia*.

Hodges, B, & Dallimore, C. (2016). Aquatic Ecosystem Model: AEM3D v1. 0 User Manual. *Hydronumerics Pty Ltd*.

Hodges, Ben, & Dallimore, C. (2018). *HydroNumerics*.

Hodgkins, G. A., James, I. C., & Huntington, T. G. (2002). Historical changes in lake ice-out dates as indicators of climate change in New England, 1850–2000. *International Journal of Climatology: A Journal of the Royal Meteorological Society*, *22*(15), 1819–1827.

Hohmann, R., Hofer, M., Kipfer, R., Peeters, F., Imboden, D. M., Baur, H., & Shimaraev, M. N. (1998). Distribution of helium and tritium in Lake Baikal. *Journal of Geophysical Research: Oceans*, *103*(C6), 12823–12838.

Igkb. (2012). Limnologischer Zustand des Bodensees. *Grüner Bericht Nr. 39*.

Igkb. (2016). Limnologischer Zustand des Bodensees. *Grüner Bericht Nr. 41*.

Igkb. (2018). Limnologischer Zustand des Bodensees. *Grüner Bericht Nr. 42*.

Imberger, Jörg, & Patterson, J. C. (1989). Physical limnology. *Advances in Applied Mechanics*, *27*, 303–475.

Imberger, J., & Patterson, J. C. (1989). Physical limnology. *Advances in Applied Mechanics*, *27*, 303–475.

Imberger, Jorg. (1998). Flux paths in a stratified lake: A review. *Physical Processes in Lakes and Oceans*, *54*, 1–17.

Imberger, Jorg, Loh, I., Hebbert, B., & Patterson, J. (1978). Dynamics of reservoir of medium size. *Journal of the Hydraulics Division*, *104*(5), 725–743.

Kalff, J. (2002). *Limnology: inland water ecosystems.*

Kirillin, G., Hochschild, J., Mironov, D., Terzhevik, A., Golosov, S., & Nützmann, G. (2011). FLake-Global: Online lake model with worldwide coverage. *Environmental Modelling & Software*, *26*(5), 683–684.

Kjaran, S. P., Hólm, S. L., & Myer, E. M. (2004). Lake circulation and sediment transport in Lake Myvatn. *Aquatic Ecology*, *38*(2), 145–162.

Kupisch, M., Moenickes, S., Schlief, J., Frassl, M., & Richter, O. (2012). Temperature-dependent consumer-resource dynamics: A coupled structured model for Gammarus pulex (L.) and leaf litter. *Ecological Modelling*, *247*, 157–167.

Jiang, L., Xia, M., Ludsin, S. A., Rutherford, E. S., Mason, D. M., Jarrin, J. M., & Pangle, K. L. (2015). Biophysical modeling assessment of the drivers for plankton dynamics in dreissenid-colonized western Lake Erie. *Ecological Modelling*, *308*, 18–33.

Joehnk, K. D., Huisman, J. E. F., Sharples, J., Sommeijer, B. E. N., Visser, P. M., & Stroom, J. M. (2008). Summer heatwaves promote blooms of harmful cyanobacteria. *Global Change Biology*, *14*(3), 495–512.

Jones, E. L. (2011). *Ecological Modelling of Lake Erie: Sensitivity Analysis and Simulation of Nutrient, Phytoplankton and Zooplankton Dynamics*. University of Waterloo.

Kalff, J. (2002). *Limnology: inland water ecosystems.*

Kerimoglu, O., Straile, D., & Peeters, F. (2013). Seasonal, inter-annual and long term variation in top–down versus bottom–up regulation of primary production. *Oikos*, *122*(2), 223–234.

Kerimoglu, O., Straile, D., & Peeters, F. (2014). Modeling the spring blooms of ciliates in a deep lake. *Hydrobiologia*, *731*(1), 173–189.

Laborde, S., Antenucci, J. P., Copetti, D., & Imberger, J. (2010). Inflow intrusions at multiple scales in a large temperate lake. *Limnology and Oceanography*, *55*(3), 1301–1312.

LaBounty, J. F., & Horn, M. J. (1997). The influence of drainage from the Las Vegas valley on the limnology of Boulder Basin, Lake Mead, Arizona-Nevada. *Lake and Reservoir Management*, *13*(2), 95–108.

Lam, D. C. L., & Schertzer, W. M. (1987). Lake Erie thermocline model results: comparison with 1967–1982 data and relation to anoxic occurrences. *Journal of Great Lakes Research*, *13*(4), 757–769.

Lang, U., Schick, R., & Schroder, G. (2010). The decision support system Bodenseeonline for hydrodynamics and water quality in Lake Constance. In *Decision support systems, advances in*. IntechOpen.

Laval, B., Imberger, J., Hodges, B. R., & Stocker, R. (2003). Modeling circulation in lakes: Spatial and temporal variations. *Limnology and Oceanography*, *48*(3), 983–994.

Leon, L. F., Smith, R. E. H., Hipsey, M. R., Bocaniov, S. A., Higgins, S. N., Hecky, R. E., … Guildford, S. J. (2011). Application of a 3D hydrodynamic–biological model for seasonal and spatial dynamics of water quality and phytoplankton in Lake Erie. *Journal of Great Lakes Research*, *37*(1), 41–53.

Leon, L. F., Antenucci, J. P., Rao, Y. R., & McCrimmon, C. (2012). Summary performance of the Estuary and Lake Computer Model (ELCOM): application in the Laurentian and other Great Lakes. *Water Quality Research Journal*, *47*(3–4), 252–267.

Lewis, D. M., Elliott, J. A., Lambert, M. F., & Reynolds, C. S. (2002). The simulation of an Australian reservoir using a phytoplankton community model: PROTECH. *Ecological Modelling*, *150*(1–2), 107–116.

Lindim, C., Pinho, J. L., & Vieira, J. M. P. (2011). Analysis of spatial and temporal patterns in a large reservoir using water quality and hydrodynamic modeling. *Ecological Modelling*, *222*(14), 2485–2494.

Liu, S., Ye, Q., Wu, S., & Stive, M. J. F. (2018). Horizontal circulation patterns in a large shallow lake: Taihu Lake, China. *Water*, *10*(6), 792.

Livingstone, D. M. (1993). Temporal structure in the deep-water temperature of four swiss lakes: A short-term climatic change indicator? *Internationale Vereinigung Für Theoretische Und Angewandte Limnologie: Verhandlungen*, *25*(1), 75–81.

Livingstone, D. M. (2003). Impact of secular climate change on the thermal structure of a large temperate central European lake. *Climatic Change*, *57*(1–2), 205–225.

Lizotte, M. P., Sharp, T. R., & Priscu, J. C. (1996). Phytoplankton dynamics in the stratified water column of Lake Bonney, Antarctica. *Polar Biology*, *16*(3), 155–162.

Loose, B., McGillis, W. R., Schlosser, P., Perovich, D., & Takahashi, T. (2009). Effects of freezing, growth, and ice cover on gas transport processes in laboratory seawater experiments. *Geophysical Research Letters*, *36*(5).

Lorenzen, C. J. (1968). Carbon/Chlorophyll relationships in and upwelling area. *Limnology and Oceanography*, *13*(1), 202–204.

Luft, G., & van den Eertwegh, G. (1991). Long-term changes in the water level of Lake Constance and possible causes. *Proc. Vienna Symp. Hydrology of Natural and Manmade Lakes. IAHS Publ. 206*, 31–44.

Lung, W.-S. (2001). *Water quality modeling for wasteload allocations and TMDLs*. John Wiley & Sons.

MacIntyre, S., Romero, J. R., & Kling, G. W. (2002). Spatial-temporal variability in surface layer deepening and lateral advection in an embayment of Lake Victoria, East Africa. *Limnology and Oceanography*, *47*(3), 656–671.

Mack, R. N., Simberloff, D., Mark Lonsdale, W., Evans, H., Clout, M., & Bazzaz, F. A. (2000). Biotic invasions: causes, epidemiology, global consequences, and control. *Ecological Applications*, *10*(3), 689–710.

Magnuson, J. J., Robertson, D. M., Benson, B. J., Wynne, R. H., Livingstone, D. M., Arai, T., … Kuusisto, E. (2000). Historical trends in lake and river ice cover in the Northern Hemisphere. *Science*, *289*(5485), 1743–1746.

Michel, A., Brauchli, T., Lehning, M., Schaefli, B., & Huwald, H. (2020). Stream temperature and discharge evolution in Switzerland over the last 50 years: annual and seasonal behaviour. *Hydrology and Earth System Sciences*, *24*(1), 115–142.

Mishra, V., Cherkauer, K. A., Bowling, L. C., & Huber, M. (2011). Lake Ice phenology of small lakes: Impacts of climate variability in the Great Lakes region. *Global and Planetary Change*, *76*(3–4), 166–185.

Missaghi, S., & Hondzo, M. (2010). Evaluation and application of a three-dimensional water quality model in a shallow lake with complex morphometry. *Ecological Modelling*, *221*(11), 1512–1525.

Nguyen, T. D., Hawley, N., & Phanikumar, M. S. (2017). Ice cover, winter circulation, and exchange in S aginaw B ay and L ake H uron. *Limnology and Oceanography*, *62*(1), 376–393.

Nguyen, T. D., Thupaki, P., Anderson, E. J., & Phanikumar, M. S. (2014). Summer circulation and exchange in the Saginaw Bay-Lake Huron system. *Journal of Geophysical Research: Oceans*, *119*(4), 2713–2734.

Nihoul, J. C. J., Adam, P., Brasseur, P., Deleersnijder, E., Djenidi, S., & Haus, J. (1993). Three-dimensional general circulation model of the northern Bering Sea's summer ecohydrodynamics. *Continental Shelf Research*, *13*(5–6), 509–542.

Niu, Q., Xia, M., Rutherford, E. S., Mason, D. M., Anderson, E. J., & Schwab, D. J. (2015). Investigation of interbasin exchange and interannual variability in L ake E rie using an unstructured-grid hydrodynamic model. *Journal of Geophysical Research: Oceans*, *120*(3), 2212–2232.

O'Reilly, C. M., Alin, S. R., Plisnier, P.-D., Cohen, A. S., & McKee, B. A. (2003). Climate change decreases aquatic ecosystem productivity of Lake Tanganyika, Africa. *Nature*, *424*(6950), 766.

O'Reilly, C. M., Sharma, S., Gray, D. K., Hampton, S. E., Read, J. S., Rowley, R. J., … Kraemer, B. M. (2015). Rapid and highly variable warming of lake surface waters around the globe. *Geophysical Research Letters*, *42*(24), 10–773.

Okubo, A. (1971). Oceanic diffusion diagrams. In *Deep sea research and oceanographic abstracts* (Vol. 18, pp. 789–802). Elsevier.

Oveisy, A., Boegman, L., & Imberger, J. (2012). *Three-dimensional simulation of lake and ice dynamics during winter*. *57*(1), 43–57. https://doi.org/10.4319/lo.2012.57.1.0043.

Oveisy, A., Rao, Y. R., Leon, L. F., & Bocaniov, S. A. (2014a). Three-dimensional winter modeling and the effects of ice cover on hydrodynamics, thermal structure and water quality in Lake Erie. *Journal of Great Lakes Research*, *40*, 19–28.

Oveisy, A., & Boegman, L. (2014b). One-dimensional simulation of lake and ice dynamics during winter. *Journal of Limnology*, *73*(3).

Paerl, H. W., & Huisman, J. (2008). Blooms like it hot. *Science*, *320*(5872), 57–58.

Paerl, H. W. (2014). Mitigating harmful cyanobacterial blooms in a human-and climatically-impacted world. *Life*, *4*(4), 988–1012.

Parkinson, C. L., & Washington, W. M. (1979). A large-scale numerical model of sea ice. *Journal of Geophysical Research: Oceans*, *84*(C1), 311–337.

Patterson, J. C., & Hamblin, P. F. (1988). Thermal simulation of a lake with winter ice cover 1. *Limnology and Oceanography*, *33*(3), 323–338.

Peeters, F. (2000). Correction to "Vertical turbulent diffusion and upwelling in Lake Baikal estimated by inverse modeling of transient tracers" by F. Peeters, R. Kipfer, M. Hofer, DM Imboden, and VM Domysheva. *J. Geophys. Res*, *105*(14,283).

Peeters, F., Straile, D., Lorke, A., & Livingstone, D. M. (2007a). Earlier onset of the spring phytoplankton bloom in lakes of the temperate zone in a warmer climate. *Global Change Biology*, *13*(9), 1898–1909.

Peeters, F., Straile, D., Lorke, A., & Ollinger, D. (2007b). Turbulent mixing and phytoplankton spring bloom development in a deep lake. *Limnology and Oceanography*, *52*(1), 286–298.

Peeters, F., & Hofmann, H. (2015). Length-scale dependence of horizontal dispersion in the surface water of lakes, 1917–1934. https://doi.org/10.1002/lno.10141.

Pérez, G. L., Queimaliños, C. P., & Modenutti, B. E. (2002). Light climate and plankton in the deep chlorophyll maxima in North Patagonian Andean lakes. *Journal of Plankton Research*, *24*(6), 591–599.

Rajar, R., & Cetina, M. (1997). Hydrodynamic and water quality modelling: An experience. *Ecological Modelling*, *101*(2), 195–207. https://doi.org/https://doi.org/10.1016/S0304-3800(97)00047-1.

Rao, Y. R., Marvin, C. H., & Zhao, J. (2009). Application of a numerical model for circulation, temperature and pollutant distribution in Hamilton Harbour. *Journal of Great Lakes Research*, *35*(1), 61–73.

Perroud, M., Goyette, S., Martynov, A., Beniston, M., & Annevillec, O. (2009). Simulation of multiannual thermal profiles in deep Lake Geneva: A comparison of one-dimensional lake models. *Limnology and Oceanography*, *54*(5), 1574–1594.

Razmi, A. M., Barry, D. A., Lemmin, U., Bonvin, F., Kohn, T., & Bakhtyar, R. (2014). Direct effects of dominant winds on residence and travel times in the wide and open lacustrine embayment: Vidy Bay (Lake Geneva, Switzerland). *Aquatic Sciences*, *76*(1), 59–71.

Read, J. S., Hamilton, D. P., Jones, I. D., Muraoka, K., Winslow, L. A., Kroiss, R., … Gaiser, E. (2011). Derivation of lake mixing and stratification indices from high-resolution lake buoy data. *Environmental Modelling and Software*, *26*(11), 1325–1336. https://doi.org/10.1016/j.envsoft.2011.05.006.

Reynolds, C. S. (1997). *Vegetation processes in the pelagic: a model for ecosystem theory* (Vol. 9). Ecology Institute Oldendorf.

Reynolds, C. S. (2006). *The ecology of phytoplankton*. Cambridge University Press.

Rigosi, A., Fleenor, W., & Rueda, F. (2010). State-of-the-art and recent progress in phytoplankton succession modelling. *Environmental Reviews*, *18*(NA), 423–440.

Rinke, K., Eder, M., Peeters, F., Kuemmerlin, R., Gal, G., & Rothhaupt, K.-O. (2009). Simulating phytoplankton community dynamics in Lake Constance with a coupled hydrodynamic-ecological model. *Internationale Vereinigung Für Theoretische Und Angewandte Limnologie: Verhandlungen*, *30*(5), 701–704.

Rinke, K., Yeates, P., & Rothhaupt, K. (2010). A simulation study of the feedback of phytoplankton on thermal structure via light extinction. *Freshwater Biology*, *55*(8), 1674–1693.

Robertson, D. M., & Ragotzkie, R. A. (1990). Changes in the thermal structure of moderate to large sized lakes in response to changes in air temperature. *Aquatic Sciences*, *52*(4), 360–380.

Robson, B. J., & Hamilton, D. P. (2004). Three-dimensional modelling of a Microcystis bloom event in the Swan River estuary, Western Australia. *Ecological Modelling*, *174*(1–2), 203–222.

Rogers, C. K., Lawrence, G. A., & Hamblin, P. F. (1995). Observations and numericzal simulation of a shallow, *40*(March 1992), 374–385.

Romero, J. R., & Imberger, J. (2003). Effect of a flood underflow on reservoir water quality: Data and three-dimensional modeling. *Archiv Für Hydrobiologie*, *157*(1), 1–25.

Romero, J. R., Antenucci, J. P., & Imberger, J. (2004). One-and three-dimensional biogeochemical simulations of two differing reservoirs. *Ecological Modelling*, *174*(1–2), 143–160.

Rueda, F. J., & Cowen, E. A. (2005). Exchange between a freshwater embayment and a large lake through a long, shallow channel. *Limnology and Oceanography*, *50*(1), 169–183.

Schlatter, J. W., Wüest, A., & Imboden, D. M. (1997). Hypolimnetic density currents traced by sulphur hexafluoride (SF 6). *Aquatic Sciences*, *59*(3), 225–242.

Semovski, S. V, Mogilev, N. Y., & Sherstyankin, P. P. (2000). Lake Baikal ice: analysis of AVHRR imagery and simulation of under-ice phytoplankton bloom. *Journal of Marine Systems*, *27*(1–3), 117–130.

Serruya, S. (1974). The mixing patterns of the Jordan River in Lake Kinneret 1. *Limnology and Oceanography*, *19*(2), 175–181.

Sharma, S., Blagrave, K., Magnuson, J. J., O'Reilly, C. M., Oliver, S., Batt, R. D., … Winslow, L. (2019). Widespread loss of lake ice around the Northern Hemisphere in a warming world. *Nature Climate Change*, *9*(3), 227.

Smith, V. H., & Schindler, D. W. (2009). Eutrophication science: where do we go from here? *Trends in Ecology & Evolution*, *24*(4), 201–207.

Snortheim, C. A., Hanson, P. C., McMahon, K. D., Read, J. S., Carey, C. C., & Dugan, H. A. (2017). Meteorological drivers of hypolimnetic anoxia in a eutrophic, north temperate lake. *Ecological Modelling*, *343*, 39–53.

Spillman, C. M., Hamilton, D. P., Hipsey, M. R., & Imberger, J. (2008). A spatially resolved model of seasonal variations in phytoplankton and clam (Tapes philippinarum) biomass in Barbamarco Lagoon, Italy. *Estuarine, Coastal and Shelf Science*, *79*(2), 187–203.

Stewart, K. M. (1988). TRACING INFLOWS IN A PHYSICAL MODEL OF LAKE CONSTANCE. *Journal of Great Lakes Research*, *14*(4), 466–478. https://doi.org/10.1016/S0380-1330(88)71579-8.

Straile, D., Kerimoglu, O., & Peeters, F. (2015). Trophic mismatch requires seasonal heterogeneity of warming. *Ecology*, *96*(10), 2794–2805.

Tilzer, M. M., & Goldman, C. R. (1978). Importance of mixing, thermal stratification and light adaptation for phytoplankton productivity in Lake Tahoe (California-Nevada). *Ecology*, *59*(4), 810–821.

Tilzer (1983). The importance of fractional light absorption by photosynthetic pigments for phytoplankton productivity in Lake Constance, *28*, 833–846.

Trolle, D., Skovgaard, H., & Jeppesen, E. (2008). The Water Framework Directive: Setting the phosphorus loading target for a deep lake in Denmark using the 1D lake ecosystem model DYRESM–CAEDYM. *Ecological Modelling*, *219*(1–2), 138–152.

Trolle, D., Hamilton, D. P., Pilditch, C. A., Duggan, I. C., & Jeppesen, E. (2011). Predicting the effects of climate change on trophic status of three morphologically varying lakes: Implications for lake restoration and management. *Environmental Modelling & Software*, *26*(4), 354–370.

Trolle, D., Spigel, B., Hamilton, D. P., Norton, N., Sutherland, D., Plew, D., & Allan, M. G. (2014). Application of a three-dimensional water quality model as a decision support tool for the management of land-use changes in the catchment of an oligotrophic lake. *Environmental Management*, *54*(3), 479–493.

Umlauf, L., & Lemmin, U. (2005). Interbasin exchange and mixing in the hypolimnion of a large lake: The role of long internal waves. *Limnology and Oceanography*, *50*(5), 1601–1611.

Vanderploeg, H. A., Bolsenga, S. J., Fahnenstiel, G. L., Liebig, J. R., & Gardner, W. S. (1992). Plankton ecology in an ice-covered bay of Lake Michigan: Utilization of a winter phytoplankton bloom by reproducing copepods. *Hydrobiologia*, *243*(1), 175–183.

Vilhena, L. C., Hillmer, I., & Imberger, J. rg. (2010). The role of climate change in the occurrence of algal blooms: Lake Burragorang, Australia. *Limnology and Oceanography*, *55*(3), 1188–1200.

Von Westernhagen, N. (2010). *Measurements and modelling of eutrophication processes in Lake Rotoiti, New Zealand*. University of Waikato.

Vonlanthen, P., Bittner, D., Hudson, A. G., Young, K. A., Müller, R., Lundsgaard-Hansen, B., … Seehausen, O. (2012). Eutrophication causes speciation reversal in whitefish adaptive radiations. *Nature*, *482*(7385), 357–362.

Wahl, B., & Peeters, F. (2014). Effect of climatic changes on stratification and deep-water renewal in Lake Constance assessed by sensitivity studies with a 3D hydrodynamic model. *Limnology and Oceanography*, *59*(3), 1035–1052.

Walsby, A. E. (2005). Stratification by cyanobacteria in lakes: a dynamic buoyancy model indicates size limitations met by Planktothrix rubescens filaments. *New Phytologist*, *168*(2), 365–376.

Walsby, A. E., Schanz, F., & Schmid, M. (2006). The Burgundy-blood phenomenon: a model of buoyancy change explains autumnal waterblooms by Planktothrix rubescens in Lake Zürich. *New Phytologist*, *169*(1), 109–122.

Walsh, S. E., Vavrus, S. J., Foley, J. A., Fisher, V. A., Wynne, R. H., & Lenters, J. D. (1998). Global patterns of lake ice phenology and climate: Model simulations and observations. *Journal of Geophysical Research: Atmospheres*, *103*(D22), 28825–28837.

Wang, J., Hu, H., Schwab, D., Leshkevich, G., Beletsky, D., Hawley, N., & Clites, A. (2010). Development of the Great Lakes ice-circulation model (GLIM): application to Lake Erie in 2003–2004. *Journal of Great Lakes Research*, *36*(3), 425–436.

Wang, J., Bai, X., Hu, H., Clites, A., Colton, M., & Lofgren, B. (2012). Temporal and spatial variability of Great Lakes ice cover, 1973–2010. *Journal of Climate*, *25*(4), 1318–1329.

Weiss, R. F., Carmack, E. C. C., & Koropalov, V. M. (1991). Deep-water renewal and biological production in Lake Baikal. *Nature*, *349*(6311), 665–669.

Weyhenmeyer, G. A., Westöö, A.-K., & Willén, E. (2007). Increasingly ice-free winters and their effects on water quality in Sweden's largest lakes. In *European Large Lakes Ecosystem changes and their ecological and socioeconomic impacts*. *Springer*, 111-118.

Wetzel, R. G. (2001). *Limnology: lake and river ecosystems*. gulf professional publishing.

Williamson, C. E., Saros, J. E., Vincent, W. F., & Smol, J. P. (2009). Lakes and reservoirs as sentinels, integrators, and regulators of climate change. *Limnology and Oceanography*, *54*(6part2), 2273–2282.

Wirth, C., Limberger, R., & Weisse, T. (2019). Temperature× light interaction and tolerance of high water temperature in the planktonic freshwater flagellates Cryptomonas (Cryptophyceae) and Dinobryon (Chrysophyceae). *Journal of Phycology*, *55*(2), 404–414.

Woodward, B. L., Marti, C. L., Imberger, J., Hipsey, M. R., & Oldham, C. E. (2017). Wind and buoyancy driven horizontal exchange in shallow embayments of a tropical reservoir: Lake Argyle, Western Australia. *Limnology and Oceanography*, *62*(4), 1636–1657.

Woolway, R. I., & Merchant, C. J. (2019). Worldwide alteration of lake mixing regimes in response to climate change. *Nature Geoscience*, *12*(4), 271–276.

Yao, H., Samal, N. R., Joehnk, K. D., Fang, X., Bruce, L. C., Pierson, D. C., … James, A. (2014). Comparing ice and temperature simulations by four dynamic lake models in Harp Lake: past performance and future predictions. *Hydrological Processes*, *28*(16), 4587–4601.

Zhang, Y., Peng, C., Wang, Z., Zhang, J., Li, L., Huang, S., & Li, D. (2018). The species-specific responses of freshwater diatoms to elevated temperatures are affected by interspecific interactions. *Microorganisms*, *6*(3), 82.

Authors contributions

This paragraph will give an overview of the authors' contributions to each chapter. Details on the data sources can be instead found in the methods and acknowledgment sections of each chapter.

Chapter 2

The research question was jointly developed by me, Hilmar Hofmann and Frank Peeters. I set-up the model, analyzed the output data and drafted the manuscript. Hilmar Hofmann and Frank Peeters helped with the design of the analysis and contributed to the revision of the manuscript. David Hamilton made suggestions for improvement of the manuscript.

Chapter 3

All the three authors participated in the design of the study. I set-up the model, analyzed the output data and drafted the manuscript. Frank Peeters significantly helped with the design of the analysis. Frank Peeters and Hilmar Hofmann contributed to the revision of the manuscript. All authors read and approved the final manuscript.

Chapter 4

The research question was jointly developed by the authors. I designed the study, set-up the model, ran the simulation, undertook the data analysis and prepared the manuscript. Frank Peeters contributed to partial the revision of the manuscript.

Acknowledgments

First of all, I would like to thank my supervisors Prof. Dr. Frank Peeters and Dr. Hilmar Hofmann for their supervision and support during the last years. Their vast store of knowledge, unlimited ideas and love for details greatly improved my way of working and this thesis in particular. I further thank Prof. Dr. David Schleheck for the evaluation of this thesis and for being on my defense committee.

I wish to acknowledge Professor David Hamilton for his guidance with the model AEM3D. Working together at the Griffith University was for me a really stimulant experience. Thanks also to the Mein Program of the University of Konstanz that made this visit possible. For funding and support of this work, I thank the DFG. Large thanks to Tina Romer, fundamental member of the RTG, who always supported and helped me.

I am grateful to have shared this experience with the other PhD students of the RTG and colleagues of the Environmental Physic Group. In particular, thank Manuela Milan for your support and continuous encouragement. I thank Beatrix Rosenberg, Josef Halder and Leon Walther for their help with field work. In particular, a big thank to Bea for the nice time (and chocolate) on the boat. I would also like to acknowledge Stefan Gerlach, who manages the Computer Cluster of the University of Konstanz. Without the cluster I would still been waiting for the results of my first simulations. Thanks also to Andrea Cattani for his guidance with the cluster.

I am really grateful for the encouragement, support and love of my family. Their numerous visits and packages with Italian food made my staying in Konstanz easier. Grazie mamma e nonna! I would also thank all the member of Flamemotions and in particular Michl Blümm. The passion for salsa dancing he has transmitted to me was really helpful to get integrated and to enjoy my staying in Konstanz.

Lastly, I would like to thank Nico for his constant support and patience, who believes in me more than I do. He would deserve half of my doctor title because without him I would have never reached this milestone.

List of publications

Caramatti, I., Peeters, F., Hamilton, D., & Hofmann, H. (2019). **Modelling inter-annual and spatial variability of ice cover in a temperate lake with complex morphology**. *Journal of Hydrological Processes* (2019). https://doi.org/10.1002/hyp.13618

Caramatti, I., Hofmann, H., & Peeters, F. **Effects of climate change on inter-basin exchange in Lower Lake Constance** (in prep)

Caramatti, I., Hofmann, H., & Peeters, F. **Modelling phytoplankton spatiotemporal variability in a morphologically complex lake with winter ice cover** (in prep.)

Conference presentations

ASLO Summer Meeting, Victoria, Canada (June 2018)

Poster presentation: Modelling of inter-annual and spatial variability of ice cover in a subdivided temperate lake

GLEON21 Meeting, Ontario, Canada (November 2019)

Poster presentation: Modelling water exchange between the sub-basins of Lower Lake Constance under climate change scenarios